Magnetic small-angle neutron scattering of bulk ferromagnets

2014 J. Phys.: Condens. Matter 26 383201

(http://iopscience.iop.org/0953-8984/26/38/383201)

OPEN ACCESS
IOP Publishing
Journal of Physics: Condensed Matter
J. Phys.: Condens. Matter **26** (2014) 383201 (41pp)
doi:10.1088/0953-8984/26/38/383201

Topical Review

Magnetic small-angle neutron scattering of bulk ferromagnets

Andreas Michels

Physics and Materials Science Research Unit, University of Luxembourg, 162A Avenue de la Faïencerie, L-1511 Luxembourg, Grand Duchy of Luxembourg

E-mail: andreas.michels@uni.lu

Received 4 May 2014, revised 13 June 2014
Accepted for publication 23 June 2014
Published 2 September 2014

Abstract

We summarize recent theoretical and experimental work in the field of magnetic small-angle neutron scattering (SANS) of bulk ferromagnets. The response of the magnetization to spatially inhomogeneous magnetic anisotropy and magnetostatic stray fields is computed using linearized micromagnetic theory, and the ensuing spin-misalignment SANS is deduced. Analysis of experimental magnetic-field-dependent SANS data of various nanocrystalline ferromagnets corroborates the usefulness of the approach, which provides important quantitative information on the magnetic-interaction parameters such as the exchange-stiffness constant, the mean magnetic anisotropy field, and the mean magnetostatic field due to jumps ΔM of the magnetization at internal interfaces. Besides the value of the applied magnetic field, it turns out to be the ratio of the magnetic anisotropy field H_p to ΔM, which determines the properties of the magnetic SANS cross-section of bulk ferromagnets; specifically, the angular anisotropy on a two-dimensional detector, the asymptotic power-law exponent, and the characteristic decay length of spin-misalignment fluctuations. For the two most often employed scattering geometries where the externally applied magnetic field $\mathbf{H}_0$ is either perpendicular or parallel to the wave vector $\mathbf{k}_0$ of the incoming neutron beam, we provide a compilation of the various unpolarized, half-polarized (SANSPOL), and uniaxial fully-polarized (POLARIS) SANS cross-sections of magnetic materials.

Keywords: micromagnetics, neutron scattering, small-angle scattering

(Some figures may appear in colour only in the online journal)

Contents

1. Introduction

Small-angle neutron scattering (SANS) is one of the most important techniques for microstructure determination, which is utilized in a wide range of scientific disciplines such as materials science, physics, chemistry, and biology. Conventional SANS is able to probe microstructural (density and composition) and magnetic inhomogeneities in the bulk and on a length scale between a few and a few hundred nanometers. As such, SANS ideally complements more direct imaging techniques, e.g. scanning and transmission electron microscopy, Kerr microscopy, atomic force microscopy, or scanning tunnelling microscopy. The research literature on SANS (and on small-angle x-ray scattering (SAXS)) is vast, and any realistic attempt to provide an encyclopaedic listing is beyond the scope of this work. For a selection of reviews on various topics and aspects of small-angle scattering, we refer the reader to [1–31].

From the historical point of view, experimental and theoretical progress in the domain of small-angle scattering is closely connected to the development of laboratory SAXS methods [32]. Only with the advent of nuclear research reactors and the concomitant construction and development of the first SANS instruments at Jülich [1] and Grenoble [33], it became possible to explore magnetism and superconductivity by means of SANS. Perhaps related to this historical perspective is the fact that the theoretical concepts and foundations of *nuclear* SANS and SAXS are relatively well developed and widely acknowledged and applied in experimental studies [32, 34–36].

The SANS technique has also been used to study a wide range of magnetic materials, for instance (in the last 10–15 years) *magnetic* SANS has been employed for investigating the microstructures of amorphous alloys [37–41], hard and soft magnetic nanocomposites [31, 42–57], elemental nanocrystalline $4f$ [58–60] and $3d$ magnets [61–68], the process of dynamic nuclear polarization [69–71], the flux-line lattice of superconductors [72, 73], precipitates in steels [74–77], fractal magnetic domain structures in NdFeB permanent magnets [78], the spin structures of ferrofluids, nanoparticles, and nanowires [79–96], magnetic recording media [97–101], magnetostriction in FeGa alloys [102], electric-field-induced magnetization in multiferroic $HoMnO_3$ [103] and weak antiferromagnetism in $BiFeO_3$ [104], magnetization reversal in exchange-bias materials [105], or chiral and skyrmion-like structures in MnSi single crystals [106, 107].

The prototypical sample in a small-angle scattering experiment consists of a dispersion of homogeneous phase-A nanoparticles in a homogeneous phase-B matrix. For such a two-phase particulate system, the 'standard' expression for the elastic nuclear SANS cross-section $\frac{\mathrm{d}\Sigma_{\mathrm{nuc}}}{\mathrm{d}\Omega}$ is of the form [5]

$$\frac{\mathrm{d}\Sigma_{\mathrm{nuc}}}{\mathrm{d}\Omega}(\mathbf{q}) = \frac{(\Delta\rho)^2_{\mathrm{nuc}}}{V}\left|\sum_{j=1}^{N} V_{p,j}\, F_j(\mathbf{q})\, \exp(-\mathrm{i}\mathbf{q}\,\mathbf{r}_j)\right|^2, \quad (1)$$

where $\mathbf{q}$ is the momentum-transfer vector, N is the number of particles in the scattering volume V, $(\Delta\rho)^2_{\mathrm{nuc}}$ denotes the nuclear scattering-length density contrast between the particles and the matrix (assumed to be a constant here for simplicity), and $V_{p,j}$, F_j, and $\mathbf{r}_j$ represent, respectively, the volume, form factor, and position vector of particle 'j'.

Besides analyzing nuclear SANS data, equation (1) is also often used to analyze *magnetic* SANS data, and in most cases the expressions for the magnetic SANS cross-section are adapted on an almost one-to-one correspondence basis from nuclear SANS theory. Specifically, $(\Delta\rho)^2_{\mathrm{nuc}}$ in equation (1) is then replaced by its magnetic counterpart $(\Delta\rho)^2_{\mathrm{mag}}$, and an additional factor $\sin^2\alpha$ is introduced (see discussion below), which takes account of the dipolar nature of the neutron-magnetic interaction [108]. We note that different definitions regarding the angle α can be found in the literature (see, e.g. [21, 94, 109]). For a dilute system of monodisperse magnetic nanoparticles, the magnetic part of the total unpolarized SANS cross-section is commonly expressed as [21, 94, 110]

$$\frac{\mathrm{d}\Sigma_{\mathrm{mag}}}{\mathrm{d}\Omega}(\mathbf{q}) = \frac{N}{V}(\Delta\rho)^2_{\mathrm{mag}}\, V_p^2\, |F(\mathbf{q})|^2\, \sin^2\alpha. \quad (2)$$

One may also include a structure factor in equation (2), but (for rigid nanoparticles in a rigid matrix) this would only affect the q-dependence of the scattering (similar to a particle-size distribution), not its field dependence.

While equation (2) can certainly be employed for analyzing magnetic SANS data on a wide range of materials (e.g. ferrofluids, saturated or uniformly magnetized magnetic nanoparticles in a saturated or nonmagnetic matrix, or pores in a saturated ferromagnetic matrix) [94, 111, 112], there exists an important class of magnets-bulk ferromagnets-where the mere decomposition of the magnetic SANS cross-section in terms of form and structure factors fails to describe experimental

magnetic-field-dependent data; only at complete magnetic saturation may the magnetic SANS of bulk ferromagnets be described in terms of equation (2) (e.g. for a nanocomposite).

A detailed discussion on why equation (2) is inadequate to describe the magnetic SANS of *bulk ferromagnets* can be found in [26]. Here, we briefly recall these (interrelated) facts in order to achieve a self-contained introductory discussion.

(a) It is rather obvious that equation (2) is not adapted to the magnetic microstructure of a bulk ferromagnet, simply because there is no direct relation to the characteristic parameters of a ferromagnet such as the exchange constant, magnetic anisotropy, or magnetostatic field. The only information regarding magnetism which is contained in equation (2) refers to variations in the *magnitude* of the magnetization (via $(\Delta\rho)^2_{\rm mag}$) and in the *orientation* of the magnetization (via $\sin^2\alpha$) of *homogeneously* magnetized domains (particles).

(b) The applied-field dependence of the azimuthally-averaged $\frac{{\rm d}\Sigma_{\rm mag}}{{\rm d}\Omega}$, equation (2), is exclusively embodied in the factor $\sin^2\alpha$. If α is taken to be the angle between $\mathbf{q}$ and the local direction of the magnetization $\mathbf{M}$ of a uniformly magnetized nanoparticle, then, for the scattering geometry where the applied magnetic field $\mathbf{H}_0$ is perpendicular to the wave vector $\mathbf{k}_0$ of the incoming neutron beam ($\mathbf{k}_0 \perp \mathbf{H}_0$), the expectation value of the function $\sin^2\alpha$ varies between a value of $1/2$ at saturation and a value of $2/3$ in the demagnetized state (random domain orientation); note that while the azimuthal anisotropy on a two-dimensional detector changes considerably (between these two cases), the azimuthal average of the $\sin^2\alpha$ term changes only relatively weakly. For $\mathbf{k}_0 \parallel \mathbf{H}_0$, the expectation value of $\sin^2\alpha$ varies between a value of 1 at saturation and a value of $2/3$ in the demagnetized state [108, 113]. In other words, for $\mathbf{k}_0 \perp \mathbf{H}_0$ an intensity *increase* (of azimuthally-averaged data) by a factor of $4/3$ is predicted between saturation and the demagnetized state, whereas for $\mathbf{k}_0 \parallel \mathbf{H}_0$, a corresponding intensity *decrease* by a factor of $2/3$ is expected. These predictions are, however, in striking contrast to experimental observations (see, e.g. figure 3(*a*) below).

(c) Magnetic SANS cross-sections based on equation (2) predict q-scaling, i.e. the $\frac{{\rm d}\Sigma_{\rm mag}}{{\rm d}\Omega}$ that are measured at different fields are expected to be parallel to each other (i.e. shifted along the $\frac{{\rm d}\Sigma_{\rm mag}}{{\rm d}\Omega}$ axis), which is also in contrast to experiment. In other words, there are no characteristic magnetic length scales contained in equation (2), which may vary as a function of the applied field.

The decisive point to realize is that magnetic SANS cross-sections based on equation (2) entirely ignore the *continuous* spatial variations of the local orientation of the magnetization vector $\mathbf{M}(\mathbf{r})$ both within and between the domains. It is the purpose of this article to contribute to resolving these issues by introducing a theory of magnetic SANS of bulk ferromagnets in terms of the continuum theory of micromagnetics.

Micromagnetics is a phenomenological continuum theory which has been developed in order to compute the magnetization vector field $\mathbf{M}(\mathbf{r})$ of an arbitrarily-shaped ferromagnetic body, when the applied magnetic field, the geometry of the ferromagnet, and the magnetic materials parameters are known [114–117]. The characteristic length scale to which micromagnetic calculations apply ranges between a few nanometers and a few hundred nanometers ($\sim$ resolution range of the SANS technique). Therefore, the combination of micromagnetic computations with SANS is straightforward and adapted to the problem. Pioneering work in this direction was performed by Kronmüller *et al* [118] who calculated the magnetic SANS due to spin disorder related to the strain fields of dislocations. For more information about dislocation studies using small-angle scattering, we refer the reader to [1, 4, 118–130].

We are interested in the elastic *spin-misalignment scattering*, which results from the static magnetic microstructure of a *bulk ferromagnet*. Spin-misalignment scattering is of relevance whenever the magnitude of the externally applied magnetic field is insufficient to completely saturate the sample. The magnetic materials that we have in mind are characterized by a large number of microstructural defects (e.g. pores, grain or phase boundaries, dislocations, point defects). Examples for such materials are polycrystalline elemental magnets with a nanometer crystallite size, heavily deformed (cold worked) metals, nanoporous ferromagnets, or multiphase magnetic nanocomposites, including magnetic steels. As one of its central themes, the present work points out that spin-misalignment scattering will typically dominate the magnetic SANS signal from bulk ferromagnets (compare e.g. figure 3(*a*) below).

The mechanisms by which spin disorder is generated are essentially related to (a) magnetoelastic and magnetocrystalline anisotropy and (b) internal magnetostatic stray fields, for instance due to spatially fluctuating materials' parameters. To be more specific, forces due to the distortion of the lattice (in the vicinity of a defect) tend to rotate the local magnetization vector field $\mathbf{M}(\mathbf{r})$ along the main axes of the system of internal stresses (magnetoelastic coupling), while magnetocrystalline anisotropy tries to pull the magnetic moments along the principal axes of the crystal; figure 1 illustrates the magnetization distribution in the vicinity of point and line defects. Likewise, jumps in the values of magnetization, exchange, or anisotropy constants at internal interfaces (e.g. in a magnetic nanocomposite or nanoporous ferromagnet) give rise to inhomogenous magnetization states, which contribute significantly to the magnetic SANS signal; figure 2 depicts $\mathbf{M}(\mathbf{r})$ around a pore in a ferromagnetic matrix.

For the discussion of magnetic SANS, it is important to emphasize that the adjustment of the magnetization along the respective local 'easy' axes does not occur abruptly, i.e. on a scale of the interatomic spacing, but requires a more extended range. This is a consequence of the quantum-mechanical exchange interaction, which spreads out local perturbations in $\mathbf{M}(\mathbf{r})$ over larger distances [131][1]. The sizes of such spin inhomogeneities (i.e. gradients in $\mathbf{M}$) are characterized by the field-dependent exchange length l_H of the field (see figure 1), which takes on values ($\sim$1–100 nm) that are routinely accessible by the SANS technique.

[1] This statement should not imply that the exchange interaction is the only important interaction for the discussion of magnetic SANS of bulk ferromagnets.

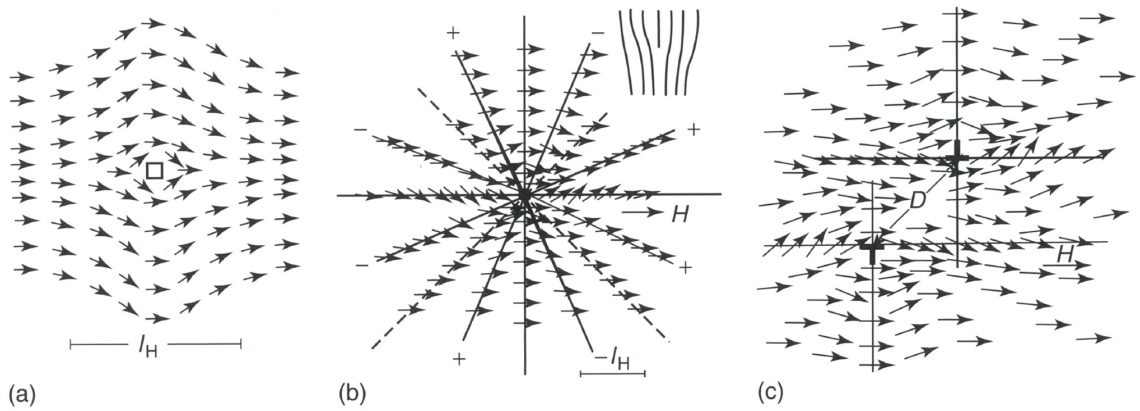

Figure 1. Qualitative magnetization distribution around (*a*) a vacancy-type defect, (*b*) an isolated quasidislocation, and (*c*) a quasidislocation dipole. Reprinted with permission from [117] (courtesy of Dagmar Goll, Aalen University, Aalen, Germany). Copyright 2007 by Wiley.

It is of crucial importance to realize that-even in the approach-to-saturation regime-spin-misalignment SANS is strongly dependent on the applied magnetic field and that it usually dominates the $d\Sigma/d\Omega$ of a bulk ferromagnet. As an example, figure 3(*a*) shows the unpolarized (nuclear and magnetic) $d\Sigma/d\Omega$ of nanocrystalline Co with an average crystallite size of 9.5 ± 3.0 nm [62, 63]; we note that the sample under study is a fully dense polycrystalline bulk metal with a nanometer grain size, not nanoparticles in a matrix. The cross-section at the smallest momentum transfers varies by more than three orders of magnitude between 5 mT and 1800 mT. Even in the saturation regime (compare hysteresis loop in figure 3(*b*)), $d\Sigma/d\Omega$ exhibits an extraordinarily large field variation, which cannot be reproduced by means of equation (2) (see above). The origin of the large field dependence of $d\Sigma/d\Omega$ near saturation is not related to a macroscopic magnetic domain structure, but to the failure of the spins to completely align along the external field, in other words, it is due to spin-misalignment.

Furthermore, closer inspection of the $d\Sigma/d\Omega$ data in figure 3(*a*) reveals that, with an increasing field, a characteristic length scale is evolving towards larger q values (i.e. q-scaling is lost). This observation provides evidence for the existence of characteristic magnetic-field-dependent length scales in the system. In fact, micromagnetic theory predicts that long-wavelength magnetization fluctuations (characterized by l_H) are selectively suppressed by an increasing applied field.

The remarkably strong field dependence of magnetic SANS near saturation may have important consequences for the analysis of SANS data. In unpolarized SANS experiments on apparently saturated samples, the scattering along the field direction $\mathbf{H}_0$ is often taken as the nuclear SANS contribution. This is common practice, for instance in SANS studies on steels, where applied fields of the order of 1 T are usually employed for carrying out the separation of nuclear and magnetic SANS (e.g. [74]). As we will see later on, a large part of the spin-misalignment SANS scatters along $\mathbf{H}_0$. Therefore, when H_0 is not large enough to sufficiently suppress the spin-misaligned SANS, the determined nuclear SANS may contain a significant (and in view of the results shown in figure 3 an even dominating) 'contamination' due to magnetic scattering [76].

Once spin-misalignment SANS is suppressed by a large applied magnetic field, the remaining nuclear and magnetic SANS (at $H_0 \rightarrow \infty$)-the so-called residual SANS cross-section-may be analyzed in terms of the classical particle-matrix concept, equations (1) and (2).

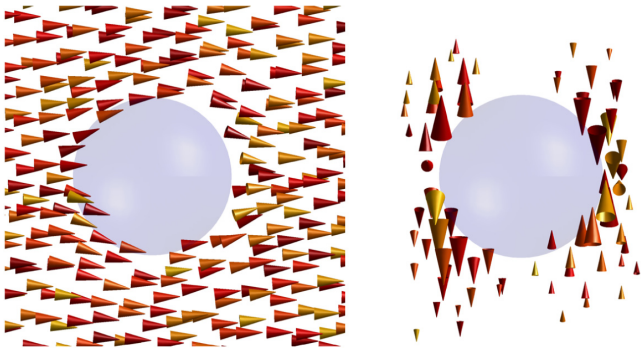

Figure 2. Result of a micromagnetic simulation for the magnetization distribution around a spherical pore (diameter: 10 nm) in a ferromagnetic iron matrix (two-dimensional cut out of a three-dimensional simulation). The external magnetic field $\mathbf{H}_0$ is applied horizontally in the plane ($\mu_0 H_0 = 0.6$ T). Note that the jump of the magnetization magnitude at the pore-matrix interface is $\mu_0 \Delta M = 2.2$ T. The left image shows the magnetization distribution (arrows) in the iron matrix. In order to highlight the spin-misalignment in the iron phase, the right image displays the magnetization component $\mathbf{M}_\perp$ perpendicular to $\mathbf{H}_0$; thickness of arrows is proportional to the magnitude of $\mathbf{M}_\perp$. Data courtesy of Sergey Erokhin, General Numerics Research Lab, Jena, Germany (www.general-numerics-rl.de/).

The present review article is largely based on previous experimental and theoretical SANS work [48, 51, 53–56, 66–68]. In particular, we have developed a theory for the magnetic SANS of weakly *inhomogeneous* ferromagnets such as nanocomposites or steels [53], which, besides spatially inhomogeneous magnetic anisotropy fields, takes into account small variations of the magnitude of the magnetization. This represents an important extension of earlier work, summarized in [26], which has considered magnetic SANS due to anisotropy fields in *homogeneous* magnets with uniform saturation magnetization.

The paper is organized as follows: section 2 introduces the micromagnetic model based on which magnetic SANS is described. In particular, we briefly discuss the main magnetic energy contributions (section 2.1), and we solve

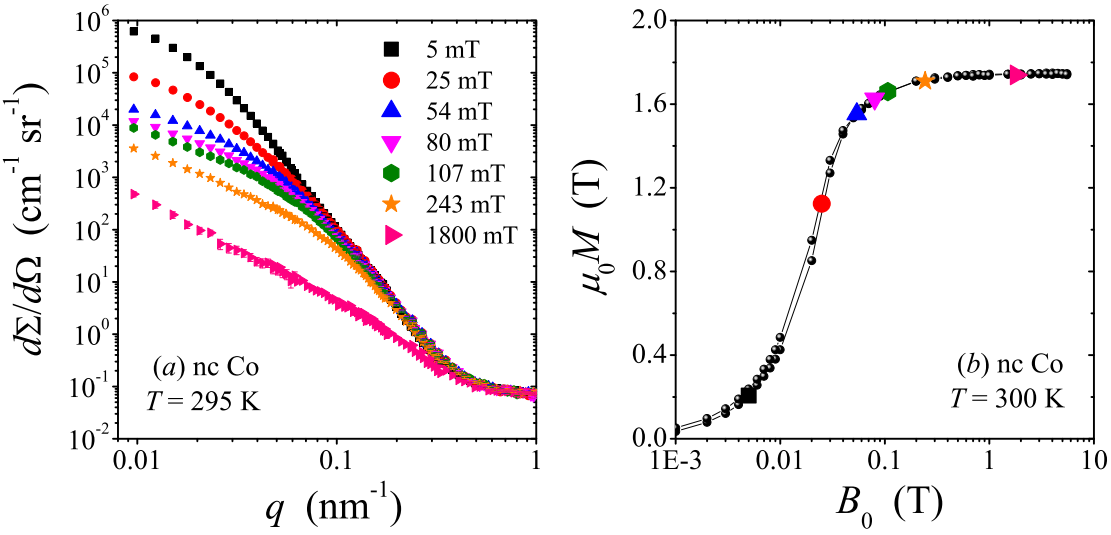

Figure 3. (*a*) Azimuthally-averaged unpolarized SANS cross-section $\mathrm{d}\Sigma/\mathrm{d}\Omega$ of nanocrystalline Co metal (average grain size: 9.5 ± 3.0 nm) as a function of momentum transfer q ($\mathbf{k}_0 \perp \mathbf{H}_0$) at selected applied magnetic fields (see inset) (log–log scale). (*b*) (•) Room-temperature magnetization curve of nanocrystalline Co (log-linear scale) [62]. The $M(B_0)$ values where the SANS measurements shown in (*a*) have been carried out are indicated by the large data points. Reprinted with permission from [63]. Copyright 2003 by the American Physical Society.

the linearized micromagnetic equations to obtain closed-form expressions for the magnetization Fourier coefficients (section 2.2), which are used in order to compute the magnetic SANS cross-section (section 2.3). In section 3, we briefly introduce the typical SANS setup (section 3.1) and the nomenclature and approximations used (section 3.2), we explicitly display the spin-resolved (POLARIS, section 3.3), half-polarized (SANSPOL, section 3.4), and unpolarized (section 3.5) SANS cross-sections, and we discuss and graphically display SANS at magnetic saturation (section 3.6). In section 4, spin-misalignment scattering is discussed. We comment on the usefulness of half-polarized experiments for the analysis of spin-misalignment SANS (section 4.1), and we demonstrate how experimental unpolarized (section 4.2) and spin-resolved (section 4.3) SANS data on nanocrystalline bulk ferromagnets can be analyzed in order to decipher the magnetic interactions. Section 5 provides an account of the real-space analysis of magnetic SANS data in terms of the autocorrelation function of the spin-misalignment, which is defined in section 5.1. Magnetization profiles, theoretical and experimental correlation functions (section 5.2) and the field dependence of the spin-misalignment length (section 5.3) are discussed. Finally, section 6 summarizes the main results of this work and provides an outlook on future challenges in the field. In the appendix, we list the most important parameters, quantities, and relations.

2. Micromagnetic model of bulk ferromagnets near saturation

In section 2.1, we discuss briefly the main micromagnetic energy contributions, section 2.2 provides the solution of Brown's balance-of-torques equation for the Fourier coefficients of the magnetization, whereas section 2.3 establishes the relation between micromagnetics and SANS.

2.1. Magnetic energy contributions

The magnetic energy contributions that are taken into account in standard micromagnetic computations are due to the exchange interaction, the magnetic anisotropy, and the external and magnetodipolar field.

2.1.1. Exchange energy. In the limit of a continuous ferromagnetic material, the exchange energy E_{exch} (for cubic crystal structures) can be approximated by [132, 133]

$$E_{\mathrm{exch}} = \int_V A\left[(\nabla m_x)^2 + (\nabla m_y)^2 + (\nabla m_z)^2\right] \mathrm{d}V, \qquad (3)$$

where $A > 0$ denotes the exchange-stiffness constant, $m_{x,y,z}$ are the Cartesian components of a unit vector $\mathbf{m} = \mathbf{M}/M_s$ in the direction of the magnetization, and the integral extends over the sample volume V. The exchange energy is a positive definite quantity, which favours the parallel alignment of neighbouring atomic magnetic moments in the crystal lattice. Any nonuniformity in $\mathbf{M}$ has an energy cost. Typical values for A are in the $10\,\mathrm{pJ\,m^{-1}}$ range [116, 134]. Note that in multiphase magnets, the exchange constant is a function of the position inside the material, i.e. $A = A(\mathbf{r})$ [135–137].

Equation (3) represents a continuum expansion based on the discrete Heisenberg Hamiltonian

$$H_{\mathrm{exch}} = -\sum_{i,j} J_{ij}(\mathbf{r}_{ij})\,\mathbf{S}_i(\mathbf{r}_i)\,\mathbf{S}_j(\mathbf{r}_j), \qquad (4)$$

where J_{ij} denotes the quantum mechanical exchange integral between localized magnetic moments with spins $\mathbf{S}_i$ and $\mathbf{S}_j$ separated by a distance $\mathbf{r}_{ij} = \mathbf{r}_j - \mathbf{r}_i$. Equation (3) follows from equation (4) by treating the $\mathbf{S}_i$ as (quasi)classical continuous vectors, taking into account only nearest neighbour exchange interactions (of equal strength J), and by assuming small angles between neighbouring spins (see e.g. [138] for a derivation

of equation (3)). Therefore, the applicability of the above continuum expression for the exchange energy is restricted to situations where the magnetization changes smoothly. Strongly inhomogeneous magnetization configurations are expected, e.g. at/across internal interfaces such as grain boundaries, where the materials parameters may take on different values as compared to the bulk [139].

Furthermore, for crystal lattices of low symmetry, the exchange interaction is anisotropic and the tensor character of A should be taken into account [132, 133]. For example, hexagonal or tetragonal crystal structures would require two exchange constants. In fact, equation (3) has been derived for cubic crystals; here, $A = JS^2c/a$, where S is the spin quantum number (measured in units of $\hbar$), a is the lattice constant, and $c = 1, 2, 4$ for simple cubic, body-centred cubic, and face-centred cubic lattices, respectively. However, we would like to note that the vast majority of micromagnetic computations that are reported in the literature *model* nonuniform spin states by a single stiffness parameter. Likewise, one may also question the usefulness of the (short-range) expression, equation (3), for describing long-range *indirect* exchange interactions in ferromagnets such as in the 4f metals. Again, we emphasize that the purpose of equation (3) is to model to a first-order approximation the effect of magnetization inhomogeneities. See the book by Kronmüller and Fähnle [116] for a micromagnetic treatment of itinerant exchange.

2.1.2. Magnetic anisotropy.

Magnetocrystalline anisotropy. The magnetocrystalline anisotropy energy $E_{\rm mc}$ expresses the dependence of the magnetic energy of a ferromagnet on the orientation of the magnetization $\mathbf{M}$ relative to the crystal axes. The origin of magnetocrystalline anisotropy is related to the combined action of the spin–orbit (L-S) coupling and the crystal-field interaction. The magnetodipolar interaction may also contribute to $E_{\rm mc}$ [140, 141]; however, dipolar anisotropy is generally small and vanishes for ideal cubic and hexagonal lattices [138]. On a phenomenological level, $E_{\rm mc}$ is determined by an expression for the anisotropy energy density $\omega_{\rm mc}$, which is a function of the position $\mathbf{r}$ and of $\mathbf{M}$ [114],

$$E_{\rm mc} = \int_V \omega_{\rm mc}\left[\mathbf{r}, \mathbf{M}(\mathbf{r})\right] \mathrm{d}V. \tag{5}$$

Note that due to the micromagnetic constraint

$$|\mathbf{M}| = \left(M_x^2 + M_y^2 + M_z^2\right)^{1/2} = M_s, \tag{6}$$

where M_s denotes the saturation magnetization, $\omega_{\rm mc}$ depends only on two independent components of $\mathbf{M}$. The magnetocrystalline anisotropy energy favours the orientation of $\mathbf{M}$ along certain crystallographic directions, the so-called easy axes. Expressions for $E_{\rm mc}$ reflect therefore the symmetry of the underlying crystal lattice. In particular, $E_{\rm mc}$ must be an even function of $\mathbf{M}$.

In [116], various anisotropy expressions for cubic, hexagonal, tetragonal, and orthorombic crystal structures can be found. For the case of cubic ('c') and uniaxial ('u') anisotropy, $\omega_{\rm mc}$ can be expanded in powers of the reduced magnetization components $\mathbf{m} = \mathbf{M}/M_s = (m_x, m_y, m_z)$ as [115]

$$\begin{aligned}\omega_{\rm mc}^c = {} & K_1\left(m_x^2 m_y^2 + m_x^2 m_z^2 + m_y^2 m_z^2\right) \\ & + K_2 m_x^2 m_y^2 m_z^2 + \ldots,\end{aligned} \tag{7}$$

and

$$\begin{aligned}\omega_{\rm mc}^u &= K_{u1}(1 - m_z^2) + K_{u2}(1 - m_z^2)^2 + \ldots \\ &= K_{u1}\sin^2\gamma + K_{u2}\sin^4\gamma + \ldots,\end{aligned} \tag{8}$$

where the respective K represent the temperature-dependent anisotropy constants, and γ denotes the angle between $\mathbf{m}$ and the direction of the uniaxial anisotropy axis. The easy directions for the magnetization are found by solving the extreme conditions $\partial\omega_{\rm mc}/\partial m_j = 0$ and $\partial^2\omega_{\rm mc}/\partial m_j^2 > 0$, where $j = x, y, z$; see [116] for the phase diagrams of cubic and hexagonal crystals. For the examples of α-Fe (bcc) and Ni (fcc), the respective easy directions at room temperature are the cube axes $\langle 100\rangle$ and the body diagonals $\langle 111\rangle$, whereas in hcp Co single crystals, the magnetic moments at room temperature are aligned along the c-axis and the basal plane is a so-called hard plane for the magnetization. Experimental values for the anisotropy constants range between about $10^2\,\mathrm{J\,m^{-3}}$ (for soft magnetic materials) and $10^7\,\mathrm{J\,m^{-3}}$ (for hard magnets) [116, 134, 142]. Note also that, as with the exchange constant, the K's may depend on the position, i.e. $K = K(\mathbf{r})$ (e.g. [143, 144]).

Magnetoelastic anisotropy. When an unstressed ferromagnetic specimen is magnetized by an increasing applied magnetic field, the dimensions of the body change. The process continues until elastic counterforces provide for a state of stable equilibrium. This phenomenon is called magnetostriction, and it demonstrates that there is a connection between the elastic and magnetic properties of magnetic materials. Magnetostriction occurs because the magnetic energy of a ferromagnetic crystal depends on the components of the strain tensor, and it may be energetically favourable for an unstrained lattice to spontaneously deform and lower its energy. The associated interaction energy is called the magnetoelastic energy $E_{\rm me}$, which can also be defined via a volume integral over some energy density $\omega_{\rm me}$ (compare equation (5)),

$$E_{\rm me} = \int_V \omega_{\rm me}\,\mathrm{d}V. \tag{9}$$

The general treatment of magnetostrictive effects in deformable magnets is a highly complicated task [116], and we refer the reader to chapter 8 in Brown's book [114] for a critical discussion of the underlying assumptions of the Voigt approximation.

For polycrystalline magnetic materials, it is well known that the mechanical lattice strain, which is related to microstructural imperfections, couples to the spin distribution and may give rise to nonuniform magnetization patterns [145, 146]. For instance, the long-range stress field of a straight dislocation line ($\sigma \propto 1/r$) produces a characteristic magnetic structure

(see figure 1), which can be resolved via the SANS technique [126]. We will close this subsection by stating the relevant expressions for the magnetoelastic coupling energy of cubic and hexagonal crystal structures, which form the basis for determining the spin distribution in the vicinity of stress-active defects. For cubic crystals, the magnetoelastic coupling energy-density (in cubic crystal coordinates) can be expressed as [116]

$$\omega_{\rm me}^{c} = -\frac{3}{2}\,\lambda_{100}\sum_{i=1}^{3}\sigma_{ii}\,m_i^2 - \frac{3}{2}\,\lambda_{111}\sum_{i\neq j}\sigma_{ij}\,m_i\,m_j, \quad (10)$$

where λ_{100} and λ_{111} denote the saturation magnetostriction constants along the indicated crystallographic directions, the m_i $(i = x, y, z)$ are the Cartesian components of the unit vector in the direction of the magnetization, and the components of the stress tensor $\boldsymbol{\sigma}$ are due to internal stresses related to microstructural defects (or to externally applied stresses). Values for the λ's range between about 10^{-3} and 10^{-6}. For hexagonal materials, one finds [147]

$$\begin{aligned}\omega_{\rm me}^{u} = & -\sum_{i,j\neq 3}\sigma_{ii}\left(\lambda_{ii}\,m_i^2 + \frac{1}{2}\lambda_{ij}\,m_j^2\right) - \sigma_{33}\,\lambda_{33}\,m_3^2 \\ & - 2\,(\lambda_{11}-\lambda_{12})\,\sigma_{12}\,m_1\,m_2 - \lambda_{44}\sum_{i\neq 3}\sigma_{i3}\,m_3\,m_i, \quad (11)\end{aligned}$$

With respect to the micromagnetic SANS theory (see sections 2.2 and 2.3 below), we note that we do not employ any of the equations (7)–(11) for the magnetocrystalline and/or magnetoelastic energy density. Rather, the linearized micromagnetic equations are solved by using an approximate formal expression for ω, which includes both magnetocrystalline and magnetoelastic anisotropy. As discussed in section 4.2, the analysis of experimental magnetic-field-dependent SANS data allows one to determine the Fourier coefficients of the magnetic anisotropy field which are related to that particular ω.

2.1.3. Magnetostatic energy.

External magnetic field. An externally applied magnetic field $\mathbf{H}_0$ (assumed to be homogeneous throughout this paper) imposes a torque on the magnetization and tries to rotate the magnetic moments along its direction. The corresponding interacting energy is called the Zeeman energy $E_{\rm z}$ and is given by

$$E_{\rm z} = -\mu_0\int_V \mathbf{M}\,\mathbf{H}_0\,{\rm d}V, \quad (12)$$

where $\mu_0 = 4\pi\,10^{-7}\,{\rm T\,m\,A^{-1}}$ is the permeability of free space.

Magnetodipolar interaction. Within the Lorentz continuum approximation, the magnetostatic field $\mathbf{H}_d(\mathbf{r})$ that is created by the magnetization $\mathbf{M}$ is related to a magnetostatic self-energy [115]

$$\begin{aligned}E_{\rm m} = & -\frac{1}{2}\mu_0\int_V \mathbf{M}\,\mathbf{H}_d\,{\rm d}V \quad (13)\\ = & +\frac{1}{2}\mu_0\int_{\rm all\ space}|\mathbf{H}_d|^2\,{\rm d}V.\end{aligned}$$

Note that the second integral in equation (13) extends over all space; the factor $1/2$ comes from the fact that the magnetostatic energy is a self-energy and, without it, the interaction of each pair of magnetic moments is counted twice. Basic magnetostatics (i.e. the solution of the Poisson equation), allows one to compute $\mathbf{H}_d$ from the scalar potential function

$$U(\mathbf{r}) = \frac{1}{4\pi}\left(-\int_V\frac{\nabla_{\mathbf{r}'}\cdot\mathbf{M}(\mathbf{r}')}{|\mathbf{r}-\mathbf{r}'|}\,{\rm d}V' + \int_S\frac{\mathbf{n}\cdot\mathbf{M}(\mathbf{r}')}{|\mathbf{r}-\mathbf{r}'|}\,{\rm d}S'\right), \quad (14)$$

according to

$$\begin{aligned}\mathbf{H}_d(\mathbf{r}) = & -\nabla U(\mathbf{r})\\ = & \frac{1}{4\pi}\left(-\int_V\frac{(\mathbf{r}-\mathbf{r}')\ \nabla_{\mathbf{r}'}\cdot\mathbf{M}(\mathbf{r}')}{|\mathbf{r}-\mathbf{r}'|^3}\,{\rm d}V'\right.\\ & \left.+\int_S\frac{(\mathbf{r}-\mathbf{r}')\ \mathbf{n}\cdot\mathbf{M}(\mathbf{r}')}{|\mathbf{r}-\mathbf{r}'|^3}\,{\rm d}S'\right). \quad (15)\end{aligned}$$

The first integral in equation (14) is over the volume and the second integral over the surface of the ferromagnetic body. The last expression on the right hand side of equation (13) embodies the pole-avoidance principle: the magnetostatic self-energy $E_{\rm m} \geqslant 0$ tries to avoid any sort of fictitious magnetic volume $(-\nabla\cdot\mathbf{M})$ or surface $(\mathbf{n}\cdot\mathbf{M})$ charges. The sources of $\mathbf{H}_d$ are due to inhomogeneities in $\mathbf{M}$, either in orientation or in magnitude. In contrast to the previously discussed energy terms (equations (3), (5), (9), and (12)), which involve only a single integration over the sample volume, equation (13) requires integrating twice over the same volume.

2.2. Balance of torques

In order to find the equilibrium magnetization distribution, the total magnetic energy

$$E_{\rm tot} = E_{\rm exch} + E_{\rm mc} + E_{\rm me} + E_{\rm z} + E_{\rm m} \quad (16)$$

of a ferromagnet should be considered as a functional of its magnetization state,

$$E_{\rm tot} = E_{\rm tot}\,[\mathbf{M}(\mathbf{r})]\,. \quad (17)$$

The state which delivers a (local) minimum to this functional corresponds to an equilibrium magnetization configuration. Therefore, at static equilibrium, the variation of $E_{\rm tot}$ must vanish,

$$\delta E_{\rm tot} = \delta(E_{\rm exch} + E_{\rm mc} + E_{\rm me} + E_{\rm z} + E_{\rm m}) = 0. \quad (18)$$

As detailed in [114–117], variational calculus leads to a set of nonlinear partial integro-differential equations for the bulk, along with quite complex boundary conditions for the magnetization at the surface. In keeping with our interest in the magnetic microstructure within the bulk of macroscopic magnetic bodies, we restrict our attention here to the bulk equilibrium conditions. The static equations of micromagnetics (so-called Brown's equations) can be conveniently expressed as a balance-of-torques equation [114–117],

$$\mathbf{M}(\mathbf{r})\times\mathbf{H}_{\rm eff}(\mathbf{r}) = 0. \quad (19)$$

Equation (19) expresses the fact that at static equilibrium the torque on the magnetization vector field $\mathbf{M}(\mathbf{r})$ due to an effective magnetic field $\mathbf{H}_{\text{eff}}(\mathbf{r})$ vanishes everywhere inside the material. The effective field

$$\mathbf{H}_{\text{eff}}(\mathbf{r}) = \mathbf{H}_0 + \mathbf{H}_d(\mathbf{r}) + \mathbf{H}_p(\mathbf{r}) + \frac{2A}{\mu_0 M_s^2}\nabla^2\mathbf{M}(\mathbf{r}) \tag{20}$$

is composed of a uniform applied magnetic field $\mathbf{H}_0$, of the magnetostatic field $\mathbf{H}_d(\mathbf{r})$, of the magnetic anisotropy field $\mathbf{H}_p(\mathbf{r})$, and of the exchange field (last term on the right hand side of equation (20)); $\nabla = \mathbf{e}_x\partial/\partial x + \mathbf{e}_y\partial/\partial y + \mathbf{e}_z\partial/\partial z$, where $\mathbf{e}_x$, $\mathbf{e}_y$, and $\mathbf{e}_z$ represent the unit vectors along the Cartesian laboratory axes.

In the following, we assume the material to be nearly saturated along $\mathbf{H}_0 \parallel \mathbf{e}_z$, i.e. we write

$$\mathbf{M}(\mathbf{r}) = M_x(\mathbf{r})\,\mathbf{e}_x + M_y(\mathbf{r})\,\mathbf{e}_y + M_z(\mathbf{r})\,\mathbf{e}_z \tag{21}$$

with $M_x \ll M_z$ and $M_y \ll M_z$ (small-misalignment approximation). The local saturation magnetization is assumed to differ only slightly from its spatial average, i.e. $M_z(\mathbf{r}) \cong M_s$.

Furthermore, we assume that the anisotropy-energy density $\omega = \omega(\mathbf{r}, \mathbf{M})$ depends only linearly on the components of the magnetization, i.e. $\omega \cong g_0 + g_1(\mathbf{r})M_x + g_2(\mathbf{r})M_y$, where the g_i are functions of position [114]. As a consequence, the resulting anisotropy field

$$\mathbf{H}_p = -\mu_0^{-1}\left(\partial\omega/\partial M_x, \partial\omega/\partial M_y, \partial\omega/\partial M_z\right) \tag{22}$$

is independent of $\mathbf{M}$ and, therefore, also independent of the applied magnetic field, implying that near saturation $\mathbf{H}_p = \mathbf{H}_p(\mathbf{r})$. As mentioned in section 2.1.2, due to the micromagnetic constraint $|\mathbf{M}| = M_s$, an anisotropy-energy density of the form $\omega = \omega(\mathbf{r}, M_x, M_y, M_z)$ may be re-expressed as $\omega = \omega(\mathbf{r}, M_x, M_y)$ with the consequence that only two independent components of $\mathbf{H}_p$ exist [145]. In the approach-to-saturation regime, when $\mathbf{M}$ is nearly aligned parallel to the external magnetic field $\mathbf{H}_0$, only those components of $\mathbf{H}_p$ which are normal to $\mathbf{H}_0$ are physically effective in producing a torque on the magnetization. For the solution of the balance-of-torques equation, it proves to be convenient to introduce the Fourier transform

$$\mathbf{h}(\mathbf{q}) = \left(h_x(\mathbf{q}), h_y(\mathbf{q}), 0\right) \tag{23}$$

of the magnetic anisotropy field $\mathbf{H}_p(\mathbf{r})$ as

$$\mathbf{H}_p(\mathbf{r}) = \frac{1}{(2\pi)^{3/2}}\int \mathbf{h}(\mathbf{q})\,\exp(\mathrm{i}\mathbf{q}\mathbf{r})\,\mathrm{d}^3q. \tag{24}$$

The details of the sample's microstructure (e.g. grain size, lattice strain, crystallographic texture) are included in $\mathbf{H}_p(\mathbf{r})$ [62].

The micromagnetic treatment of the magnetostatic self-interaction starts with Maxwell's equations. One of them states that the magnetic flux density $\mathbf{B}$ is divergence-free, i.e.

$$\nabla\cdot\mathbf{B} = 0, \tag{25}$$

where

$$\mathbf{B} = \mu_0\left(\mathbf{H}_0 + \mathbf{H}_d + \mathbf{M}\right). \tag{26}$$

From equations (25) and (26), it follows that

$$\nabla\cdot(\mathbf{H}_0 + \mathbf{H}_d) = -\nabla\cdot\mathbf{M}, \tag{27}$$

and again from Maxwell's equations for the static case and no currents

$$\nabla\times(\mathbf{H}_0 + \mathbf{H}_d) = 0. \tag{28}$$

The magnetostatic field $\mathbf{H}_d(\mathbf{r})$ can be written as the sum of the surface demagnetizing field $\mathbf{H}_d^s(\mathbf{r})$ and of the magnetostatic field $\mathbf{H}_d^b(\mathbf{r})$ which is related to volume charges, i.e.

$$\mathbf{H}_d(\mathbf{r}) = \mathbf{H}_d^s(\mathbf{r}) + \mathbf{H}_d^b(\mathbf{r}). \tag{29}$$

In the high-field limit (when the magnetization is close to saturation) and for samples with an ellipsoidal shape with $\mathbf{H}_0$ directed along a principal axis of the ellipsoid, one may approximate the demagnetizing field due to the surface charges by the *uniform* field

$$\mathbf{H}_d^s = -N\,M_s\,\mathbf{e}_z, \tag{30}$$

where $0 < N < 1$ denotes the corresponding demagnetizing factor. In Fourier space (at $\mathbf{q} \neq 0$), the above magnetostatic relations suggest the following expression for the Fourier coefficient $\mathbf{h}_d^b(\mathbf{q})$ of $\mathbf{H}_d^b(\mathbf{r})$ [133],

$$\begin{aligned}\mathbf{h}_d^b(\mathbf{q}) &= \left(h_{d,x}^b(\mathbf{q}), h_{d,y}^b(\mathbf{q}), h_{d,z}^b(\mathbf{q})\right)\\ &= -\frac{\mathbf{q}\,[\mathbf{q}\,\widetilde{\mathbf{M}}(\mathbf{q})]}{q^2},\end{aligned} \tag{31}$$

where

$$\mathbf{H}_d^b(\mathbf{r}) = \frac{1}{(2\pi)^{3/2}}\int \mathbf{h}_d^b(\mathbf{q})\,\exp(\mathrm{i}\mathbf{q}\mathbf{r})\,\mathrm{d}^3q \tag{32}$$

and

$$\widetilde{\mathbf{M}}(\mathbf{q}) = \left(\widetilde{M}_x(\mathbf{q}), \widetilde{M}_y(\mathbf{q}), \widetilde{M}_z(\mathbf{q})\right) \tag{33}$$

represents the Fourier transform of the magnetization $\mathbf{M}(\mathbf{r})$,

$$\mathbf{M}(\mathbf{r}) = \frac{1}{(2\pi)^{3/2}}\int \widetilde{\mathbf{M}}(\mathbf{q})\,\exp(\mathrm{i}\mathbf{q}\mathbf{r})\,\mathrm{d}^3q. \tag{34}$$

By inserting equations (21)–(24) and equations (29)–(34) into equations (19) and (20) and neglecting terms of higher than linear order in M_x or M_y, including terms such as $H_{d,i}^b M_x$ or $H_{d,i}^b M_y$ (where $i = x, y, z$), we obtain, in Fourier space, the following set of linear equations for $\widetilde{M}_x$ and $\widetilde{M}_y$ [115]:

$$\frac{2A}{\mu_0 M_s^2}\,q^2\,\widetilde{M}_x + \frac{H_i}{M_s}\,\widetilde{M}_x - h_{d,x}^b - h_x = 0, \tag{35}$$

$$\frac{2A}{\mu_0 M_s^2}\,q^2\,\widetilde{M}_y + \frac{H_i}{M_s}\,\widetilde{M}_y - h_{d,y}^b - h_y = 0. \tag{36}$$

Note that the Cartesian components of $\mathbf{h}_d^b$ depend also only linearly on the components of $\widetilde{\mathbf{M}}$ (compare equation (31)).

For a general orientation of the wave vector $\mathbf{q} = (q_x, q_y, q_z)$, the solutions for $\widetilde{M}_x(\mathbf{q})$ and $\widetilde{M}_y(\mathbf{q})$ can be then written as [53]

$$\widetilde{M}_x(\mathbf{q}) = M_s \frac{\left(h_x - \widetilde{M}_z \frac{q_x q_z}{q^2}\right)\left(H_{\text{eff}} + M_s \frac{q_y^2}{q^2}\right) - M_s \frac{q_x q_y}{q^2}\left(h_y - \widetilde{M}_z \frac{q_y q_z}{q^2}\right)}{H_{\text{eff}}\left(H_{\text{eff}} + M_s \frac{q_x^2+q_y^2}{q^2}\right)}, \tag{37}$$

$$\widetilde{M}_y(\mathbf{q}) = M_s \frac{\left(h_y - \widetilde{M}_z \frac{q_y q_z}{q^2}\right)\left(H_{\text{eff}} + M_s \frac{q_x^2}{q^2}\right) - M_s \frac{q_x q_y}{q^2}\left(h_x - \widetilde{M}_z \frac{q_x q_z}{q^2}\right)}{H_{\text{eff}}\left(H_{\text{eff}} + M_s \frac{q_x^2+q_y^2}{q^2}\right)}. \tag{38}$$

Note that both Fourier coefficients $\widetilde{M}_x(\mathbf{q})$ and $\widetilde{M}_y(\mathbf{q})$ depend explicitly on the longitudinal magnetization Fourier coefficient $\widetilde{M}_z(\mathbf{q})$. Since $\widetilde{M}_z \propto \Delta M$ [148], this term models inhomogeneities in the magnetic microstructure that are due to jumps in the magnetization at internal interfaces. The corresponding expressions for $\widetilde{M}_x$ and $\widetilde{M}_y$ for the single-phase material case do not contain such terms (compare equations (2.15) in [26]). Analytical micromagnetic calculations of the type presented here have already been carried out by other authors, for instance for the study of the approach to magnetic saturation [148–151].

The quantity

$$H_{\text{eff}}(q, H_i) = H_i\left(1 + l_H^2 q^2\right) \tag{39}$$

denotes the effective magnetic field (not to be confused with the effective field of equation (19)), which depends on the internal (applied) field $H_i = H_0 - NM_s$, on $q = |\mathbf{q}|$, and on the exchange length of the field

$$l_H(H_i) = \sqrt{\frac{2A}{\mu_0 M_s H_i}}. \tag{40}$$

The length scale l_H may take on values between a few nanometers and a few hundred nanometers (compare figure 2 in [26]), and it characterizes the range over which perturbations in the spin structure decay [53, 63, 66]. Likewise, when magnetostrictive interactions are explicitly taken into account, then an additional exchange length of the stress appears [116],

$$l_\sigma = \sqrt{\frac{2A}{3\lambda\sigma}}, \tag{41}$$

where λ is a magnetostriction constant and σ is some appropriate average of the internal stress; for typical values of λ and σ, l_σ takes on values of the order of a few 10 nm [116]. Such length scales can also be probed with SANS. H_{eff} consists of a contribution due to the internal field H_i and the exchange field $2Aq^2/(\mu_0 M_s)$. An increase of H_i increases the effective magnetic field only at the smallest q values, whereas H_{eff} at the larger q is always very large ($\sim$10 T) and independent of H_i (compare figure 2 in [26]). Since H_{eff} appears predominantly in the denominators of the expressions for $\widetilde{M}_x$ and $\widetilde{M}_y$, its role is to suppress the high-q Fourier components of the magnetization, which correspond to sharp real-space fluctuations. On the other hand, long-range magnetization fluctuations, at small q, are effectively suppressed when H_i is increased.

We would particularly like to emphasize that in deriving equations (37) and (38), no assumption was made about the particular form of the magnetic anisotropy (magnetocrystalline and/or magnetoelastic). Rather, we formally operate with the Fourier coefficient $\mathbf{h}(\mathbf{q})$ of $\mathbf{H}_p(\mathbf{r})$. As we will see in section 4, analysis of magnetic-field-dependent SANS data allows one to determine model-independently the squared magnitude of the magnetic anisotropy field.

At this point, we find it appropriate to pause and to recall the approximations made during the calculation. Besides the small-misalignment approximation ($M_x \ll M_s$ and $M_y \ll M_s$), we have introduced (at least) the following further approximations: (i) The exchange interaction is assumed to be homogeneous, i.e. $A =$ constant and jumps in this quantity (e.g. in a two-phase magnet) are not taken into account. Such an approximation is permissible as long as exchange fluctuations are not too large, in particular, for soft magnetic materials [134]. (ii) The function $\widetilde{M}_z(\mathbf{q})$ is introduced into our theory only in $\mathbf{q}$-space via $\mathbf{h}_d^b(\mathbf{q}) = -\mathbf{q}\,[\mathbf{q}\,\widetilde{\mathbf{M}}(\mathbf{q})]/q^2$ (equation (31)). This is an approximation, since in real space we have assumed that $M_z \cong M_s =$ constant, and hence $\widetilde{M}_z(\mathbf{q}) \propto \delta(\mathbf{q})$ would result, as is appropriate for a homogeneous single-phase material. However, by explicitly considering only the $\mathbf{q} \neq 0$ Fourier coefficients of $\widetilde{M}_z$, it becomes possible to directly include jumps in the longitudinal magnetization (e.g. at particle-matrix interfaces), and to avoid the otherwise necessary calculation of convolution products [148–150]. (iii) The combined magnetocrystalline and magnetoelastic anisotropy-energy density is assumed to depend only linearly on the components of the magnetization. This then implies that the anisotropy field $\mathbf{H}_p$, which enters the balance-of-torques equation, is independent of $\mathbf{M}$ and, hence, independent of the applied magnetic field.

2.3. Connecting micromagnetics and SANS

For the following discussion of magnetic SANS, it is of interest to consider special projections of equations (37) and (38) into the plane of the two-dimensional detector. The two scattering geometries which are of particular relevance to experiment have the external magnetic field $\mathbf{H}_0$ either perpendicular or parallel to the wave vector $\mathbf{k}_0$ of the incoming neutron beam (compare figure 6). For $\mathbf{k}_0 \parallel \mathbf{e}_x$ and $\mathbf{H}_0 \parallel \mathbf{e}_z$, the scattering vector can be approximated as $\mathbf{q} \cong (0, q_y, q_z) = q\,(0, \sin\theta, \cos\theta)$, i.e. $q_x \cong 0$, and equations (37) and (38) reduce to

$$\widetilde{M}_x(\mathbf{q}) = M_s \frac{h_x(\mathbf{q})}{H_{\text{eff}}}, \tag{42}$$

$$\widetilde{M}_y(\mathbf{q}) = M_s \frac{h_y(\mathbf{q}) - \widetilde{M}_z(\mathbf{q})\frac{q_y q_z}{q^2}}{H_{\text{eff}} + M_s \frac{q_y^2}{q^2}}. \tag{43}$$

For $\mathbf{k}_0 \parallel \mathbf{H}_0 \parallel \mathbf{e}_z$, $\mathbf{q} \cong (q_x, q_y, 0) = q\,(\cos\theta, \sin\theta, 0)$, i.e. $q_z \cong 0$, and the results for the Fourier coefficients simplify to

$$\widetilde{M}_x(\mathbf{q}) = M_s \frac{h_x(\mathbf{q})\left(H_{\text{eff}} + M_s \frac{q_y^2}{q^2}\right) - h_y(\mathbf{q}) M_s \frac{q_x q_y}{q^2}}{H_{\text{eff}}\left(H_{\text{eff}} + M_s\right)}, \tag{44}$$

$$\widetilde{M}_y(\mathbf{q}) = M_s \frac{h_y(\mathbf{q})\left(H_{\text{eff}} + M_s \frac{q_x^2}{q^2}\right) - h_x(\mathbf{q}) M_s \frac{q_x q_y}{q^2}}{H_{\text{eff}}\,(H_{\text{eff}} + M_s)}. \tag{45}$$

Note that equations (44) and (45) are independent of $\widetilde{M}_z$ and similar to equations (2.15) in [26]. Furthermore, in equations (42)–(45) we have made use of the 'usual' small-angle approximation, which neglects the component of the scattering vector along the direction of the incident beam. This approximation might not be justified anymore at large scattering angles, where typically SANS from objects of the order of a nanometer is probed.

Both Fourier coefficients $\widetilde{M}_x(\mathbf{q})$ and $\widetilde{M}_y(\mathbf{q})$ can be considered as a sum of products of components of the anisotropy-field Fourier coefficient $\mathbf{h}(\mathbf{q})$ and $\widetilde{M}_z(\mathbf{q})$ with micromagnetic functions, which contain the effective magnetic field H_{eff} and terms that depend on the orientation of the wavevector (e.g. $M_s q_y^2/q^2$). The convolution theorem then implies that the magnetic microstructure in real space, $\mathbf{M}(\mathbf{r})$, is tantamount to a complicated convolution product between the corresponding real-space functions. As a consequence, sharp features in the nuclear or anisotropy-field microstructure are washed out and smoothly-varying magnetization profiles are at the origin of the related spin-misalignment scattering. Consistent with this notion is the observation of power-law exponents significantly larger than 4 and the finding that the slope of the correlation function at the origin vanishes (see section 5 below) [152].

Since the magnetic SANS cross-section $\mathrm{d}\Sigma/\mathrm{d}\Omega$ depends on the squared magnitudes of the magnetization Fourier coefficients (compare sections 3.3–3.5), it is necessary to compute appropriate averages of these functions. For this purpose, we assume that the Fourier coefficient of the anisotropy field is isotropically distributed in the plane perpendicular to $\mathbf{H}_0$,

$$\mathbf{h}(\mathbf{q}) = (h(\mathbf{q})\cos\beta, h(\mathbf{q})\sin\beta, 0)\,, \tag{46}$$

where the angle β specifies the orientation of $\mathbf{h}$. In other words, we assume that the vector $\mathbf{h}(\mathbf{q})$ takes on all orientations (i.e. angles β) with equal probability. This allows us to average $\widetilde{M}_x^2(q,\theta,H_i,\beta)$, $\widetilde{M}_y^2(q,\theta,H_i,\beta)$, and both cross terms $-2\widetilde{M}_y\widetilde{M}_z$ and $-2\widetilde{M}_x\widetilde{M}_y$ over β, i.e.

$$\frac{1}{2\pi}\int_0^{2\pi} (\ldots)\,\mathrm{d}\beta. \tag{47}$$

For $\mathbf{k}_0 \perp \mathbf{H}_0$, this results in

$$\widetilde{M}_x^2(q,\theta,H_i) = M_s^2 \frac{h^2(\mathbf{q})}{2H_{\text{eff}}^2(q,H_i)}, \tag{48}$$

$$\widetilde{M}_y^2(q,\theta,H_i) = M_s^2 \frac{h^2(\mathbf{q}) + 2\widetilde{M}_z^2(\mathbf{q})\sin^2\theta\cos^2\theta}{2\left[H_{\text{eff}}(q,H_i) + M_s\sin^2\theta\right]^2}, \tag{49}$$

$$-2\widetilde{M}_y\widetilde{M}_z = M_s \frac{2\widetilde{M}_z^2(\mathbf{q})\sin\theta\cos\theta}{H_{\text{eff}}(q,H_i) + M_s\sin^2\theta}, \tag{50}$$

whereas for $\mathbf{k}_0 \parallel \mathbf{H}_0$, we obtain

$$\widetilde{M}_x^2 = M_s^2\,h^2(\mathbf{q})\,\frac{\left[H_{\text{eff}}(q,H_i) + M_s\sin^2\theta\right]^2 + M_s^2\sin^2\theta\cos^2\theta}{2H_{\text{eff}}^2(q,H_i)\left[H_{\text{eff}}(q,H_i) + M_s\right]^2}, \tag{51}$$

$$\widetilde{M}_y^2 = M_s^2\,h^2(\mathbf{q})\,\frac{\left[H_{\text{eff}}(q,H_i) + M_s\cos^2\theta\right]^2 + M_s^2\sin^2\theta\cos^2\theta}{2H_{\text{eff}}^2(q,H_i)\left[H_{\text{eff}}(q,H_i) + M_s\right]^2}, \tag{52}$$

$$-2\widetilde{M}_x\widetilde{M}_y = M_s^2\,h^2(\mathbf{q})\,\frac{M_s\left[2H_{\text{eff}}(q,H_i) + M_s\right]\sin\theta\cos\theta}{H_{\text{eff}}^2(q,H_i)\left[H_{\text{eff}}(q,H_i) + M_s\right]^2}. \tag{53}$$

In writing down equations (48)–(53), we have treated all functions as real-valued. We have also assumed that the longitudinal Fourier coefficient $\widetilde{M}_z$ is independent of the orientation of the anisotropy field, which may be approximately valid for polycrystalline bulk ferromagnets in the approach-to-saturation regime. Note also that interference terms $\propto h_y\widetilde{M}_z$ or $h_x h_y$ vanish in this averaging procedure. The case of a texture present in the orientation distribution of the anisotropy field is treated in the appendix of [62].

For the later derivation of the spin-misalignment SANS cross-sections (section 4), it is convenient to introduce the dimensionless function

$$p(q,H_i) = \frac{M_s}{H_{\text{eff}}(q,H_i)} = \frac{M_s}{H_i(1 + l_H^2 q^2)} \tag{54}$$

(see figure 12(*a*)) and to re-express equations (48)–(53) in terms of p. We then obtain for the squared Fourier components and cross terms:

$$\widetilde{M}_x^2 = \frac{h^2 p^2}{2}, \tag{55}$$

$$\widetilde{M}_y^2 = \frac{h^2 p^2 + 2\widetilde{M}_z^2 p^2\sin^2\theta\cos^2\theta}{2\left(1 + p\sin^2\theta\right)^2}, \tag{56}$$

$$-2\widetilde{M}_y\widetilde{M}_z = \frac{2\widetilde{M}_z^2 p\sin\theta\cos\theta}{\left(1 + p\sin^2\theta\right)}, \tag{57}$$

in perpendicular ($\mathbf{k}_0 \perp \mathbf{H}_0$) and

$$\widetilde{M}_x^2 = h^2\,p^2\,\frac{\left(1 + p\sin^2\theta\right)^2 + p^2\sin^2\theta\cos^2\theta}{2\,(1+p)^2}, \tag{58}$$

$$\widetilde{M}_y^2 = h^2\,p^2\,\frac{\left(1 + p\cos^2\theta\right)^2 + p^2\sin^2\theta\cos^2\theta}{2\,(1+p)^2}, \tag{59}$$

$$-2\widetilde{M}_x\widetilde{M}_y = h^2\,p^2\,\frac{p\,(2+p)\sin\theta\cos\theta}{(1+p)^2}, \tag{60}$$

in parallel ($\mathbf{k}_0 \parallel \mathbf{H}_0$) geometry. The above Fourier coefficients only need to be multiplied by the corresponding trigonometric functions (and summed up) in order to obtain the magnetic SANS cross-section for the respective scattering geometry. Note also the symmetry of the transversal Fourier coefficients in the parallel scattering geometry (equations (58) and (59)), which is absent in the perpendicular case (equations (55) and (56)).

Figures 4 and 5 show the applied-field dependence of the above Fourier coefficients. For the functions h^2 and $\widetilde{M}_z^2$, we have for simplicity assumed the form factor of the sphere

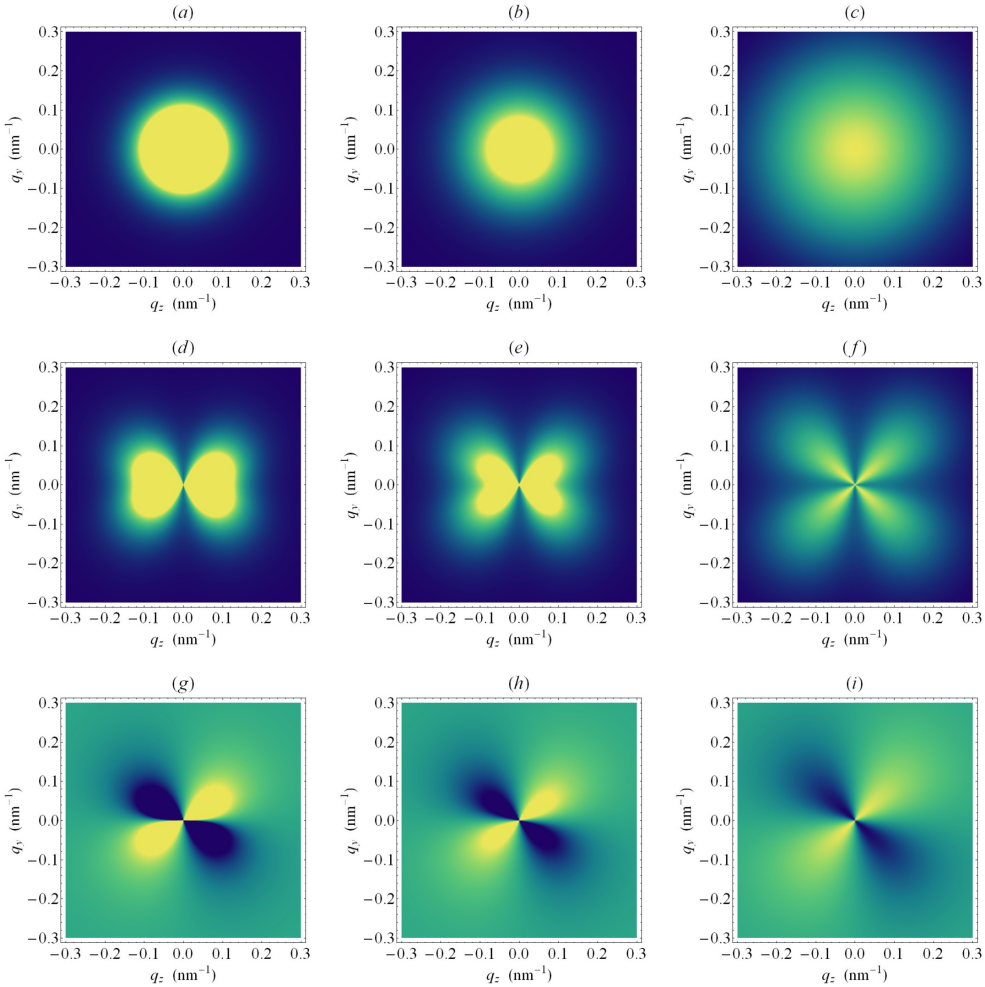

Figure 4. Contour plots of $\widetilde{M}_x^2$ (upper row), $\widetilde{M}_y^2$ (middle row), and $-2\widetilde{M}_y\widetilde{M}_z$ (lower row) for $\mathbf{k}_0 \perp \mathbf{H}_0$ at selected applied magnetic fields (equations (55)–(57)). $\mathbf{H}_0 \parallel \mathbf{e}_z$ is horizontal. For $h^2(qR)$ and $\widetilde{M}_z^2(qR)$, we used the form factor of the sphere with a radius of $R = 8$ nm (equations (104) and (105)). Materials parameters: $A = 2.5 \times 10^{-11}$ J/m; $\mu_0 M_s = 1.5$ T; $\mu_0 H_p = 0.125$ T; $\mu_0 \Delta M = 0.25$ T ($H_p/\Delta M = 1/2$). H_i values (in T) from left to right column: 0.1; 1.0; 10.0. In (a)–(f), yellow colour corresponds to 'high intensity' and blue colour to 'low intensity', whereas in (g)–(i) yellow colour corresponds to positive and blue colour to negative values of $-2\widetilde{M}_y\widetilde{M}_z$.

(see equations (104) and (105) below). It is seen that for the transversal scattering geometry ($\mathbf{k}_0 \perp \mathbf{H}_0$), $\widetilde{M}_x^2$ is isotropic at all fields, whereas $\widetilde{M}_y^2$ is highly anisotropic, with a characteristic 'clover-leaf-shaped' angular anisotropy. For the parallel case ($\mathbf{k}_0 \parallel \mathbf{H}_0$), $\widetilde{M}_x^2$ and $\widetilde{M}_y^2$ are both strongly anisotropic with characteristic maxima in the plane perpendicular to $\mathbf{H}_0$. Note that in the considered high-field regime, the Fourier coefficient $|\widetilde{M}_z|^2$ is (for polycrystalline bulk ferromagnets) isotropic and approximately independent of the applied magnetic field. It is also worth mentioning that due to the $\sin\theta\cos\theta$ term, both cross terms ($-2\widetilde{M}_y\widetilde{M}_z$ and $-2\widetilde{M}_x\widetilde{M}_y$) change their sign at the border of quadrants on the detector. However, when both cross terms are multiplied with the additional factor $\sin\theta\cos\theta$, in order to arrive at the contribution to the respective cross-section (compare, e.g. equations (77) and (78)), they turn into positive definite contributions. The results in figures 4 and 5 agree qualitatively with the micromagnetic simulations reported in [31].

It is very important to note that the angular anisotropy (θ-dependence) present in the Fourier coefficients is a consequence of the magnetodipolar interaction: neglecting this contribution results (for isotropic $\mathbf{h}$) in isotropic Fourier coefficients, which do not reproduce the experimentally observed clover-leaf anisotropy [46, 60, 65, 76]. These observations underline the importance of the magnetodipolar interaction for understanding magnetic SANS.

The above expressions for the Fourier coefficients are quite generally valid for bulk magnetic materials in the approach-to-saturation regime. In particular, the cross terms are believed to be of relevance for practically all bulk ferromagnets, where the magnetodipolar interaction is an almost inevitable part of the total magnetic energy: whenever the divergence of $\mathbf{M}$ is nonzero, one has a magnetostatic field, which, by virtue of the anisotropic character of the dipole-dipole interaction, gives rise to θ-dependent Fourier coefficients and cross-sections. Whether or not the cross terms show up in experimental SANS data is of course only a question of their magnitude relative to the other Fourier coefficients $\widetilde{M}_x^2$ and $\widetilde{M}_y^2$. For example, since $\widetilde{M}_z \propto \Delta M$, one may expect that the cross term $-2\widetilde{M}_y\widetilde{M}_z \sin\theta\cos\theta$ makes only a small contribution to the overall cross-section of a single-phase ferromagnet with homogeneous saturation magnetization (compare figure 23(b) and figure 8 in [31]).

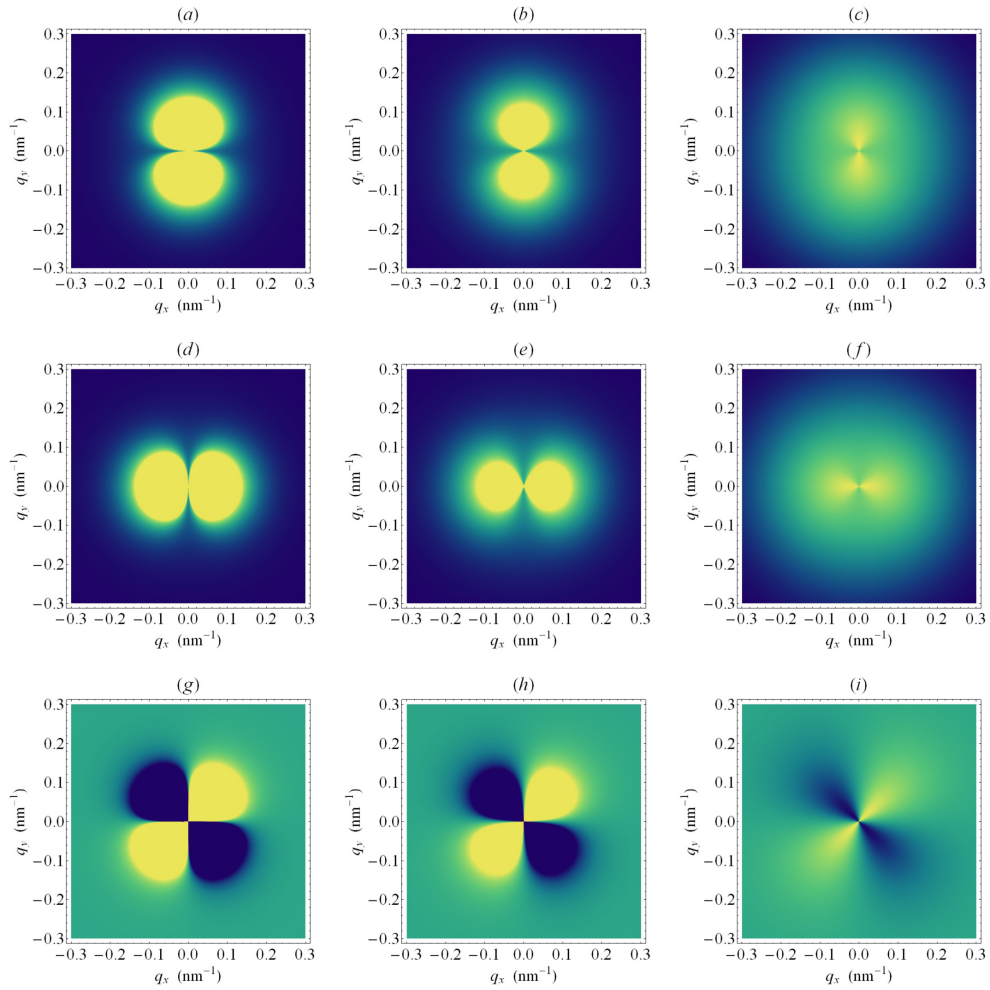

Figure 5. Contour plots of $\widetilde{M}_x^2$ (upper row), $\widetilde{M}_y^2$ (middle row), and $-2\widetilde{M}_x\widetilde{M}_y$ (lower row) for $\mathbf{k}_0 \parallel \mathbf{H}_0$ at selected applied magnetic fields (equations (58)–(60)). $\mathbf{H}_0 \parallel \mathbf{e}_z$ points into the detector plane. Form factors for $h^2(qR)$ and $\widetilde{M}_z^2(qR)$ and materials parameters are the same as in figure 4. H_i values (in T) from left to right column: 0.1; 1.0; 10.0. In (a)–(f), yellow colour corresponds to 'high intensity' and blue colour to 'low intensity', whereas in (g)–(i) yellow colour corresponds to positive and blue colour to negative values of $-2\widetilde{M}_x\widetilde{M}_y$.

3. SANS cross-sections

The purpose of this section is to display in a compact manner the relevant expressions for the SANS cross-sections of magnetic materials. Magnetic SANS, in contrast to magnetic (small-angle) neutron diffraction, which is used, e.g. to study the vortex lattice of superconductors [29] or skyrmion structures [153], measures the diffuse scattering along the forward direction which arises from nanoscale variations in the magnetic microstructure [20, 21, 26, 27]. The unique strength of the SANS technique resides in the fact that it probes *bulk* properties on a length scale from a few to a few hundred nanometers. Since magnetic SANS experiments typically employ cold neutrons (with wavelengths above the Bragg cuttoff, $\lambda \gtrsim 5$ Å), the discrete atomic structure of condensed matter is generally of no relevance, and the magnetization state of the sample can be represented by a *continuous* magnetization vector field $\mathbf{M}(\mathbf{r})$, where $\mathbf{r}$ denotes the position vector inside the material. Magnetic SANS is a consequence of nanoscale variations in both the *orientation* and/or *magnitude* of $\mathbf{M}$.

Typical SANS instrumentation does not allow for energy analysis of the scattered neutrons and the measurable quantity-the energy-integrated macroscopic differential scattering cross-section $\mathrm{d}\Sigma/\mathrm{d}\Omega$ at scattering vector $\mathbf{q}$-is a function of the magnetization Fourier coefficients $\widetilde{\mathbf{M}}(\mathbf{q})$. These Fourier coefficients depend in a complicated manner on the magnetic interactions (e.g. exchange, magnetic anisotropy, magnetodipolar interaction), the underlying microstructure (particle-size distribution or crystallographic texture), and on the applied magnetic field. The continuum theory of micromagnetics [114–117] is designed to compute spin structure on a mesoscopic length scale (∼1–1000 nm) [154], which overlaps with the resolution range of the SANS technique. It is therefore straightforward to calculate SANS cross-sections based on micromagnetic theory.

Since we are specifically interested in the *static* magnetic microstructure of bulk ferromagnets, which is probed by *elastic* scattering, it is necessary to estimate the influence of inelastic scattering to the energy-integrated cross-section. Potential sources of inelastic scattering contributions to $\mathrm{d}\Sigma/\mathrm{d}\Omega$ are spin waves (magnons) [155, 156] and lattice vibrations (phonons). As discussed in section 3.5 of [26], throughout the *major* part of the parameter space which is probed in typical SANS experiments, the requirements of momentum and energy

conservation upon absorption or emission of a magnon or phonon cannot be satisfied simultaneously for any scattering vector in the small-angle regime, in particular at large applied fields or for strongly anisotropic materials. However, the so-called left-right asymmetry method [157], which employs the initial low-q magnon dispersion, allows one to measure the spin-wave stiffness constant of magnetic materials (using polarized SANS in inclined field geometry). See also the article by Maleev [158] for a discussion on inelastic SANS.

Before displaying the fully spin-resolved SANS cross-sections (section 3.3), the half-polarized cross-sections (section 3.4), and the unpolarized $\mathrm{d}\Sigma/\mathrm{d}\Omega$ (section 3.5), we briefly describe in section 3.1 the main features and the typical setup of a SANS instrument. Section 3.2 introduces the nomenclature, whereas section 3.6 provides a discussion of the cross-sections in the completely saturated magnetization state (at large applied magnetic field), which is often taken as a reference for data recorded at lower fields.

3.1. Description of the SANS setup

Figure 6 shows schematically the typical SANS setup along with sketches of the two most commonly used scattering geometries. Cold neutrons, which emerge from a nuclear reactor or from a spallation source, are monochromatized by means of a mechanical velocity selector. Depending on the rotational speed and tilting angle of the selector drum relative to the incident neutron-beam direction, a mean wavelength between about 5 and 20 Å and with a wavelength resolution $\Delta\lambda/\lambda$ between 10 and 30% (full width at half maximum) can be selected. In the evacuated pre-sample flight path (source-to-sample distance ∼1–20 m), a set of circular pinholes collimates the monochromatized beam. A particular strength of the SANS technique is that experiments can be conducted under rather flexible conditions and under different sample environments (temperature, electric and magnetic field, pressure, neutron polarization, time-resolved data acquisition, etc.). The typical size of the irradiated area of sample is of the order of 1 cm^2.

A two-dimensional position-sensitive detector, moving along rails in an evacuated post-sample flight path (sample-to-detector ∼1–20 m), counts the scattered neutrons during acquisition times ranging between a few minutes and a few hours. The recorded neutron counts (in each pixel element of the detector) are corrected for detector dead time, normalized to incident-beam monitor counts, and a solid-angle correction is applied to the data which corrects for the planar geometry of the detector; further corrections relate to sample transmission, background scattering, detector dark current and detector efficiency. The scattering cross-section of the sample is obtained by comparing the corrected signal to that of a reference sample (e.g. water, polystyrene, porous silica, vanadium single crystal) of known cross-section. The data-reduction procedure provides the macroscopic differential scattering cross-section $\mathrm{d}\Sigma/\mathrm{d}\Omega$ of the sample in absolute units (typically $\mathrm{cm}^{-1}\,\mathrm{sr}^{-1}$) and as a function of the magnitude and orientation of the momentum-transfer or scattering vector $\mathbf{q}$ (see figure 6). In order to conveniently present the

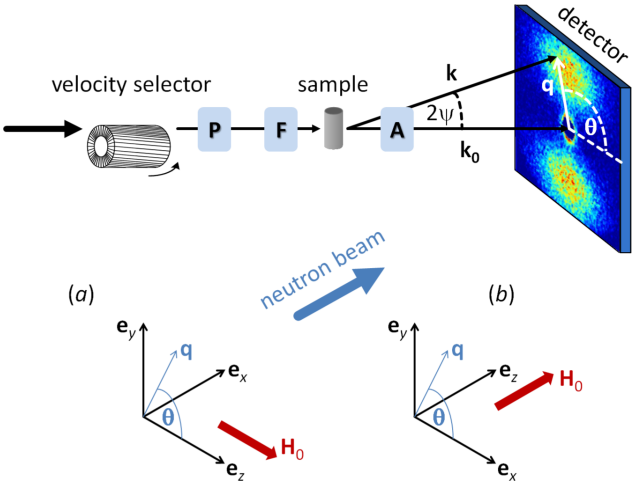

Figure 6. Sketch of the SANS setup and of the two most often employed scattering geometries in magnetic SANS experiments. (*a*) $\mathbf{k}_0 \perp \mathbf{H}_0$; (*b*) $\mathbf{k}_0 \parallel \mathbf{H}_0$. The scattering vector $\mathbf{q}$ is defined as the difference between the wave vectors of the scattered and incident neutrons, i.e. $\mathbf{q} = \mathbf{k} - \mathbf{k}_0$; its magnitude $q = |\mathbf{q}| = (4\pi/\lambda)\sin\psi$ depends on the mean wavelength λ of the neutrons (selected by the velocity selector) and on the scattering angle 2ψ. The symbols 'P', 'F', and 'A' denote, respectively, the polarizer, spin flipper, and analyzer. SANS is usually implemented as elastic scattering ($k_0 = k = 2\pi/\lambda$), and the component of $\mathbf{q}$ along the incident neutron beam (i.e. q_x in (*a*) and q_z in (*b*)) is neglected. The angle θ may be conveniently used in order to describe the angular anisotropy of the recorded scattering pattern on a two-dimensional position-sensitive detector.

neutron data, one often carries out a so-called azimuthal averaging procedure, whereby the data at a constant magnitude of $\mathbf{q}$ are summed up (integrated) within a certain angular range (e.g. by 360°); this yields $\mathrm{d}\Sigma/\mathrm{d}\Omega$ as a function of $|\mathbf{q}| = q$. As quoted in [159], the uncertainty in the cross-sections determined by this procedure is estimated to be 5–10%. Since $q = (4\pi/\lambda)\sin\psi$, where 2ψ denotes the scattering angle, different momentum transfers (scattering angles) can be accessed by varying the distance between the sample and the detector. With conventional SANS instruments it becomes thus possible to cover a q-range of $0.01\,\mathrm{nm}^{-1} \lesssim q \lesssim 5\,\mathrm{nm}^{-1}$, which translates into structure sizes of the order of 1–100 nm. The q-resolution of a SANS instrument is mainly related to the wavelength spread of the incident neutrons, the finite collimation of the beam, and the detector resolution (finite pixel size). For studies which describe the optimal instrument configuration, instrumental resolution (smearing) effects, the impact of gravitation, the data-reduction procedure, the performance of SANS instruments, or the treatment of multiple scattering see [5, 159–169] and references therein.

The neutrons incident on the sample may be polarized by means of a supermirror transmission polarizer and the initial neutron polarization can be reverted by 180° using a (radio-frequency) spin flipper [170, 171] (see figure 6). In magnetic SANS experiments, ^{3}He spin filters act as spin analyzers and, correspondingly, are installed behind the sample (sometimes inside the detector housing). Magnetic guide fields of the order of 1 mT serve to maintain the polarization between polarizer and ^{3}He filter. Recent progress in the development of

efficient ^{3}He spin filters [172] allows one to perform routinely uniaxial (also called longitudinal or one-dimensional) neutron-polarization analysis on a SANS instrument, for instance, at the instruments D22 and D33 at the Institut Laue-Langevin, Grenoble, France or at NG3 and NG7 at the NIST Center for Neutron Research, Gaithersburg, USA. The principle of operation of a ^{3}He spin polarizer/analyzer is based upon the strongly spin-dependent absorption of neutrons by a nuclear-spin-polarized gas of ^{3}He atoms [173]; only neutrons with spin component antiparallel to the ^{3}He nuclear spin are absorbed. The advantages of ^{3}He spin filters as compared to other polarizing/analyzing devices are (i) that they can be used over a rather broad wavelength band (from cold to thermal to hot neutrons) and (ii) that they allow for a rather large phase space (neutron-energy transfer and scattering angle) to be covered.

In uniaxial polarization analysis [174], the polarization of the scattered neutrons is analyzed in the direction parallel to that of the initial polarization (before entering the detector). The externally applied magnetic field at the sample position defines the quantization axis for both incident and scattered polarization. For more information on (polarized) neutron scattering (and on spherical neutron polarimetry), we refer the reader to the classic papers [108, 113, 174–184, 185] and textbooks [186–189].

With the above described setup it becomes possible to measure four intensities that connect two neutron-spin states. Following [174], the four partial scattering cross-sections are the two non-spin-flip quantities $\frac{\mathrm{d}\Sigma^{++}}{\mathrm{d}\Omega}$ and $\frac{\mathrm{d}\Sigma^{--}}{\mathrm{d}\Omega}$ and the two spin-flip cross-sections $\frac{\mathrm{d}\Sigma^{+-}}{\mathrm{d}\Omega}$ and $\frac{\mathrm{d}\Sigma^{-+}}{\mathrm{d}\Omega}$. When the rf flipper is off (inactive), we measure, depending on the spin state of the ^{3}He filter, the non-spin-flip or the spin-flip cross-section $\frac{\mathrm{d}\Sigma^{++}}{\mathrm{d}\Omega}$ or $\frac{\mathrm{d}\Sigma^{+-}}{\mathrm{d}\Omega}$. Likewise, when the flipper is on (active), we either measure $\frac{\mathrm{d}\Sigma^{--}}{\mathrm{d}\Omega}$ or $\frac{\mathrm{d}\Sigma^{-+}}{\mathrm{d}\Omega}$. In the context of magnetic SANS, the corresponding expressions for the cross-sections are denoted as the POLARIS equations (see section 3.3).

SANS experiments with a polarized incident beam only (and no detection of the polarization of the scattered neutrons) provide access to the so-called SANSPOL cross-sections $\frac{\mathrm{d}\Sigma^{+}}{\mathrm{d}\Omega}$ and $\frac{\mathrm{d}\Sigma^{-}}{\mathrm{d}\Omega}$. In particular (see section 3.4),

$$\frac{\mathrm{d}\Sigma^{+}}{\mathrm{d}\Omega} = \frac{\mathrm{d}\Sigma^{++}}{\mathrm{d}\Omega} + \frac{\mathrm{d}\Sigma^{+-}}{\mathrm{d}\Omega}, \tag{61}$$

$$\frac{\mathrm{d}\Sigma^{-}}{\mathrm{d}\Omega} = \frac{\mathrm{d}\Sigma^{--}}{\mathrm{d}\Omega} + \frac{\mathrm{d}\Sigma^{-+}}{\mathrm{d}\Omega}. \tag{62}$$

The difference between 'spin-up' and 'spin-down' SANSPOL cross-sections yields the polarization-dependent nuclear-magnetic and chiral scattering terms. As demonstrated, e.g. in [171] on an Fe_3O_4 glass ceramic, this difference allows one to highlight weak magnetic contributions relative to strong nuclear scattering (or vice versa). Finally, the unpolarized SANS cross-section is obtained as (see section 3.5)

$$\begin{aligned}\frac{\mathrm{d}\Sigma}{\mathrm{d}\Omega} &= \frac{1}{2}\left(\frac{\mathrm{d}\Sigma^{+}}{\mathrm{d}\Omega} + \frac{\mathrm{d}\Sigma^{-}}{\mathrm{d}\Omega}\right) \\ &= \frac{1}{2}\left(\frac{\mathrm{d}\Sigma^{++}}{\mathrm{d}\Omega} + \frac{\mathrm{d}\Sigma^{--}}{\mathrm{d}\Omega} + \frac{\mathrm{d}\Sigma^{+-}}{\mathrm{d}\Omega} + \frac{\mathrm{d}\Sigma^{-+}}{\mathrm{d}\Omega}\right).\end{aligned} \tag{63}$$

3.2. Nomenclature and simplifications

In the equations for the various cross-sections that follow, V denotes the scattering volume,

$$b_H = 2.70 \times 10^{-15}\,\mathrm{m}\,\mu_\mathrm{B}^{-1} = 2.91 \times 10^{8}\,\mathrm{A}^{-1}\mathrm{m}^{-1} \tag{64}$$

is a constant (see below), $\widetilde{N}(\mathbf{q})$ is the nuclear scattering amplitude, and

$$\widetilde{\mathbf{M}}(\mathbf{q}) = \left[\widetilde{M}_x(\mathbf{q}), \widetilde{M}_y(\mathbf{q}), \widetilde{M}_z(\mathbf{q})\right], \tag{65}$$

represents the Fourier coefficient of the magnetization vector field

$$\mathbf{M}(\mathbf{r}) = \left[M_x(\mathbf{r}), M_y(\mathbf{r}), M_z(\mathbf{r})\right]; \tag{66}$$

c^* is a quantity complex-conjugated to c. We adopt a Cartesian laboratory coordinate system with corresponding unit vectors $\mathbf{e}_x$, $\mathbf{e}_y$, and $\mathbf{e}_z$. $\mathbf{H}_0$ is assumed to be always parallel to $\mathbf{e}_z$, so that $\widetilde{M}_z(\mathbf{q})$ denotes the corresponding *longitudinal* magnetization Fourier coefficient, and $\widetilde{M}_x(\mathbf{q})$ and $\widetilde{M}_y(\mathbf{q})$ are the *transversal* components, giving rise to spin-misalignment scattering. For $\mathbf{k}_0 \perp \mathbf{H}_0$, the angle θ is then measured between $\mathbf{H}_0$ and

$$\mathbf{q} \cong q\ (0, \sin\theta, \cos\theta)\,, \tag{67}$$

whereas for $\mathbf{k}_0 \parallel \mathbf{H}_0$, θ is the angle between $\mathbf{e}_x$ and

$$\mathbf{q} \cong q\ (\cos\theta, \sin\theta, 0) \tag{68}$$

(compare figure 6). In these expressions for $\mathbf{q}$, we have made use of the small-angle approximation (note that typically $2\psi \lesssim 10^\circ$), i.e. the magnitude of the component of $\mathbf{q}$ along the incident-beam direction is negligible as compared to the other two components. The atomic magnetic form factor $f(\mathbf{q})$ in the expression for the atomic magnetic scattering amplitude

$$b_m = 2.70 \times 10^{-15}\,\mathrm{m}\ f(\mathbf{q})\,\frac{\mu_a}{\mu_\mathrm{B}} = b_H\,\mu_a \tag{69}$$

was set to unity, which is permissible along the forward direction (μ_a: atomic magnetic moment; μ_B: Bohr magneton).

In an attempt not to unnecessarily encumber the notation in the expressions for the POLARIS (and SANSPOL) cross-sections, we assume a perfectly working neutron optics, i.e. we set the efficiencies of the polarizer, analyzer, and spin flipper to unity. However, since in actual POLARIS experiments these devices are characterized by efficiencies close to but smaller than unity, it is necessary to measure all four partial cross-sections in order to correct for spin leakage between the different channels [190]. Such a correction can for example be accomplished by means of the *BERSANS* [191, 192] and *Pol-Corr* [193] software tools.

We would like to particularly emphasize that nuclear spin-incoherent SANS, which is partly spin-flip scattering, is neglected in the spin-flip SANS cross-sections (equations (72) and (74) below). This is motivated by the fact that its magnitude [18] is very small relative to the here relevant coherent magnetic SANS (compare e.g. the field-dependent $\frac{\mathrm{d}\Sigma^{+-}}{\mathrm{d}\Omega}$ shown in figure 23).

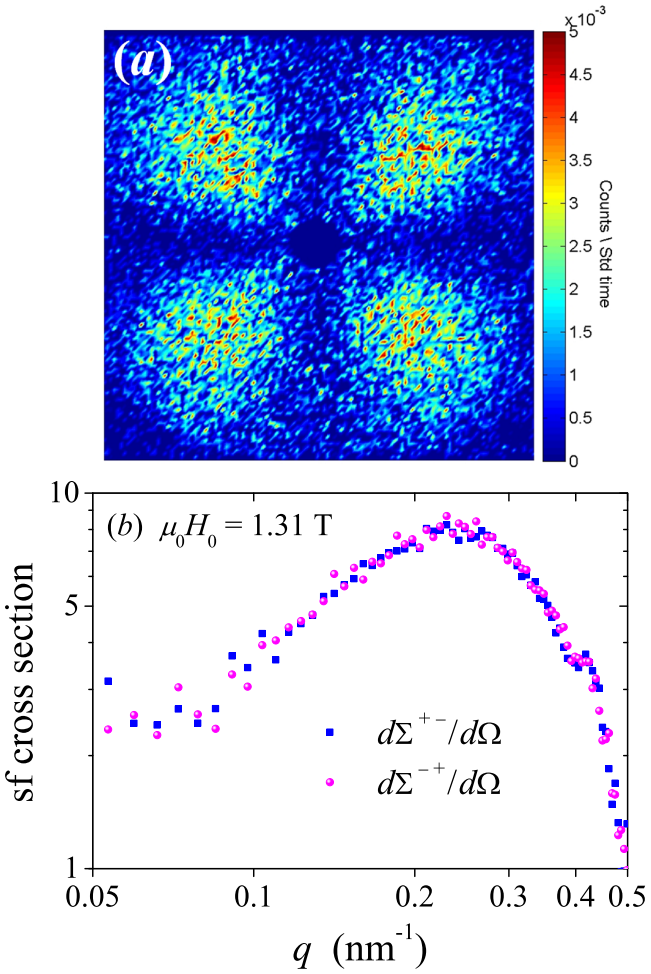

Figure 7. (*a*) Spin-flip SANS cross-section $\frac{d\Sigma^{+-}}{d\Omega}$ of an FeCr-based nanocomposite at a saturating applied magnetic field of 1.31 T ($\mathbf{k}_0 \perp \mathbf{H}_0$) (logarithmic colour scale). (*b*) Azimuthally-averaged spin-flip cross-sections $\frac{d\Sigma^{+-}}{d\Omega}$ and $\frac{d\Sigma^{-+}}{d\Omega}$ (log–log scale). Reproduced from [48] with permission from Springer Science & Business Media.

Furthermore, since the focus of this review article is on magnetic SANS of statistically isotropic polycrystalline bulk ferromagnets, polarization-dependent chiral scattering terms, proportional to

$$\mp \mathrm{i}\left(Q_x\, Q_y^* - Q_x^*\, Q_y\right), \tag{70}$$

where Q_x and Q_y denote the Cartesian components of the Halpern–Johnson vector [174], have also been ignored in the spin-flip cross-sections. Consequently, the two spin-flip cross-sections are independent of the incident neutron polarization, as is shown in figure 7 for the case of a nanocrystalline FeCr-based magnetic alloy [48].

As demonstrated, e.g. in [106], the polarization dependence of the chiral terms and the related asymmetry of the cross-section with respect to $\mathbf{q}$ may be employed for the study of crystal handedness and spin-helix chirality in non-centrosymmetric cubic single crystals.

Since the vast majority of magnetic SANS experiments are carried out by employing the two scattering geometries where the externally applied magnetic field $\mathbf{H}_0$ is either perpendicular (figure 6(*a*)) or parallel (figure 6(*b*)) to the wave vector $\mathbf{k}_0$ of the incoming neutron beam, we restrict our attention to these two specific situations. We refer the reader to [194] (and references therein) for a study of critical two and three-spin correlations in EuS which employs an inclined magnetic field geometry ($\mathbf{H}_0$ at 45° to $\mathbf{k}_0$).

3.3. POLARIS cross-sections

3.3.1. $\mathbf{k}_0 \perp \mathbf{H}_0$.

$$\begin{aligned}\frac{\mathrm{d}\Sigma^{\pm\pm}}{\mathrm{d}\Omega}(\mathbf{q}) = \frac{8\pi^3}{V}\big(&|\widetilde{N}|^2 + b_H^2|\widetilde{M}_y|^2\sin^2\theta\cos^2\theta \\ &+ b_H^2|\widetilde{M}_z|^2\sin^4\theta \\ &- b_H^2(\widetilde{M}_y\widetilde{M}_z^* + \widetilde{M}_y^*\widetilde{M}_z)\sin^3\theta\cos\theta \\ &\mp b_H(\widetilde{N}\widetilde{M}_z^* + \widetilde{N}^*\widetilde{M}_z)\sin^2\theta \\ &\pm b_H(\widetilde{N}\widetilde{M}_y^* + \widetilde{N}^*\widetilde{M}_y)\sin\theta\cos\theta\big).\end{aligned} \tag{71}$$

$$\begin{aligned}\frac{\mathrm{d}\Sigma^{\pm\mp}}{\mathrm{d}\Omega}(\mathbf{q}) = \frac{8\pi^3}{V}\, b_H^2\big(&|\widetilde{M}_x|^2 + |\widetilde{M}_y|^2\cos^4\theta \\ &+ |\widetilde{M}_z|^2\sin^2\theta\cos^2\theta \\ &- (\widetilde{M}_y\widetilde{M}_z^* + \widetilde{M}_y^*\widetilde{M}_z)\sin\theta\cos^3\theta\big).\end{aligned} \tag{72}$$

3.3.2. $\mathbf{k}_0 \parallel \mathbf{H}_0$.

$$\begin{aligned}\frac{\mathrm{d}\Sigma^{\pm\pm}}{\mathrm{d}\Omega}(\mathbf{q}) = \frac{8\pi^3}{V}\big(&|\widetilde{N}|^2 + b_H^2|\widetilde{M}_z|^2 \\ &\mp b_H(\widetilde{N}\widetilde{M}_z^* + \widetilde{N}^*\widetilde{M}_z)\big).\end{aligned} \tag{73}$$

$$\begin{aligned}\frac{\mathrm{d}\Sigma^{\pm\mp}}{\mathrm{d}\Omega}(\mathbf{q}) = \frac{8\pi^3}{V}\, b_H^2\big(&|\widetilde{M}_x|^2\sin^2\theta + |\widetilde{M}_y|^2\cos^2\theta \\ &- (\widetilde{M}_x\widetilde{M}_y^* + \widetilde{M}_x^*\widetilde{M}_y)\sin\theta\cos\theta\big).\end{aligned} \tag{74}$$

3.4. SANSPOL cross-sections

3.4.1. $\mathbf{k}_0 \perp \mathbf{H}_0$.

$$\begin{aligned}\frac{\mathrm{d}\Sigma^{\pm}}{\mathrm{d}\Omega}(\mathbf{q}) = \frac{8\pi^3}{V}\big(&|\widetilde{N}|^2 + b_H^2|\widetilde{M}_x|^2 + b_H^2|\widetilde{M}_y|^2\cos^2\theta \\ &+ b_H^2|\widetilde{M}_z|^2\sin^2\theta \\ &- b_H^2(\widetilde{M}_y\widetilde{M}_z^* + \widetilde{M}_y^*\widetilde{M}_z)\sin\theta\cos\theta \\ &\mp b_H(\widetilde{N}\widetilde{M}_z^* + \widetilde{N}^*\widetilde{M}_z)\sin^2\theta \\ &\pm b_H(\widetilde{N}\widetilde{M}_y^* + \widetilde{N}^*\widetilde{M}_y)\sin\theta\cos\theta\big).\end{aligned} \tag{75}$$

3.4.2. $\mathbf{k}_0 \parallel \mathbf{H}_0$.

$$\begin{aligned}\frac{\mathrm{d}\Sigma^{\pm}}{\mathrm{d}\Omega}(\mathbf{q}) = \frac{8\pi^3}{V}\big(&|\widetilde{N}|^2 + b_H^2|\widetilde{M}_x|^2\sin^2\theta + b_H^2|\widetilde{M}_y|^2\cos^2\theta \\ &+ b_H^2|\widetilde{M}_z|^2 - (\widetilde{M}_x\widetilde{M}_y^* + \widetilde{M}_x^*\widetilde{M}_y)\sin\theta\cos\theta \\ &\mp b_H(\widetilde{N}\widetilde{M}_z^* + \widetilde{N}^*\widetilde{M}_z)\big).\end{aligned} \tag{76}$$

3.5. Unpolarized SANS cross-sections

3.5.1. $\mathbf{k}_0 \perp \mathbf{H}_0$.

$$\frac{\mathrm{d}\Sigma}{\mathrm{d}\Omega}(\mathbf{q}) = \frac{8\pi^3}{V}\left(|\widetilde{N}|^2 + b_H^2|\widetilde{M}_x|^2 + b_H^2|\widetilde{M}_y|^2\cos^2\theta + b_H^2|\widetilde{M}_z|^2\sin^2\theta - b_H^2(\widetilde{M}_y\widetilde{M}_z^* + \widetilde{M}_y^*\widetilde{M}_z)\sin\theta\cos\theta\right). \quad (77)$$

3.5.2. $\mathbf{k}_0 \parallel \mathbf{H}_0$.

$$\frac{\mathrm{d}\Sigma}{\mathrm{d}\Omega}(\mathbf{q}) = \frac{8\pi^3}{V}\left(|\widetilde{N}|^2 + b_H^2|\widetilde{M}_x|^2\sin^2\theta + b_H^2|\widetilde{M}_y|^2\cos^2\theta + b_H^2|\widetilde{M}_z|^2 - b_H^2(\widetilde{M}_x\widetilde{M}_y^* + \widetilde{M}_x^*\widetilde{M}_y)\sin\theta\cos\theta\right). \quad (78)$$

3.6. Magnetic SANS at saturation

The completely saturated magnetization state, $\mathbf{M}(\mathbf{r}) = [0, 0, M_z(\mathbf{r})]$, is often used as a reference, for instance, when discussing the results of SANS measurements at lower applied magnetic fields. In fact, it turns out that the analysis of the spin-misalignment scattering is best performed when the nuclear and magnetic SANS cross-section at a saturating field-also called the residual SANS cross-section-has been subtracted. Therefore, we find it useful to explicitly display in the following the SANS cross-sections for *saturated* magnetic microstructures.

3.6.1. POLARIS.

$\mathbf{k}_0 \perp \mathbf{H}_0$.

$$\frac{\mathrm{d}\Sigma^{\pm\pm}}{\mathrm{d}\Omega}(\mathbf{q}) = \frac{8\pi^3}{V}\left(|\widetilde{N}|^2 + b_H^2|\widetilde{M}_z|^2\sin^4\theta \mp b_H(\widetilde{N}\widetilde{M}_z^* + \widetilde{N}^*\widetilde{M}_z)\sin^2\theta\right). \quad (79)$$

$$\frac{\mathrm{d}\Sigma^{\pm\mp}}{\mathrm{d}\Omega}(\mathbf{q}) = \frac{8\pi^3}{V}\, b_H^2|\widetilde{M}_z|^2\sin^2\theta\cos^2\theta. \quad (80)$$

$\mathbf{k}_0 \parallel \mathbf{H}_0$.

$$\frac{\mathrm{d}\Sigma^{\pm\pm}}{\mathrm{d}\Omega}(\mathbf{q}) = \frac{8\pi^3}{V}\left(|\widetilde{N}|^2 + b_H^2|\widetilde{M}_z|^2 \mp b_H(\widetilde{N}\widetilde{M}_z^* + \widetilde{N}^*\widetilde{M}_z)\right). \quad (81)$$

$$\frac{\mathrm{d}\Sigma^{\pm\mp}}{\mathrm{d}\Omega}(\mathbf{q}) = 0. \quad (82)$$

We remind the reader that nuclear spin-incoherent SANS [18] has been ignored here.

3.6.2. SANSPOL.

$\mathbf{k}_0 \perp \mathbf{H}_0$.

$$\frac{\mathrm{d}\Sigma^{\pm}}{\mathrm{d}\Omega}(\mathbf{q}) = \frac{8\pi^3}{V}\left(|\widetilde{N}|^2 + b_H^2|\widetilde{M}_z|^2\sin^2\theta \mp b_H(\widetilde{N}\widetilde{M}_z^* + \widetilde{N}^*\widetilde{M}_z)\sin^2\theta\right). \quad (83)$$

$\mathbf{k}_0 \parallel \mathbf{H}_0$.

$$\frac{\mathrm{d}\Sigma^{\pm}}{\mathrm{d}\Omega}(\mathbf{q}) = \frac{8\pi^3}{V}\left(|\widetilde{N}|^2 + b_H^2|\widetilde{M}_z|^2 \mp b_H(\widetilde{N}\widetilde{M}_z^* + \widetilde{N}^*\widetilde{M}_z)\right). \quad (84)$$

3.6.3. Unpolarized SANS.

$\mathbf{k}_0 \perp \mathbf{H}_0$.

$$\frac{\mathrm{d}\Sigma}{\mathrm{d}\Omega}(\mathbf{q}) = \frac{8\pi^3}{V}\left(|\widetilde{N}|^2 + b_H^2|\widetilde{M}_z|^2\sin^2\theta\right). \quad (85)$$

$\mathbf{k}_0 \parallel \mathbf{H}_0$.

$$\frac{\mathrm{d}\Sigma}{\mathrm{d}\Omega}(\mathbf{q}) = \frac{8\pi^3}{V}\left(|\widetilde{N}|^2 + b_H^2|\widetilde{M}_z|^2\right). \quad (86)$$

3.6.4. Models for the nuclear and magnetic structure factors at saturation. The present article is concerned with magnetic SANS of bulk ferromagnets, e.g. single-phase elemental ferromagnets such as nanocrystalline Co and Ni [62] or multiphase nanocomposites such as two-phase NdFeB-based alloys [55, 56] or steels [77]. For the latter class of materials, the magnetic scattering contrast at saturation arises from variations of the magnitude of the magnetization at internal (e.g. particle-matrix) interfaces, whereas for idealized homogeneous single-phase magnets (with constant values of the magnetic materials parameters), coherent magnetic SANS is absent at saturation.

In experimental studies on single-phase magnets, however, the nuclear density and/or composition will generally be nonuniform (e.g. due to the presence of second-phase particles, pores, or impurities), and consequently there can be a nanoscale nonuniformity in the magnetization, even at the highest fields when all spins are aligned. The ensuing combined nuclear and magnetic residual scattering cross-section $\mathrm{d}\Sigma_{\mathrm{res}}/\mathrm{d}\Omega$ is not accounted for in our micromagnetics approach. In order to analyze the dominant spin-misalignment scattering (at lower fields), one can either subtract the measured $\mathrm{d}\Sigma_{\mathrm{res}}/\mathrm{d}\Omega$ (at saturation) from a measurement of the total $\mathrm{d}\Sigma/\mathrm{d}\Omega$ at a particular field, or (if saturation cannot be reached) assume a particular microstructural model for $\mathrm{d}\Sigma_{\mathrm{res}}/\mathrm{d}\Omega$ (see below) and include it in the expression for $\mathrm{d}\Sigma/\mathrm{d}\Omega$.

While analytical expressions for particle form factors have been derived for practically all particle shapes, there are only few closed-form results for the structure factor [13, 32, 34, 35]. Most of the structure-factor models (e.g. hard-sphere, sticky hard-sphere or screened Coulomb potential with or without polydispersity) have been derived for particles with spherical symmetry interacting through a spherically symmetric potential. We refer to the review article by Pedersen [13] for a detailed discussion of this topic. Likewise, several software packages [195, 196] are available which contain an extensive collection of particle form factors (including particle-size distributions) and structure factors.

For a saturated two-phase particle-matrix-type bulk ferromagnet, the general expressions for the pure nuclear and

magnetic SANS take on a particularly simple form [5, 148]

$$\frac{\mathrm{d}\Sigma_{\mathrm{nuc}}}{\mathrm{d}\Omega}(\mathbf{q}) = \frac{8\pi^3}{V}|\widetilde{N}(\mathbf{q})|^2 = \frac{(\Delta\rho)^2_{\mathrm{nuc}}}{V}\left|\sum_{j=1}^{N_p} V_{p,j}\, F_j(\mathbf{q})\, \exp(-\mathrm{i}\mathbf{q}\,\mathbf{r}_j)\right|^2, \quad (87)$$

$$\frac{\mathrm{d}\Sigma_{\mathrm{mag}}}{\mathrm{d}\Omega}(\mathbf{q}) = \frac{8\pi^3}{V} b_H^2 |\widetilde{M}_z(\mathbf{q})|^2 \sin^2\theta = \frac{(\Delta\rho)^2_{\mathrm{mag}}}{V}\left|\sum_{j=1}^{N_p} V_{p,j}\, F_j(\mathbf{q})\, \exp(-\mathrm{i}\mathbf{q}\,\mathbf{r}_j)\right|^2 \sin^2\theta, \quad (88)$$

where $\Delta\rho_{\mathrm{nuc}}$ and $\Delta\rho_{\mathrm{mag}}$ denote, respectively, the nuclear and magnetic scattering-length density contrast between the particle ('p') and the matrix ('m'), N_p is the number of particles in the scattering volume V, and $V_{p,j}$, F_j, and $\mathbf{r}_j$ represent, respectively, the particle volume, the form factor and the position vector of particle 'j'. In writing down equations (87) and (88), we have assumed uniform nuclear and magnetic scattering densities of the particles (so that the factors $(\Delta\rho)_{\mathrm{nuc}}$ and $(\Delta\rho)_{\mathrm{mag}}$ can be placed in front of the form-factor integral). Furthermore, equation (88) is valid for the scattering geometry where the wavevector $\mathbf{k}_0$ of the incoming neutron beam is perpendicular to $\mathbf{H}_0$ (figure 6(*a*)); in the parallel case (figure 6(*b*)), the factor $\sin^2\theta$ is replaced by unity (see below).

The magnetic contrast is related to the jump ΔM of the magnitude of the magnetization at the particle-matrix interface according to

$$(\Delta\rho)^2_{\mathrm{mag}} = b_H^2\,(\Delta M)^2 = b_H^2\left(M_s^p - M_s^m\right)^2, \quad (89)$$

where M_s^p and M_s^m denote, respectively, the saturation magnetizations of the particle and matrix phase; for $\mu_0\Delta M = 1\,\mathrm{T}$, $(\Delta\rho)_{\mathrm{mag}} \cong 2.3\times10^{14}\,\mathrm{m}^{-2}$. In the monodisperse and dilute limit, $\mathrm{d}\Sigma_{\mathrm{res}}/\mathrm{d}\Omega$ for unpolarized neutrons and for $\mathbf{k}_0 \perp \mathbf{H}_0$ can then be written as

$$\frac{\mathrm{d}\Sigma_{\mathrm{res}}}{\mathrm{d}\Omega}(\mathbf{q}) = \frac{N_p}{V} V_p^2\, |F(\mathbf{q})|^2 \left[(\Delta\rho)^2_{\mathrm{nuc}} + (\Delta\rho)^2_{\mathrm{mag}}\, \sin^2\theta\right], \quad (90)$$

whereas for $\mathbf{k}_0 \parallel \mathbf{H}_0$,

$$\frac{\mathrm{d}\Sigma_{\mathrm{res}}}{\mathrm{d}\Omega}(\mathbf{q}) = \frac{N_p}{V} V_p^2\, |F(\mathbf{q})|^2 \left[(\Delta\rho)^2_{\mathrm{nuc}} + (\Delta\rho)^2_{\mathrm{mag}}\right]. \quad (91)$$

Note also that nuclear and magnetic form factors need not to be identical. For instance, spin canting at the surface of nanoparticles (e.g. [94, 111, 197]) may result in different nuclear and magnetic structure sizes.

3.6.5. Graphical representation. Figure 8 qualitatively shows the SANS cross-sections at saturation for $\mathbf{k}_0 \perp \mathbf{H}_0$ and for different ratios of nuclear to magnetic scattering,

$$R(q) = \frac{|\widetilde{N}|^2}{b_H^2|\widetilde{M}_z|^2}, \quad (92)$$

assuming for simplicity the sphere form factor for both nuclear $\widetilde{N}$ and longitudinal magnetic $\widetilde{M}_z$ scattering amplitudes (dilute limit). For statistically isotropic microstructures, the case $\mathbf{k}_0 \parallel \mathbf{H}_0$ is of low interest, since the corresponding SANS cross-sections are all isotropic (no θ-dependence). While most of the images in figure 8 have been reported countless times in the research literature, we would like to draw the attention of the reader to the cross-shaped angular anisotropy in the non-spin-flip ++ channel depicted in figure 8(*b*). This type of anisotropy has only recently been observed in an Fe-based two-phase nanocomposite [51] (see figure 9(*a*)). Analysis of equation (79) reveals that, for this class of materials, the cross-shaped anisotropy is only observable at saturation in $\frac{\mathrm{d}\Sigma^{++}}{\mathrm{d}\Omega}$, provided that the ratio of nuclear to magnetic scattering is smaller than unity (roughly $R \sim 0.1$–0.4), as is experimentally observed (see figure 9(*b*)). The observation of the cross-shaped anisotropy represents an example where POLARIS provides information that is not accessible via conventional (unpolarized) SANS or SANSPOL techniques.

4. Spin-misalignment SANS: micromagnetic description

When the micromagnetic expressions for the Fourier coefficients $\widetilde{M}_x^2$, $\widetilde{M}_y^2$, and $-2\widetilde{M}_y\widetilde{M}_z$ and $-2\widetilde{M}_x\widetilde{M}_y$ (equations (55)–(60)) are inserted into the SANS cross-sections of sections 3.3–3.5, one can obtain closed-form expressions for $\mathrm{d}\Sigma/\mathrm{d}\Omega$. Analysis of magnetic-field-dependent SANS data then provides *quantitative* information on the magnetic interactions, i.e. the value of the exchange-stiffness constant and the strength and spatial structure of the magnetic anisotropy field and magnetostatic field (due to ΔM fluctuations). As discussed in section 3.6.4, in the analysis procedure, it proves to be advantageous to separate the nuclear and magnetic residual SANS cross-section $\mathrm{d}\Sigma_{\mathrm{res}}/\mathrm{d}\Omega$, which is measured at complete magnetic saturation (infinite field), from the respective spin-misalignment SANS.

In this section, we provide closed-form expressions for the spin-misalignment SANS for unpolarized neutrons (section 4.2) and for the spin-flip cross-section (section 4.3). The data-analysis procedure is explained and experimental results on hard and soft magnetic nanocomposites are discussed. It turns out that the ratio of anisotropy-field strength H_p to magnetization jump ΔM at internal interfaces is the decisive parameter determining, e.g. the angular anisotropy of the cross-section and the asymptotic power-law exponent. However, we start our discussion by commenting on the relevance of SANSPOL for the study of spin-misalignment scattering.

4.1. Comment on the relevance of SANSPOL for the study of spin-misalignment scattering

We have argued in the introduction that-for bulk ferromagnets-the spin-misalignment SANS cross-section $\mathrm{d}\Sigma_M/\mathrm{d}\Omega$ represents the dominant contribution to the total unpolarized SANS cross-section, at least for applied fields not too close to saturation. In particular, there exist numerous experimental SANS data (e.g. [26]) which exhibit an extremely large field dependence. For instance, the SANS signal of nanocrystalline Co

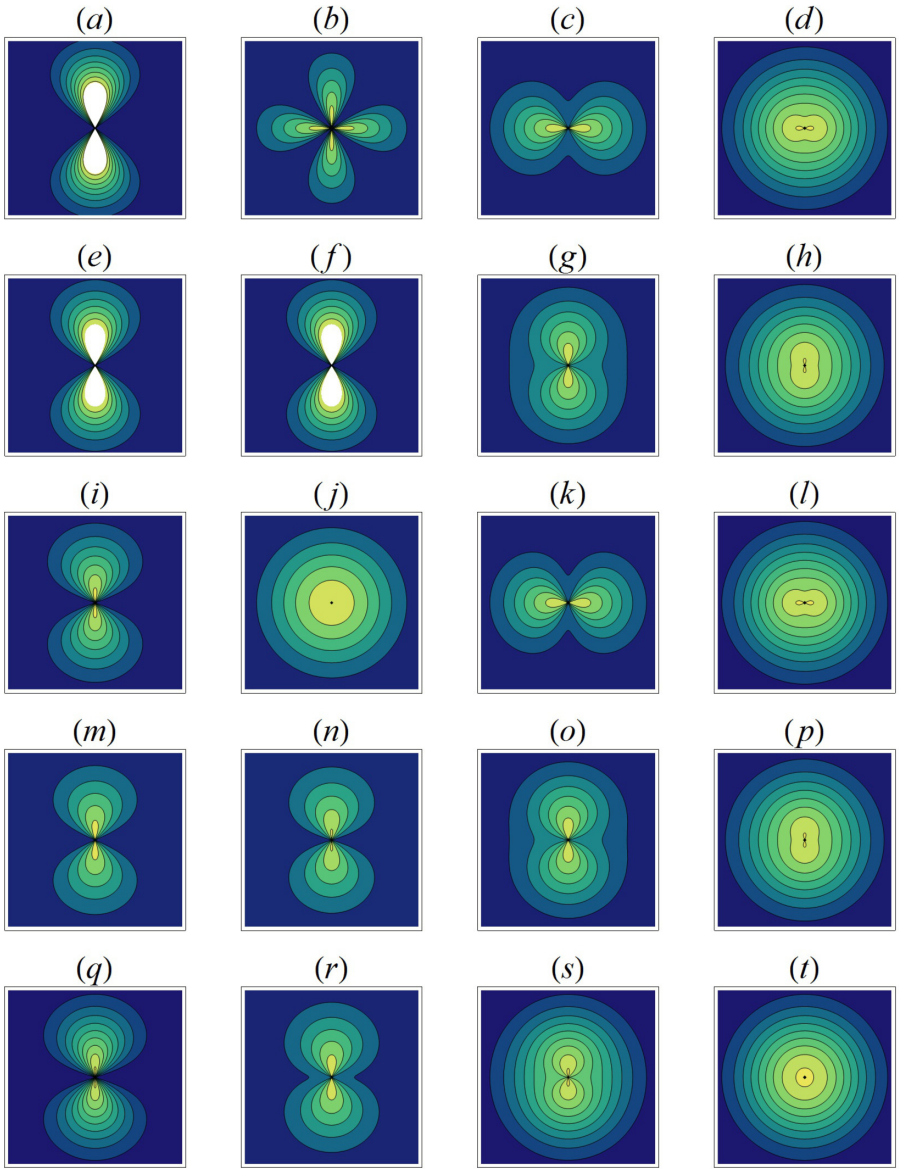

Figure 8. Qualitative variation of the SANS cross-sections at magnetic saturation for $\mathbf{k}_0 \perp \mathbf{H}_0$ and for different ratios R of nuclear to magnetic scattering ($R = |\widetilde{N}|^2/(b_H^2|\widetilde{M}_z|^2)$). (From left to right column) $R = 0.01$, $R = 0.25$, $R = 3$, $R = 400$. (a)–(d) $\frac{\mathrm{d}\Sigma^{++}}{\mathrm{d}\Omega}$; (e)–(h) $\frac{\mathrm{d}\Sigma^{--}}{\mathrm{d}\Omega}$; (i)–(l) $\frac{\mathrm{d}\Sigma^{+}}{\mathrm{d}\Omega}$; (m)–(p) $\frac{\mathrm{d}\Sigma^{-}}{\mathrm{d}\Omega}$; (q)–(t) unpolarized $\frac{\mathrm{d}\Sigma}{\mathrm{d}\Omega}$. For the calculation of the cross-sections, we have assumed the sphere form factor (sphere diameter: 16 nm) for both $|\widetilde{N}|^2$ and $|\widetilde{M}_z|^2$; the prefactor $8\pi^3/V$ in the corresponding expressions was set to unity. Yellow-green colour corresponds to 'high intensity' and blue colour to 'low intensity'.

(at the smallest q) can vary by up to three orders of magnitude between zero field (or coercivity) and a large field close to saturation (compare figure 3(a)). Since $\mathrm{d}\Sigma_M/\mathrm{d}\Omega$ is related to terms $|\widetilde{M}_x|^2$, $|\widetilde{M}_y|^2$, and to cross terms such as $\widetilde{M}_y\widetilde{M}_z$ or $\widetilde{M}_x\widetilde{M}_y$ and, since these contributions are *independent* of the polarization of the incident neutron beam, it appears to be rather straightforward to conclude that the measurement of the SANSPOL 'spin-up' and 'spin-down' cross-sections does not provide significantly more information regarding $\mathrm{d}\Sigma_M/\mathrm{d}\Omega$ than can already be learned by the measurement of the unpolarized cross-section alone. This circumstance is illustrated in the following.

The two SANSPOL cross-sections $\mathrm{d}\Sigma^+/\mathrm{d}\Omega$ and $\mathrm{d}\Sigma^-/\mathrm{d}\Omega$ contain terms which depend on the polarization of the incident neutron beam (compare section 3.4). In particular, the difference between data taken with the neutron-spin flipper on and off, $\Delta(\mathrm{d}\Sigma/\mathrm{d}\Omega) = \mathrm{d}\Sigma^-/\mathrm{d}\Omega - \mathrm{d}\Sigma^+/\mathrm{d}\Omega$, depends (for $\mathbf{k}_0 \perp \mathbf{H}_0$) on terms $\widetilde{N}\widetilde{M}_z \sin^2\theta$ and $\widetilde{N}\widetilde{M}_y \sin\theta\cos\theta$; we remind that polarization-dependent chiral terms are ignored here (compare figure 7).

Figure 10 shows the results of magnetic-field-dependent SANSPOL measurements on a NdFeB-based nanocomposite; figure 10(a) depicts the 'spin-up' and 'spin-down' cross-sections at selected field values, while figure 10(b) shows the corresponding difference $\Delta(\mathrm{d}\Sigma/\mathrm{d}\Omega)$ of the SANS cross-sections between the two spin states. It is seen that the $\mathrm{d}\Sigma^{\pm}/\mathrm{d}\Omega$ (at a given field) are practically independent of the incoming polarization. A small difference can be detected at the

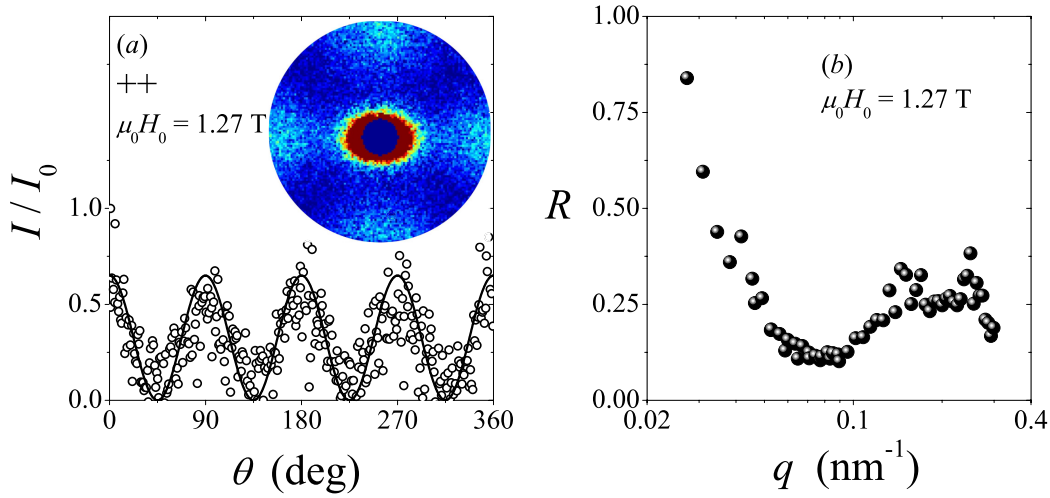

Figure 9. (*a*) (○) Normalized non-spin-flip (++) SANS intensity I/I_0 as a function of the angle θ at $\mu_0 H_0 = 1.27$ T and at $q = (0.26 \pm 0.01)$ nm^{-1} ($\mathbf{k}_0 \perp \mathbf{H}_0$). Solid line: $I/I_0 \propto \cos^2(2\theta)$. The inset shows $\frac{d\Sigma^{++}}{d\Omega}$ on the two-dimensional detector (logarithmic colour scale). Applied-field direction is horizontal. The sample under study was a magnetic nanocomposite from the NANOPERM family of alloys with a nominal composition of $(Fe_{0.985}Co_{0.015})_{90}Zr_7B_3$ [198]. (*b*) (●) Experimental momentum-transfer dependence (at 1.27 T) of the ratio R of nuclear to magnetic SANS, $R = \frac{d\Sigma_{nuc}}{d\Omega} / \frac{d\Sigma_{mag}}{d\Omega}$ (log-linear scale). Reprinted with permission from [51]. Copyright 2012 by the American Physical Society.

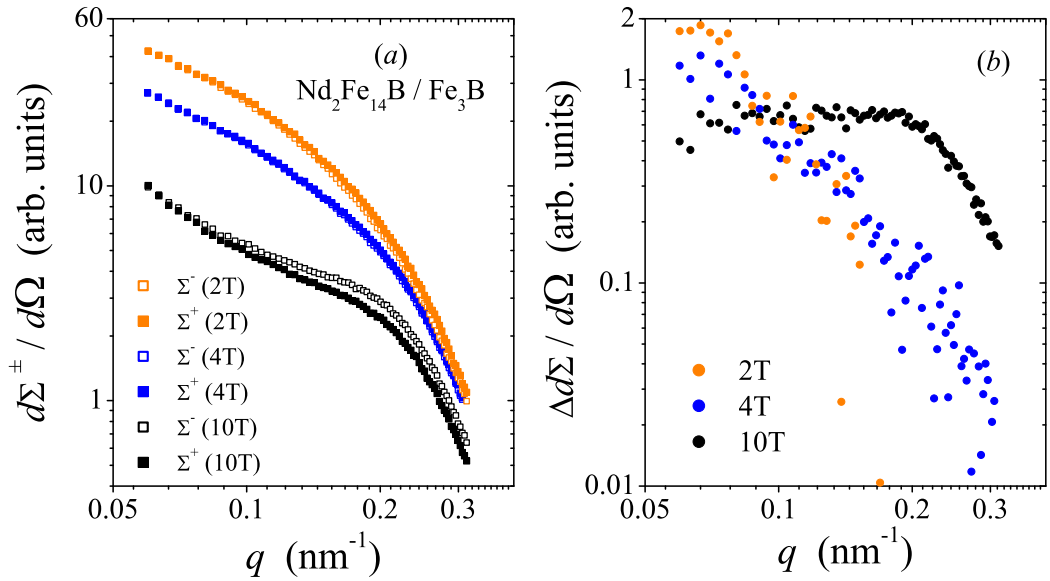

Figure 10. (*a*) SANSPOL cross-sections $d\Sigma^+/d\Omega$ (closed symbols) and $d\Sigma^-/d\Omega$ (open symbols) of a NdFeB-based nanocomposite as a function of momentum transfer q at selected applied magnetic fields (see inset) ($\mathbf{k}_0 \perp \mathbf{H}_0$) (log–log scale). (*b*) Corresponding difference cross-sections $\Delta(d\Sigma/d\Omega) = d\Sigma^-/d\Omega - d\Sigma^+/d\Omega$ (log–log scale).

largest applied field of 10 T, where the spin-misalignment scattering is weak. Given that the total unpolarized $d\Sigma/d\Omega$ (and $d\Sigma_M/d\Omega$) of this sample varies strongly as a function of the external field (compare figure 32), the observation in figure 10(*b*) that $\Delta(d\Sigma/d\Omega)$ is essentially field-independent suggests that in bulk ferromagnets the interference between nuclear and transverse spin-misalignment scattering amplitudes $\widetilde{N}\widetilde{M}_y \sin\theta\cos\theta$ is negligible. The very weak polarization dependence of $d\Sigma^{\pm}/d\Omega$ can therefore be attributed to terms $\widetilde{N}\widetilde{M}_z \sin^2\theta$.

As a further example, figure 11 depicts (for a two-phase Fe-based nanocomposite) the difference between data taken with the neutron-spin flipper on and off at several applied magnetic fields [46]. The angular anisotropy of the scattering pattern (figure 11(*a*)) is (for all fields) clearly of the $\sin^2\theta$-type, and the corresponding azimuthally-averaged data (figure 11(*b*)) are small in magnitude compared to the unpolarized data (see figure 4 in [46]) and only very weakly dependent on the applied field, in agreement with the previous conclusions. Similar results were also obtained on nanocrystalline Co [62].

These observations strongly suggest that for the study of spin-misalignment scattering it is already sufficient to measure the field dependence of the unpolarized SANS cross-section.

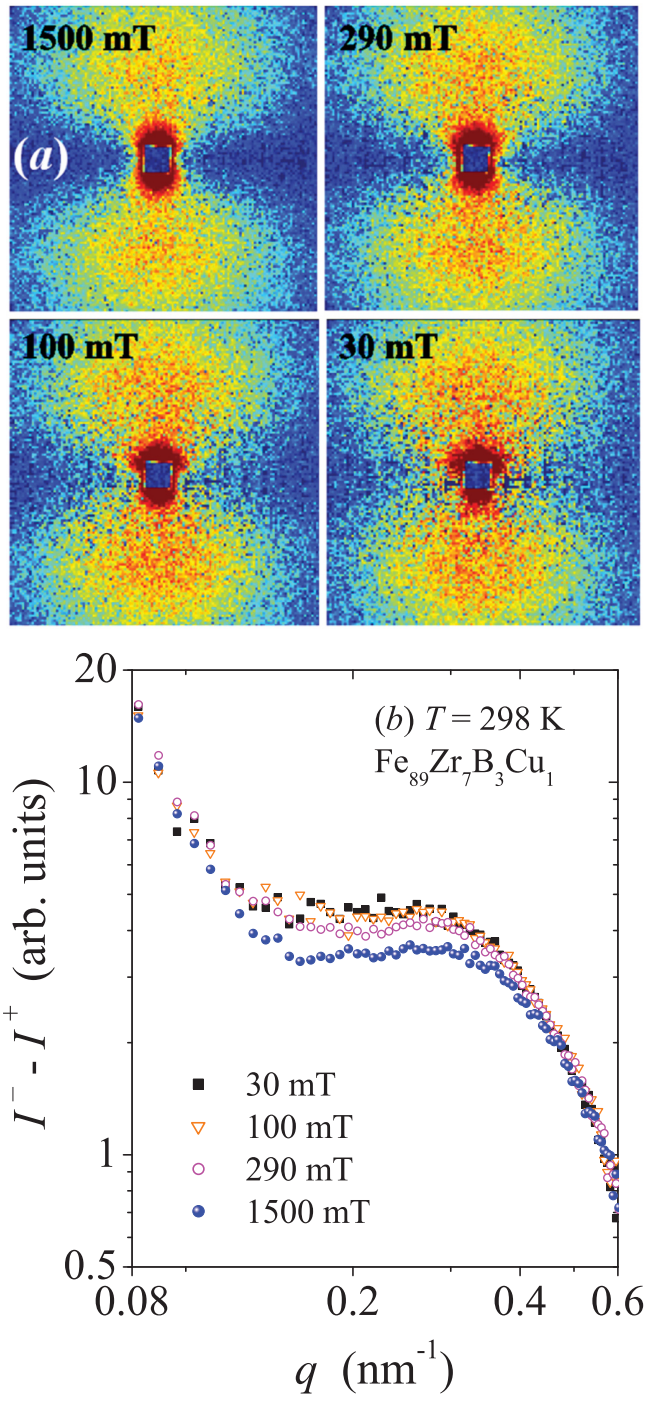

Figure 11. (*a*) Difference between flipper on and flipper off SANS intensities of NANO-PERM ($Fe_{89}Zr_7B_3Cu_1$) as a function of the applied magnetic field (see insets) ($\mathbf{k}_0 \perp \mathbf{H}_0$) (logarithmic colour scale). $\mathbf{H}_0$ is horizontal. Pixels in the corners of the detector have momentum transfer $q \cong 0.64\,\mathrm{nm}^{-1}$. (*b*) Corresponding azimuthally-averaged difference between flipper on and flipper off data (log–log scale). Reprinted with permission from [46]. Copyright 2006 by the American Physical Society.

Similar statements refer to the POLARIS non-spin-flip cross-sections $\mathrm{d}\Sigma^{++}/\mathrm{d}\Omega$ and $\mathrm{d}\Sigma^{--}/\mathrm{d}\Omega$ for the transverse scattering geometry (equations (71)) (Note that for $\mathbf{k}_0 \parallel \mathbf{H}_0$, $\mathrm{d}\Sigma^{++}/\mathrm{d}\Omega$ and $\mathrm{d}\Sigma^{--}/\mathrm{d}\Omega$ are independent of the transversal Fourier coefficients (equations (73))). Therefore, in order to provide a micromagnetic description of magnetic SANS of bulk ferromagnets, we restrict our considerations in the subsequent sections to the unpolarized and the spin-flip cross-sections.

4.2. Unpolarized case

4.2.1. $\mathbf{k}_0 \perp \mathbf{H}_0$. The unpolarized elastic SANS cross-section $\mathrm{d}\Sigma/\mathrm{d}\Omega$ for $\mathbf{k}_0 \perp \mathbf{H}_0$ (equation (77)) can be written as [53, 54]

$$\frac{\mathrm{d}\Sigma}{\mathrm{d}\Omega}(\mathbf{q}) = \frac{\mathrm{d}\Sigma_{\mathrm{res}}}{\mathrm{d}\Omega}(\mathbf{q}) + \frac{\mathrm{d}\Sigma_M}{\mathrm{d}\Omega}(\mathbf{q}), \tag{93}$$

where (compare equations (85) and (87)–(91))

$$\frac{\mathrm{d}\Sigma_{\mathrm{res}}}{\mathrm{d}\Omega}(\mathbf{q}) = \frac{8\pi^3}{V}\left(|\widetilde{N}|^2 + b_H^2|\widetilde{M}_z|^2\sin^2\theta\right) \tag{94}$$

and

$$\begin{aligned}\frac{\mathrm{d}\Sigma_M}{\mathrm{d}\Omega}(\mathbf{q}) &= \frac{8\pi^3}{V}\,b_H^2\left(|\widetilde{M}_x|^2 + |\widetilde{M}_y|^2\cos^2\theta\right.\\ &\quad\left.-(\widetilde{M}_y\widetilde{M}_z^* + \widetilde{M}_y^*\widetilde{M}_z)\sin\theta\cos\theta\right)\\ &= S_H(\mathbf{q})\,R_H(q,\theta,H_i) + S_M(\mathbf{q})\,R_M(q,\theta,H_i)\end{aligned} \tag{95}$$

is the purely magnetic SANS cross-section due to transversal spin-misalignment, with related Fourier amplitudes $\widetilde{M}_x(\mathbf{q})$ and $\widetilde{M}_y(\mathbf{q})$; equation (95) follows by inserting equations (55)–(57). $\mathrm{d}\Sigma_M/\mathrm{d}\Omega$ decomposes into a contribution $S_H\,R_H$ due to perturbing magnetic anisotropy fields and a part $S_M\,R_M$ related to magnetostatic fields. We remind the reader that the micromagnetic SANS theory considers a uniform exchange interaction and a random distribution of magnetic easy axes, but explicitly takes into account variations of the magnitude of the magnetization.

The anisotropy-field scattering function

$$S_H(\mathbf{q}) = \frac{8\pi^3}{V}\,b_H^2\,|h(\mathbf{q})|^2 \tag{96}$$

depends on the Fourier coefficient $h(\mathbf{q})$ of the magnetic anisotropy field, whereas the scattering function of the longitudinal magnetization

$$S_M(\mathbf{q}) = \frac{8\pi^3}{V}\,b_H^2\,|\widetilde{M}_z(\mathbf{q})|^2 \tag{97}$$

provides information on the magnitude $\Delta M \propto \widetilde{M}_z$ of the magnetization jump at internal (particle-matrix) interfaces. As we will see below (figure 18), both functions S_H and S_M (in units of $\mathrm{cm}^{-1}\,\mathrm{sr}^{-1}$) can be determined model-independently from the analysis of magnetic-field-dependent SANS data. Likewise, one may also employ a particle-matrix-type model based on equation (87) for both S_H and S_M; note, however, that the characteristic structural sizes that are contained in $|h(\mathbf{q})|^2$ and $|\widetilde{M}_z(\mathbf{q})|^2$ need not to be identical.

The corresponding (dimensionless) micromagnetic response functions

$$R_H(q,\theta,H_i) = \frac{p^2}{2}\left(1 + \frac{\cos^2\theta}{\left(1 + p\sin^2\theta\right)^2}\right) \tag{98}$$

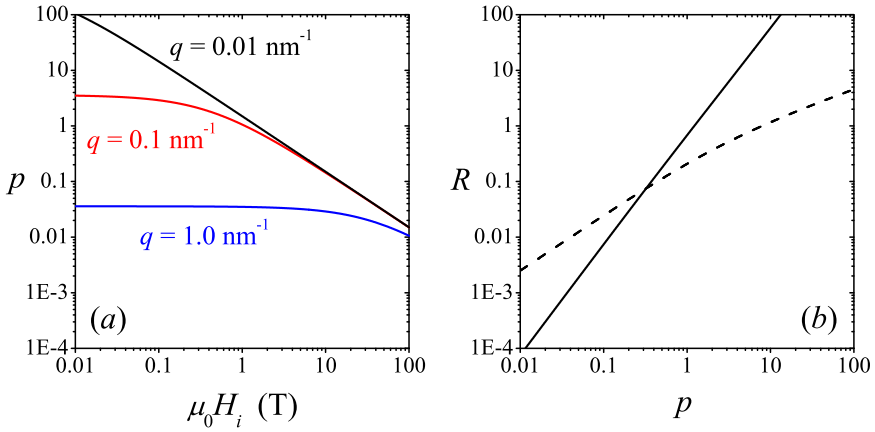

Figure 12. (*a*) Field dependence of the function $p(q, H_i) = M_s/[H_i + (2A/M_s)q^2]$ at selected values of q (see insets) (log–log scale). Materials parameters: $A = 2.5 \times 10^{-11}$ J m^{-1}; $\mu_0 M_s = 1.5$ T. (*b*) Micromagnetic response functions R_H (equation (101); solid line) and R_M (equation (102); dashed line) versus $p(q, H_i) = M_s/H_{\rm eff}(q, H_i)$ (log–log scale). Reprinted with permission from [53]. Copyright 2013 by the American Physical Society.

and

$$R_M(q, \theta, H_i) = \frac{p^2 \sin^2\theta \cos^4\theta}{\left(1 + p\sin^2\theta\right)^2} + \frac{2p\sin^2\theta\cos^2\theta}{1 + p\sin^2\theta}, \quad (99)$$

depend explicitly on the magnitude q and orientation θ of the scattering vector (compare figure 6(*a*)), on the applied magnetic field H_0, and on the magnetic materials parameters; $p(q, H_i) = M_s/H_{\rm eff}$ (compare equation (54) and see figure 12(*a*)), where the effective magnetic field $H_{\rm eff}(q, H_i) = H_i\left(1 + l_H^2 q^2\right)$ depends on the internal magnetic field $H_i = H_0 - NM_s$ and on the exchange length $l_H(H_i) = \sqrt{2A/(\mu_0 M_s H_i)}$ (compare section 2.2) (M_s: saturation magnetization; N: demagnetizing factor; A: exchange-stiffness parameter; $\mu_0 = 4\pi 10^{-7}$ Tm/A). Inspection of equations (98) and (99) shows that, depending on the values of q and H_i, a variety of angular anisotropies may be seen on a two-dimensional position-sensitive detector (see figures 13 and 14 below; compare also figure 11 in [31]).

When the functions $\widetilde{N}$, $\widetilde{M}_z$, and h depend only on the magnitude q of the scattering vector, one can perform an azimuthal average,

$$\frac{1}{2\pi}\int_0^{2\pi} (\ldots)\, {\rm d}\theta, \quad (100)$$

of equation (95). The assumption that $\widetilde{M}_z$ is isotropic is supported by experiment [48] and by micromagnetic simulations [50]. The Fourier coefficient h describes the spatial distribution (and magnitude) of magnetic anisotropy fields in the sample, and we believe that the assumption of isotropy is justified for polycrystalline (non-textured) magnetic materials. Assuming that $\widetilde{N}$, $\widetilde{M}_z$, and h are isotropic, the resulting expressions for the response functions then read [53, 54]

$$R_H(q, H_i) = \frac{p^2}{4}\left(2 + \frac{1}{\sqrt{1+p}}\right) \quad (101)$$

and

$$R_M(q, H_i) = \frac{\sqrt{1+p} - 1}{2}, \quad (102)$$

with the consequence that the azimuthally-averaged total nuclear and magnetic SANS cross-section can be written as

$$\frac{{\rm d}\Sigma}{{\rm d}\Omega}(q, H_i) = \frac{{\rm d}\Sigma_{\rm res}}{{\rm d}\Omega}(q) + S_H(q)\, R_H(q, H_i) + S_M(q)\, R_M(q, H_i). \quad (103)$$

Equation (103) is the central result.

In figure 12(*b*), both response functions R_H (equation (101)) and R_M (equation (102)) are plotted as a function of the dimensionless parameter p. Assuming that the functions S_H and S_M are of comparable magnitude, it is seen that at large applied fields or large momentum transfers (when $p \ll 1$, see figure 12(*a*)), ${\rm d}\Sigma_M/{\rm d}\Omega = S_H R_H + S_M R_M$ is dominated by the magnetostatic term $S_M R_M$, whereas at small fields and small momentum transfers (when $p \gg 1$), ${\rm d}\Sigma_M/{\rm d}\Omega$ is governed by the anisotropy-field contribution $S_H R_H$.

In order to illustrate the 'zoo' of angular anisotropies that can be obtained, figure 13 qualitatively displays the applied-field dependence of ${\rm d}\Sigma_M/{\rm d}\Omega$ for $\mathbf{k}_0 \perp \mathbf{H}_0$ (equation (95)) and for $S_H = S_M$ ($H_p/\Delta M = 1$), whereas figure 14 shows the angular anisotropy of the detector pattern as a function of the ratio $H_p/\Delta M$ at a fixed internal magnetic field. Additionally, we have included in figure 13 (lower row) the spin-misalignment SANS of a single-phase ferromagnet with a uniform saturation magnetization (i.e. $\Delta M = 0$); for such a material, perturbations in the spin-microstructure are exclusively due to spatially nonuniform magnetic anisotropy fields, and, consequently, ${\rm d}\Sigma_M/{\rm d}\Omega = S_H R_H$ [62, 199]. For the graphical representation of ${\rm d}\Sigma_M/{\rm d}\Omega$, we have for simplicity assumed that both $S_H \propto h^2(qR)$ and $S_M \propto \widetilde{M}_z^2(qR)$ can be represented by the form factor of the sphere (with radius R). Explicitly,

$$h^2(qR) = \frac{H_p^2}{(8\pi)^3}\, 9\, V_p^2\, \frac{J_1^2(qR)}{(qR)^2} \quad (104)$$

and

$$\widetilde{M}_z^2(qR) = \frac{(\Delta M)^2}{(8\pi)^3}\, 9\, V_p^2\, \frac{J_1^2(qR)}{(qR)^2}, \quad (105)$$

where $V_p = \frac{4\pi}{3}R^3$ is the particle volume and $J_1(qR)$ denotes the spherical Bessel function of first order. Under these assumptions, S_H and S_M differ only by the prefactors, i.e. the

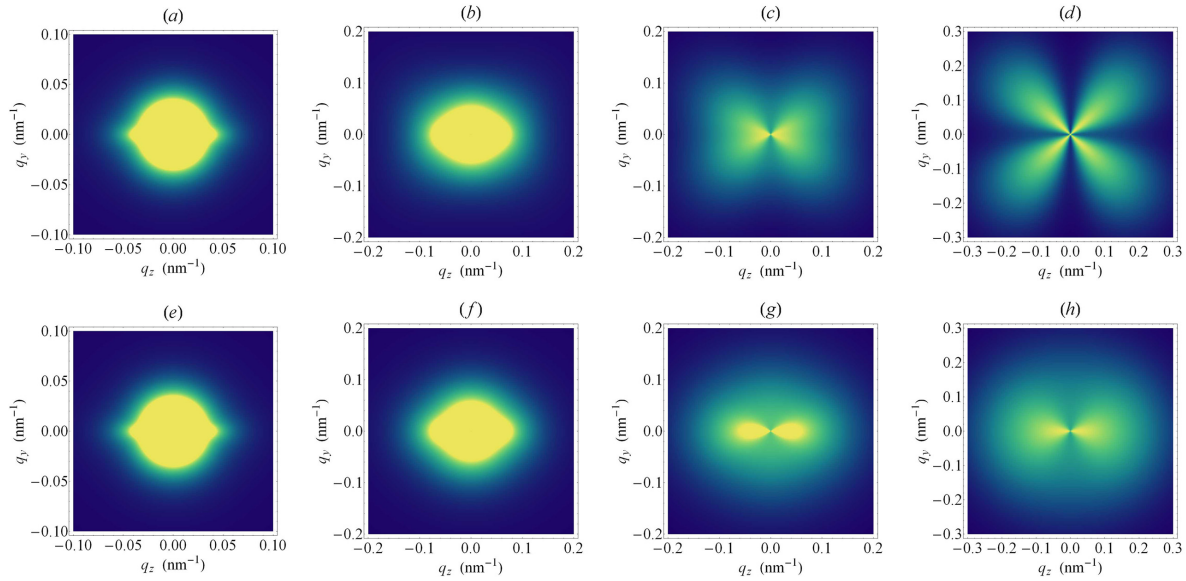

Figure 13. (Upper row) contour plots of $d\Sigma_M/d\Omega = S_H R_H + S_M R_M$ (in arbitrary units) for $\mathbf{k}_0 \perp \mathbf{H}_0$ (equation (95)). $\mathbf{H}_0$ is horizontal. For $h^2(qR)$ and $\widetilde{M}_z^2(qR)$, we used the form factor of the sphere with a radius of $R = 8$ nm (equations (104) and (105)); the prefactor $(8\pi^3/V)b_H^2$ was set to unity. Materials parameters: $A = 2.5 \times 10^{-11}$ J m^{-1}; $\mu_0 M_s = 1.5$ T; $\mu_0 H_p = 0.25$ T; $\mu_0 \Delta M = 0.25$ T ($H_p/\Delta M = 1$ and $S_H = S_M$). H_i values (in T) from (*a*) to (*d*): 0.01; 0.2; 1.0; 10.0. (Lower row) field dependence of $d\Sigma_M/d\Omega = S_H R_H$ for a homogeneous single-phase ferromagnet ($\Delta M = 0$) ($\mathbf{k}_0 \perp \mathbf{H}_0$) (equation (95) with $S_M R_M = 0$). Field values and materials parameters in (*e*) to (*h*) are the same as in (*a*) to (*d*). Yellow colour corresponds to 'high intensity' and blue colour to 'low intensity'. Reprinted with permission from [53]. Copyright 2013 by the American Physical Society.

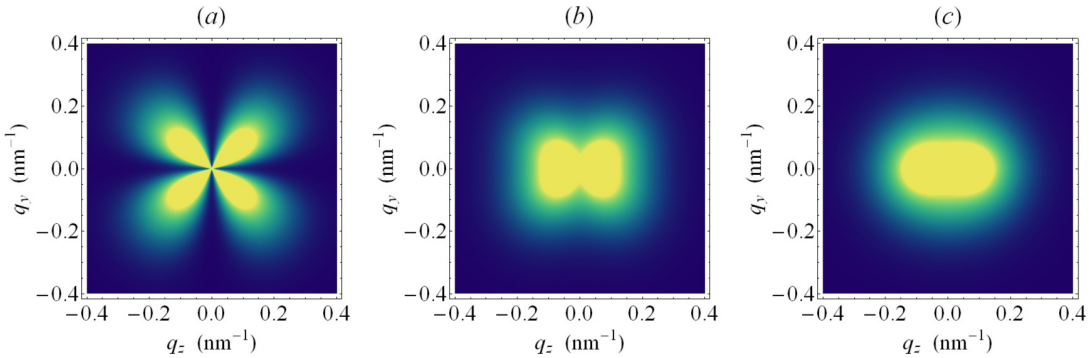

Figure 14. Crossover from magnetostatic to anisotropy-field dominated scattering. Contour plots of $d\Sigma_M/d\Omega$ (in arbitrary units) for $\mathbf{k}_0 \perp \mathbf{H}_0$ (equation (95)) at a fixed internal magnetic field of $\mu_0 H_i = 2.0$ T. $\mathbf{H}_0$ is horizontal. Form factors for $h^2(qR)$ and $\widetilde{M}_z^2(qR)$ and materials parameters are the same as in figure 13. Values of $H_p/\Delta M$ from (*a*) to (*c*): 0.2; 1.6; 8. Yellow colour corresponds to 'high intensity' and blue colour to 'low intensity'. Reprinted with permission from [53]. Copyright 2013 by the American Physical Society.

magnitude of the magnetic anisotropy field H_p and the jump ΔM of the magnitude of the magnetization at the particle-matrix interface. In fact, it is the ratio of $H_p/\Delta M$ which determines the angular anisotropy and the asymptotic power-law dependence of $d\Sigma_M/d\Omega$ as well as the characteristic decay length of spin-misalignment fluctuations (see figure 36 below) [53].

The $d\Sigma_M/d\Omega$ in figure 13 exhibit a strongly field-dependent angular anisotropy. At the largest fields and momentum transfers (figures 13(*c*) and (*d*)), the pattern exhibits maxima roughly along the diagonals of the detector-the so-called 'clover-leaf' anisotropy-previously observed in the Fe-based two-phase alloy NANOPERM (compare, e.g. figure 3 in [46]). We note that such an anisotropy type cannot be reproduced by the $d\Sigma_M/d\Omega$ for the single-phase case ($\Delta M = 0$). Here, at large q and H_i (figures 13(*g*) and (*h*)), one observes an elongation of the spin-misalignment scattering along the field direction ($\cos^2\theta$-type). The 'flying-saucer-type' sharp spike in $d\Sigma_M/d\Omega$ (figures 13(*a*) and (*e*)) is due to the magnetostatic interaction and was first predicted by Weissmüller *et al* [199]. The transition from magnetostatic ($H_p/\Delta M \ll 1$) to anisotropy-field dominated scattering ($H_p/\Delta M \gg 1$) is depicted in figure 14.

The asymptotic power-law exponent n of the *total* measured SANS cross-section, $d\Sigma/d\Omega \propto q^{-n}$, is frequently discussed in the literature. For particles with sharp interfaces, both $h^2(q)$ and $\widetilde{M}_z^2(q)$ vary asymptotically as q^{-4} [152], as does the function H_{eff}^{-2} (compare equation (39)). Taking into account that then $R_H \propto q^{-4}$ and $R_M \propto q^{-2}$, it is readily verified that the anisotropy-field contribution to $d\Sigma_M/d\Omega$ varies as $S_H R_H \propto q^{-8}$, whereas $S_M R_M \propto q^{-6}$. Therefore, depending

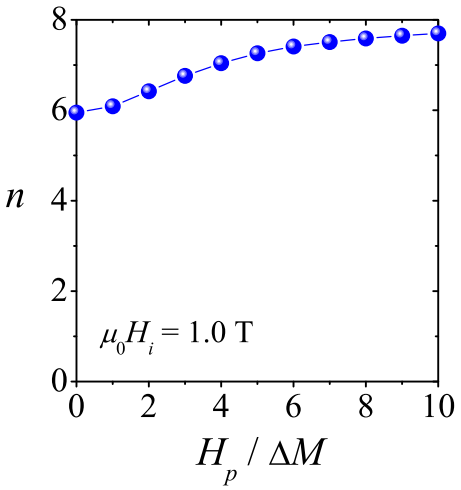

Figure 15. Variation of the power-law exponent n in $\mathrm{d}\Sigma_M/\mathrm{d}\Omega = K/q^n$ with the ratio $H_p/\Delta M$ ($\mu_0 H_i = 1.0\,\mathrm{T}$) ($\mathbf{k}_0 \perp \mathbf{H}_0$). The fits of the above power law to the simulated azimuthally-averaged data $\mathrm{d}\Sigma_M/\mathrm{d}\Omega = S_H\,R_H + S_M\,R_M$ were restricted to the interval $1.0\,\mathrm{nm}^{-1} < q < 2.0\,\mathrm{nm}^{-1}$. Form factors for $h^2(qR)$ and $\widetilde{M}_z^2(qR)$ and materials parameters are the same as in figure 13. The line is a guide to the eye. Reprinted with permission from [53]. Copyright 2013 by the American Physical Society.

on the relative magnitude of both contributions to $\mathrm{d}\Sigma_M/\mathrm{d}\Omega$, one observes different asymptotic power-law exponents of $\mathrm{d}\Sigma_M/\mathrm{d}\Omega$ and, hence, of $\mathrm{d}\Sigma/\mathrm{d}\Omega$. This is shown in figure 15, where n in $\mathrm{d}\Sigma_M/\mathrm{d}\Omega = K/q^n$ is plotted (at $\mu_0 H_i = 1.0\,\mathrm{T}$) as a function of $H_p/\Delta M$. We note that other models for the anisotropy-field microstructure may result in different exponents; in particular, the $h^2(q)$ that are related to the long-range stress fields of microstructural defects (dislocations) will give rise to asymptotic power laws that are different from the Porod exponent [200, 201].

For the case of a soft magnetic two-phase nanocomposite, figure 16 provides a *qualitative* comparison between experiment, the present analytical theory, and numerical micromagnetic simulations for the field dependence of $\mathrm{d}\Sigma_M/\mathrm{d}\Omega$ [54]. The figure demonstrates that the experimental anisotropy (θ-dependence) of $\mathrm{d}\Sigma_M/\mathrm{d}\Omega$ (upper row in figure 16) can be well reproduced by the theory (equation (95)). At the largest field of 163 mT, one observes the so-called clover-leaf-shaped angular anisotropy with maxima in $\mathrm{d}\Sigma_M/\mathrm{d}\Omega$ roughly along the diagonals of the detector. This feature is related to the magnetostatic term $S_M R_M$ in $\mathrm{d}\Sigma_M/\mathrm{d}\Omega$ (compare equation (99)). Reducing the field to 45 mT results in the emergence of a scattering pattern that is more of a $\cos^2\theta$-type, with maxima along the horizontal field direction, as described by the term $S_H R_H$ in $\mathrm{d}\Sigma_M/\mathrm{d}\Omega$ (compare equation (98)). The observed transition in the experimental data is qualitatively reproduced by the analytical micromagnetic theory (middle row) and by the results of full-scale three-dimensional micromagnetic simulations for $\mathrm{d}\Sigma_M/\mathrm{d}\Omega$ (lower row). For further details on the micromagnetic simulation methodology, we refer the reader to [31, 49, 50].

The ratio of $\mathrm{d}\Sigma_M/\mathrm{d}\Omega$ along different directions in momentum space can be easily obtained from equations (98) and (99). In particular,

$$\frac{\frac{\mathrm{d}\Sigma_M}{\mathrm{d}\Omega}(\theta = 0^\circ)}{\frac{\mathrm{d}\Sigma_M}{\mathrm{d}\Omega}(\theta = 90^\circ)} = 2. \tag{106}$$

Equation (106), which is independent of q and H_i, also holds for spin-flip scattering (compare equations (115)–(117) below). Figure 17 depicts the field dependence of the above ratio ($\pm 7.5^\circ$ sector averages) for the case of spin-flip scattering from nanocrystalline Co [67]. Note that the value of $r = 2$ is expected to be strictly valid only for $\theta = 0^\circ$ and for $\theta = 90^\circ$; sector averaging and the related additional scattering contributions may result in $r < 2$.

In experimental situations, it is often advantageous to analyze azimuthally-averaged data, instead of $\mathrm{d}\Sigma_M/\mathrm{d}\Omega$ as a function of two independent variables, e.g. q_y and q_z. In the following, we outline how azimuthally-averaged data for the *total* unpolarized $\mathrm{d}\Sigma/\mathrm{d}\Omega$ (and spin-flip SANS) can be analyzed in terms of the micromagnetic SANS theory. For given values of the materials parameters A and M_s, the numerical values of both response functions are known at each value of q and H_i. Equation (103) is linear in both R_H and R_M, with *a priori* unknown functions $\mathrm{d}\Sigma_{\mathrm{res}}/\mathrm{d}\Omega$, S_H, and S_M. By plotting at a particular $q = q^\star$ the values of $\mathrm{d}\Sigma/\mathrm{d}\Omega$ measured at several H_i versus $R_H(q^\star, H_i, A)$ and $R_M(q^\star, H_i, A)$, one can obtain the values of $\mathrm{d}\Sigma_{\mathrm{res}}/\mathrm{d}\Omega$, S_H, and S_M at $q = q^\star$ by (weighted) least-squares plane fits. In this way, one obtains the theoretical $\mathrm{d}\Sigma/\mathrm{d}\Omega = \mathrm{d}\Sigma_{\mathrm{res}}/\mathrm{d}\Omega + S_H R_H + S_M R_M$ at *discrete* q and H_i. This procedure is illustrated in figure 18 for the case of a two-phase Fe-based nanocomposite [54]. Treating the exchange-stiffness constant in the expression for H_{eff} as an adjustable parameter, allows one to obtain information on this quantity. Note that in order to obtain a best-fit value for A from experimental field-dependent SANS data, it is not necessary that the data is available in absolute units.

We would also like to particularly emphasize that the micromagnetic fitting routine does not represent a 'continuous' fit in the traditional sense, rather we compute the theoretical cross-section at discrete q and at several H_i; for comparison to experiment, these simulated data points may then be connected by straight lines (compare e.g. solid lines in figures 19, 22 and 23(a)).

The azimuthally-averaged field-dependent SANS cross-sections of two soft magnetic nanocomposites from the NANOPERM family of alloys along with the fits to the micromagnetic theory (equation (103)) are displayed in figures 19(a) and (b). It is seen that for both samples the entire (q, H_i)-dependence of $\mathrm{d}\Sigma/\mathrm{d}\Omega$ can be excellently described by the micromagnetic prediction. As expected, both residual SANS cross-sections $\mathrm{d}\Sigma_{\mathrm{res}}/\mathrm{d}\Omega$ ($\circ$) are smaller than the respective total $\mathrm{d}\Sigma/\mathrm{d}\Omega$, supporting the notion of dominant spin-misalignment scattering in these type of materials. From the fit of the entire (q, H_i) data set to equation (103) one obtains values for the volume-averaged exchange-stiffness constants (compare insets in figures 19(a) and (b)). We obtain $A = 3.1 \pm 0.1\,\mathrm{pJ\,m^{-1}}$ for the Co-free alloy and $A = 4.7 \pm 0.9\,\mathrm{pJ\,m^{-1}}$ for the zero-magnetostriction NANOPERM sample.

Since jumps in A are not taken into account in the micromagnetic SANS theory (equation (103)), the determined A

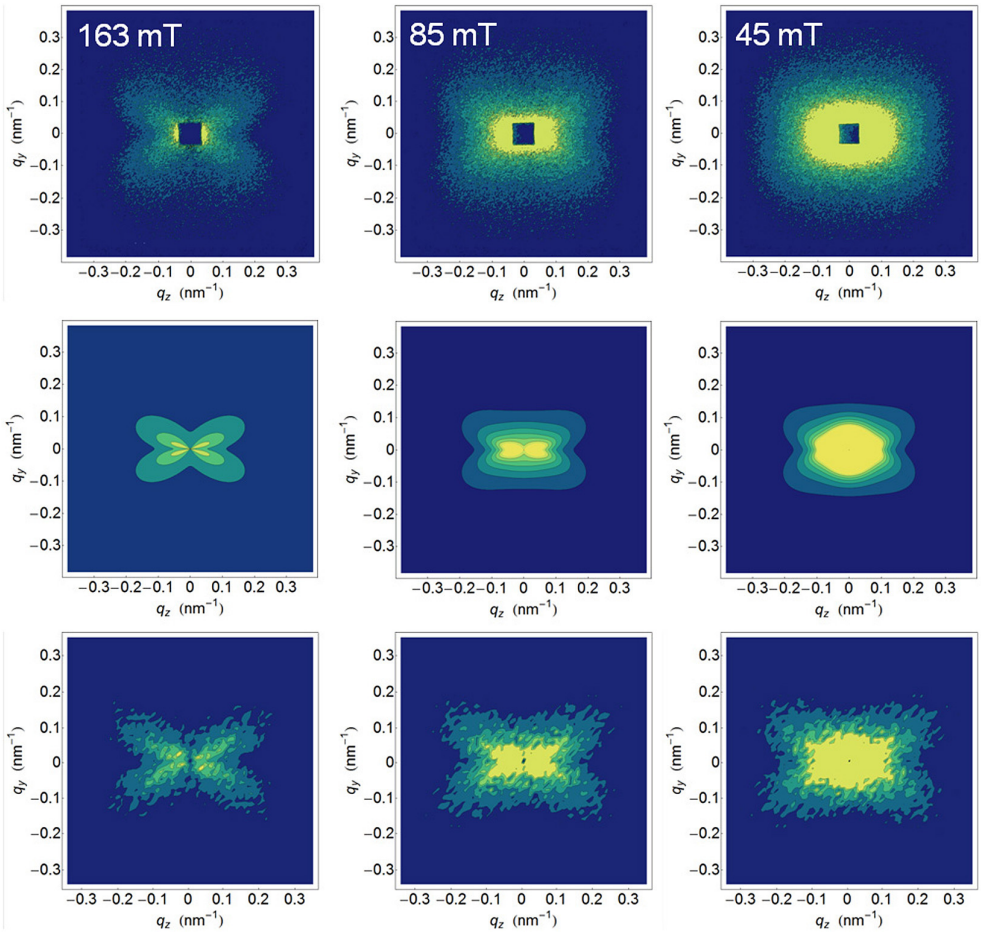

Figure 16. Qualitative comparison between experiment, analytical theory, and numerical micromagnetic simulations. Upper row: experimental spin-misalignment SANS cross-sections $d\Sigma_M/d\Omega$ of $Fe_{89}Zr_7B_3Cu$ [202] in the plane of the two-dimensional detector at selected applied magnetic fields (see insets). The $d\Sigma_M/d\Omega$ were obtained by subtracting the scattering at a saturating field of 1994 mT. $\mathbf{H}_0$ is horizontal. Middle row: prediction by the micromagnetic theory for $d\Sigma_M/d\Omega$ (equation (95)) at the same field values as above. For $h^2(qR)$ and $\widetilde{M}_z^2(qR)$, we used the form factor of the sphere with a radius of $R = 6$ nm (equations (104) and (105)). Furthermore, the following materials parameters were used: $A = 3.1$ pJ m^{-1}; $\mu_0 M_s = 1.26$ T; $\mu_0 H_p = 0.01$ T; $\mu_0 \Delta M = 0.05$ T. Lower row: results of full-scale three-dimensional micromagnetic simulations for $d\Sigma_M/d\Omega$ [31, 49, 50]. Linear colour scale is used in all figures. For each data set, we have, respectively, normalized $d\Sigma_M/d\Omega$ to its highest value at the lowest field of 45 mT. Yellow colour corresponds to 'high' $d\Sigma_M/d\Omega$ and blue colour to 'low' values of $d\Sigma_M/d\Omega$. Reprinted with permission from [54]. Copyright 2013 by the American Physical Society.

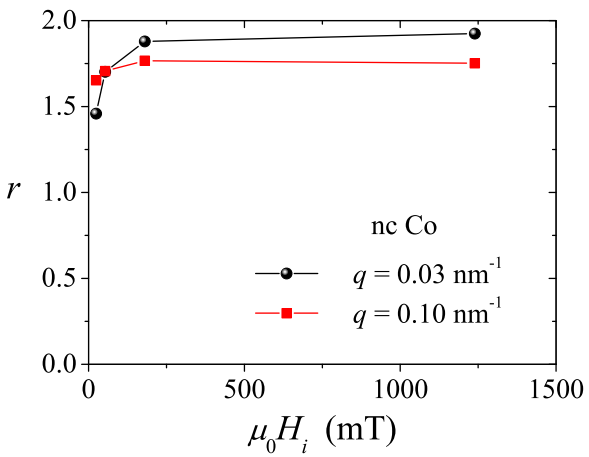

Figure 17. Field dependence of the ratio r of $d\Sigma_M^{+-}/d\Omega$ of nanocrystalline Co parallel ($\theta = 0°$) and perpendicular ($\theta = 90°$) to $\mathbf{H}_0$ at selected q-values (see inset). Lines are a guide to the eye. Reproduced with permission from [67]. Copyright 2011, Institute of Physics Publishing.

values represent mean values, averaged both over crystalline nanoparticle and amorphous matrix regions within the sample. The thickness δ of the intergranular amorphous layer between the bcc iron nanoparticles can be roughly estimated by $\delta = D(x_C^{-1/3} - 1)$ [203], where D is the average particle size and x_C denotes the crystalline volume fraction. For $Fe_{89}Zr_7B_3Cu$ with $D = 12$ nm and $x_C = 40\%$ we obtain $\delta \cong 4$ nm, whereas $\delta \cong 2$ nm for $(Fe_{0.985}Co_{0.015})_{90}Zr_7B_3$ with $D = 15$ nm and $x_C = 65\%$ [54]. Since one may expect that the effective exchange stiffness is governed by the weakest link in the bcc-amorphous-bcc coupling chain [204, 205], the above determined experimental values for A reflect qualitatively the trend in δ (and hence in x_C) between the two samples.

In addition to the exchange-stiffness constant, analysis of field-dependent SANS data in terms of equation (103) provides the magnitude squares of the Fourier coefficients of the magnetic anisotropy field $S_{H_a} \propto |h(q)|^2$ and of the longitudinal magnetization $S_M \propto |\widetilde{M}_z(q)|^2 \propto (\Delta M)^2$. The obtained results for these functions are shown in figure 20. It is

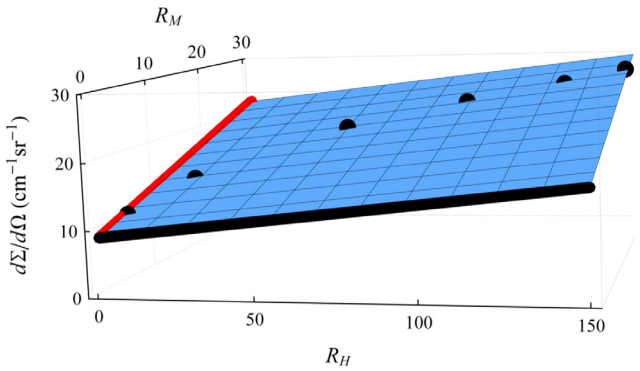

Figure 18. Illustration of the neutron-data analysis procedure according to equation (103). The sample under study is a soft magnetic two-phase nanocomposite $(Fe_{0.985}Co_{0.015})_{90}Zr_7B_3$. The total (nuclear and magnetic) unpolarized $d\Sigma/d\Omega$ (•) at a fixed $q^\star = 0.114\,nm^{-1}$ is plotted versus the response functions R_H and R_M evaluated at $A = 4.7\,pJ\,m^{-1}$ and experimental field values (in mT) of 1270, 312, 103, 61, 42, 33. The plane represents a fit to equation (103). The intercept of the plane with the $d\Sigma/d\Omega$-axis provides the residual SANS cross-section $d\Sigma_{res}/d\Omega$, while S_H and S_M are obtained from the slopes of the plane (slopes of the thick black and red lines). Reprinted with permission from [54]. Copyright 2013 by the American Physical Society.

immediately seen in figure 20 that over most of the displayed q-range $|\widetilde{M}_z|^2$ is orders of magnitude larger than $|h|^2$, suggesting that jumps ΔM in the magnetization at internal interfaces is the dominating source of spin disorder in these alloys.

Numerical integration of $S_H(q)$ and $S_M(q)$ over the whole **q**-space, i.e.

$$\frac{1}{2\pi^2 b_H^2}\int_0^\infty S_{H,M}\, q^2\, dq, \tag{107}$$

yields, respectively, the mean-square anisotropy field $\langle|\mathbf{H}_p|^2\rangle$ and the mean-square longitudinal magnetization fluctuation $\langle|M_z|^2\rangle$. These quantities are, respectively, defined as

$$\langle|\mathbf{H}_p|^2\rangle = \frac{1}{V}\int_V |\mathbf{H}_p(\mathbf{r})|^2\, dV \tag{108}$$

and

$$\langle|M_z|^2\rangle = \frac{1}{V}\int_V |M_z(\mathbf{r})|^2\, dV. \tag{109}$$

Equations (107) follow from equations (108) and (109) by using Parseval's theorem of Fourier theory and the definitions of S_H and S_M (equations (96) and (97)). However, since experimental data for S_H and S_M are only available within a finite range of momentum transfers (between q_{min} and q_{max}) and since both integrands $S_H q^2$ and $S_M q^2$ do not show signs of convergence, one can only obtain rough lower bounds for these quantities: for the $(Fe_{0.985}Co_{0.015})_{90}Zr_7B_3$ sample (for which $d\Sigma/d\Omega$ is available in absolute units), we obtain $\mu_0\langle|\mathbf{H}_p|^2\rangle^{1/2} \cong 10\,mT$ and $\mu_0\langle|M_z|^2\rangle^{1/2} \cong 50\,mT$. This finding qualitatively supports the notion of dominant spin-misalignment scattering due to magnetostatic fluctuations. Note also that in a SANS experiment only the components of the momentum-transfer vector **q** perpendicular to the incident-beam direction ($\mathbf{k}_0$) are effectively probed, which may also limit the values of the integrals in equations (107).

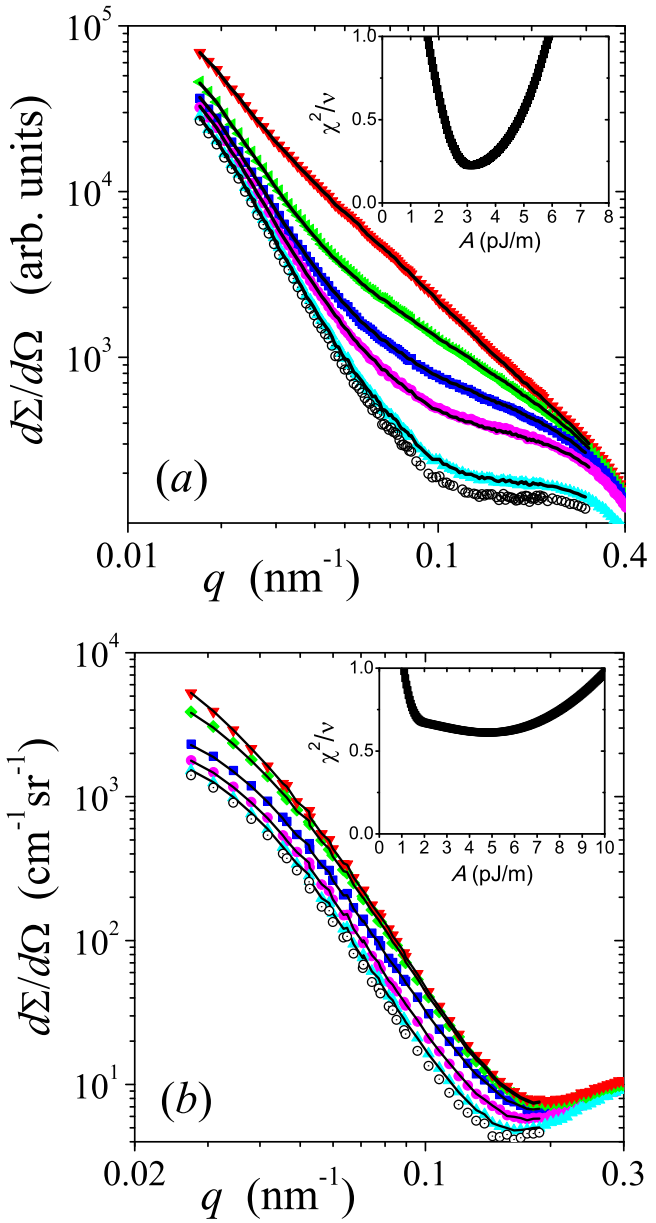

Figure 19. Azimuthally-averaged $d\Sigma/d\Omega$ of (*a*) $Fe_{89}Zr_7B_3Cu$ and (*b*) $(Fe_{0.985}Co_{0.015})_{90}Zr_7B_3$ at selected applied magnetic fields (log–log scale). Field values (in mT) from bottom to top: (*a*) 1994, 321, 163, 85, 45; (*b*) 1270, 312, 103, 61, 33. Solid lines in (*a*) and (*b*): fit to the micromagnetic theory (equation (103)); the solid lines connect the computed $d\Sigma/d\Omega$ at each value of q and H_i. (○) Residual scattering cross-sections $d\Sigma_{res}/d\Omega$. The insets depict the respective (reduced) weighted mean-square deviation between experiment and fit, χ^2/ν, as a function of the exchange-stiffness constant A. Reprinted with permission from [54]. Copyright 2013 by the American Physical Society.

Knowledge of $S_M \propto |\widetilde{M}_z|^2$ and of the residual SANS cross-section $d\Sigma_{res}/d\Omega$ (equation (94)) allows one to obtain the nuclear scattering $|\widetilde{N}|^2$ (see figure 20), without using sector-averaging procedures (in unpolarized scattering) or polarization analysis [48].

4.2.2. $\mathbf{k}_0 \parallel \mathbf{H}_0$. For $\mathbf{k}_0 \parallel \mathbf{H}_0$ (compare figure 6(*b*)), the unpolarized elastic SANS cross-section $d\Sigma/d\Omega$ (equation (78))

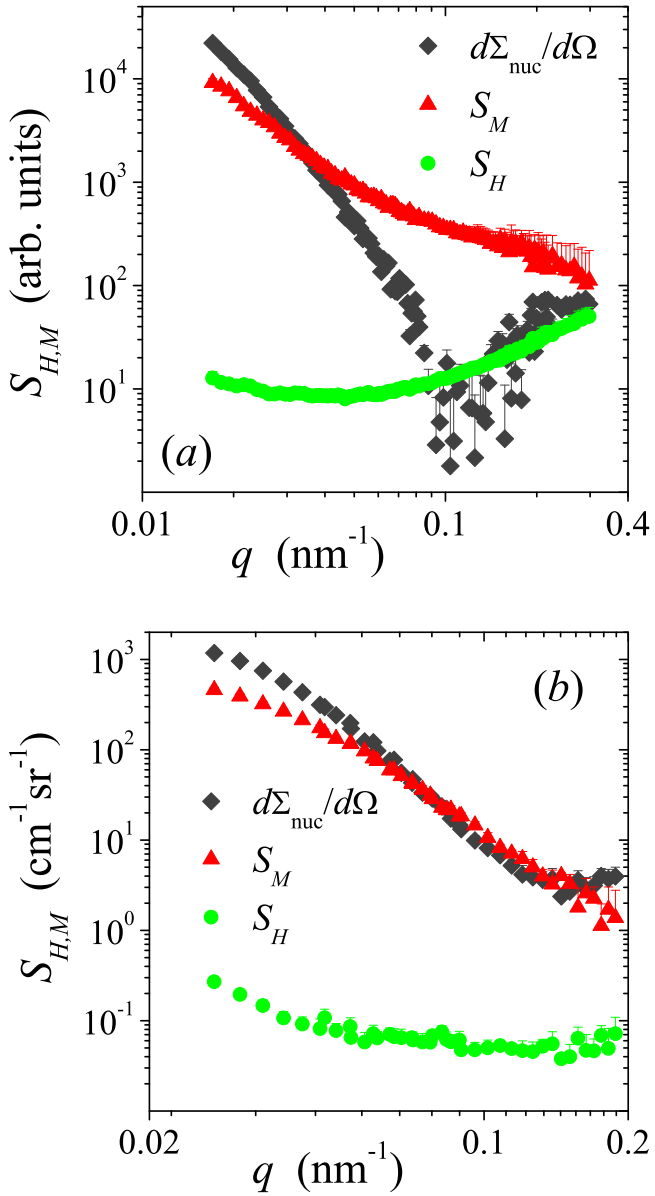

Figure 20. Best-fit results for the scattering function of the anisotropy field $S_H = (8\pi^3/V)b_H^2|h(q)|^2$ and for the scattering function of the longitudinal magnetization $S_M = (8\pi^3/V)b_H^2|\widetilde{M}_z(q)|^2$ of (*a*) $Fe_{89}Zr_7B_3Cu$ and (*b*) $(Fe_{0.985}Co_{0.015})_{90}Zr_7B_3$ (log–log scale). $d\Sigma_{nuc}/d\Omega = (8\pi^3/V)|\widetilde{N}|^2$ denotes the nuclear SANS, which was, respectively, obtained by subtracting the $|\widetilde{M}_z|^2$ scattering from the residual SANS cross-section $d\Sigma_{res}/d\Omega$ (compare equation (94)). Reprinted with permission from [54]. Copyright 2013 by the American Physical Society.

can be written as [53]

$$\frac{d\Sigma}{d\Omega}(\mathbf{q}) = \frac{d\Sigma_{res}}{d\Omega}(\mathbf{q}) + \frac{d\Sigma_M}{d\Omega}(\mathbf{q}), \tag{110}$$

where (compare equations (86)–(91))

$$\frac{d\Sigma_{res}}{d\Omega}(\mathbf{q}) = \frac{8\pi^3}{V}\left(|\widetilde{N}|^2 + b_H^2|\widetilde{M}_z|^2\right) \tag{111}$$

and

$$\frac{d\Sigma_M}{d\Omega}(\mathbf{q}) = \frac{8\pi^3}{V} b_H^2 \left(|\widetilde{M}_x|^2 \sin^2\theta + |\widetilde{M}_y|^2 \cos^2\theta - (\widetilde{M}_x\widetilde{M}_y^* + \widetilde{M}_x^*\widetilde{M}_y)\sin\theta\cos\theta\right) = S_H(\mathbf{q})\, R_H(q,\theta,H_i). \tag{112}$$

Note that in the longitudinal SANS geometry the response function

$$R_H(q,\theta,H_i) = R_H(q,H_i) = \frac{p^2}{2} \tag{113}$$

is isotropic (i.e. θ-independent) [53]; S_H is given by equation (96). Equations (112)–(113) follow by inserting equations (58)–(60). Furthermore, we note that the spin-misalignment scattering $d\Sigma_M/d\Omega$ does not depend on $\widetilde{M}_z$ fluctuations and equals the expression for the single-phase material case (compare equation (33) in [199]). In other words, the two-phase nature of the underlying microstructure is (for $\mathbf{k}_0 \parallel \mathbf{H}_0$) only contained in $d\Sigma_{res}/d\Omega$, and not in $d\Sigma_M/d\Omega$. For statistically isotropic microstructures, the total $d\Sigma/d\Omega$ is isotropic. This is illustrated in figure 21 for the case of a NdFeB-based nanocomposite. The corresponding azimuthally-averaged $d\Sigma/d\Omega$ shown in figure 22 can be excellently described by the micromagnetic theory (solid lines), which provides an average exchange-stiffness constant of $A \cong 12.5\,\mathrm{pJ\,m^{-1}}$ [56].

4.3. POLARIS case

4.3.1. $\mathbf{k}_0 \perp \mathbf{H}_0$. As in the previous sections, one may subtract the SANS signal at saturation, $d\Sigma^{+-}/d\Omega = (8\pi^3/V)b_H^2|\widetilde{M}_z|^2\sin^2\theta\cos^2\theta$, from the $d\Sigma^{+-}/d\Omega$ at lower fields in order to obtain the spin-flip scattering that is related to spin-misalignment (compare equation (72)). Inserting equations (55)–(57) into the remaining

$$\frac{d\Sigma_M^{+-}}{d\Omega}(\mathbf{q}) = \frac{8\pi^3}{V} b_H^2 \left(|\widetilde{M}_x|^2 + |\widetilde{M}_y|^2\cos^4\theta - (\widetilde{M}_y\widetilde{M}_z^* + \widetilde{M}_y^*\widetilde{M}_z)\sin\theta\cos^3\theta\right) \tag{114}$$

results in

$$\frac{d\Sigma_M^{+-}}{d\Omega}(\mathbf{q}) = S_H(\mathbf{q})\, R_H^{+-}(q,\theta,H_i) + S_M(\mathbf{q})\, R_M^{+-}(q,\theta,H_i), \tag{115}$$

where $S_H(\mathbf{q}) = (8\pi^3/V)b_H^2h^2(\mathbf{q})$ and $S_M(\mathbf{q}) = (8\pi^3/V)b_H^2\widetilde{M}_z^2(\mathbf{q})$ remain unchanged, but

$$R_H^{+-}(q,\theta,H_i) = \frac{p^2}{2}\left(1 + \frac{\cos^4\theta}{\left(1 + p\sin^2\theta\right)^2}\right) \tag{116}$$

and

$$R_M^{+-}(q,\theta,H_i) = \frac{p^2\sin^2\theta\cos^6\theta}{\left(1 + p\sin^2\theta\right)^2} + \frac{2p\sin^2\theta\cos^4\theta}{1 + p\sin^2\theta}. \tag{117}$$

The azimuthal averages of the response functions $(1/(2\pi)\int_0^{2\pi}(\ldots)d\theta)$ read

$$R_H^{+-}(q,H_i) = \frac{2 + 2p^2 - (2-p)\sqrt{1+p}}{4} \tag{118}$$

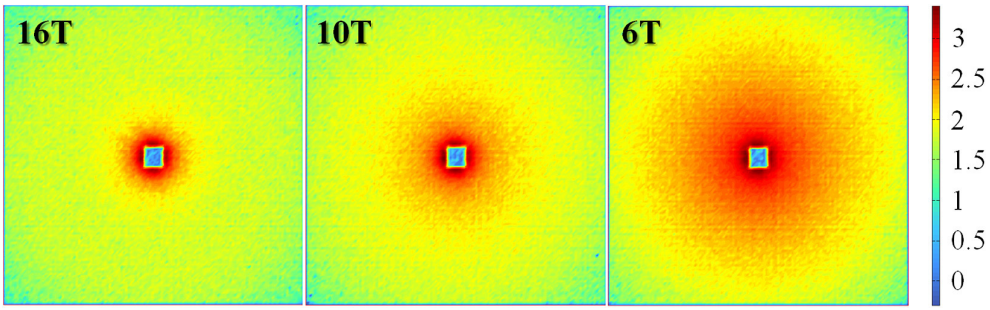

Figure 21. Experimental (unpolarized) SANS intensity distribution of a NdFeB-based nanocomposite at selected applied magnetic fields (see insets) ($\mathbf{k}_0 \parallel \mathbf{H}_0$) (logarithmic colour scale). Pixels in the corners of the detector correspond to $q \cong 0.30\,\mathrm{nm}^{-1}$.

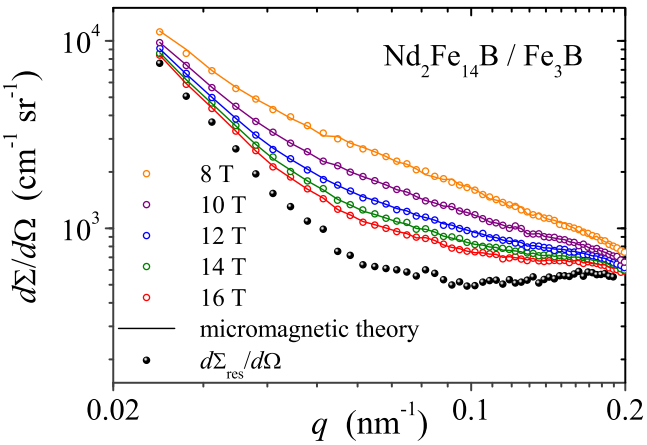

Figure 22. Azimuthally-averaged (unpolarized) $\mathrm{d}\Sigma/\mathrm{d}\Omega$ of a NdFeB-based nanocomposite as a function of momentum transfer q ($\mathbf{k}_0 \parallel \mathbf{H}_0$) (compare figure 21) (log–log scale). Values of H_0 (see inset) increase from top to bottom. The solid lines represent a fit of the experimental data to the micromagnetic theory (equations (110)–(113)); we remind that the fitting procedure yields the theoretical cross-section at discrete q and H_0 (rather than as a continuous function). (•) Nuclear and magnetic residual SANS cross-section $\mathrm{d}\Sigma_{\mathrm{res}}/\mathrm{d}\Omega$. Reproduced with permission from [56]. Copyright 2013, American Institute of Physics.

and

$$R_M^{+-}(q, H_i) = \frac{8\left(\sqrt{1+p}-1\right) - p\left(16 - 12\sqrt{1+p} + p\left[9 - 4\sqrt{1+p}\right]\right)}{8p^2}. \tag{119}$$

Figure 23 depicts the results of a micromagnetic neutron-data analysis of the field-dependent spin-flip cross-section of a nanocrystalline Co sample [67]. Global fitting of the $\mathrm{d}\Sigma^{+-}/\mathrm{d}\Omega$ data (solid lines in figure 23(a)) yields a room-temperature value of $A = (2.8 \pm 0.1) \times 10^{-11}\,\mathrm{J\,m^{-1}}$ for the volume-averaged exchange-stiffness constant (compare inset in figure 23(b)). This value agrees with literature data on single crystals obtained by means of inelastic neutron scattering [206]. The results for the anisotropy-field scattering function S_H and the longitudinal magnetization S_M (figure 23(b)) demonstrate that, as expected for a single-phase magnet, fluctuations in the magnetic anisotropy field represent the dominating source of spin disorder and dominate in strength over ΔM fluctuations.

Another nice 'feature' of the POLARIS technique is that both magnetization Fourier coefficients $|\widetilde{M}_x|^2$ and $|\widetilde{M}_y|^2$ can be obtained by means of appropriate averaging along certain directions in momentum space [48, 91]. In particular, sector averages of the two-dimensional spin-flip cross-section along the vertical ($\theta = 90°$) and the horizontal ($\theta = 0°$) direction yield, respectively, $|\widetilde{M}_x|^2$ and $|\widetilde{M}_x|^2 + |\widetilde{M}_y|^2$ along the respective directions (compare equation (72)). In figure 24, we show (for an FeCr-based nanocomposite) both correlation functions at different applied magnetic fields [48]. Roughly, the $|\widetilde{M}_x|^2 + |\widetilde{M}_y|^2$ data appear to be twice as large as $|\widetilde{M}_x|^2$. The longitudinal Fourier component $|\widetilde{M}_z|^2$ may be obtained from a measurement of $\mathrm{d}\Sigma^{+-}/\mathrm{d}\Omega$ at saturation (compare figure 7).

4.3.2. $\mathbf{k}_0 \parallel \mathbf{H}_0$. Since $\frac{\mathrm{d}\Sigma^{+-}}{\mathrm{d}\Omega}$ for the longitudinal scattering geometry (equation (74)) is identical to the corresponding spin-misalignment SANS cross-section $\mathrm{d}\Sigma_M/\mathrm{d}\Omega$ for unpolarized neutrons (compare equations (78) and (86)), it follows that $\frac{\mathrm{d}\Sigma^{+-}}{\mathrm{d}\Omega}$ for $\mathbf{k}_0 \parallel \mathbf{H}_0$ is described by equations (112) and (113).

5. Real-space analysis of magnetic SANS data: autocorrelation function of the spin-misalignment

As discussed in the preceding sections, by means of the continuum theory of micromagnetics it becomes possible to calculate the spin-misalignment SANS cross-section of bulk ferromagnets as a function of momentum transfer, applied magnetic field, as well as of magnetic and microstructural parameters (e.g. particle size). In addition to analyzing field-dependent SANS data directly in reciprocal space, one may also Fourier transform the data and carry out a study in real space. This approach provides not only complementary information about characteristic magnetic length scales, but it is essentially model independent. In particular, the real-space approach does not rely on the assumption of small misalignment of magnetic moments relative to the applied-field direction. It may therefore be applied to hard magnetic materials, which cannot be brought into the approach-to-saturation regime with available laboratory magnetic fields.

In section 5.1, we define the autocorrelation of the spin-misalignment, and in section 5.2 we discuss the impact of various models for the anisotropy-field microstructure on the

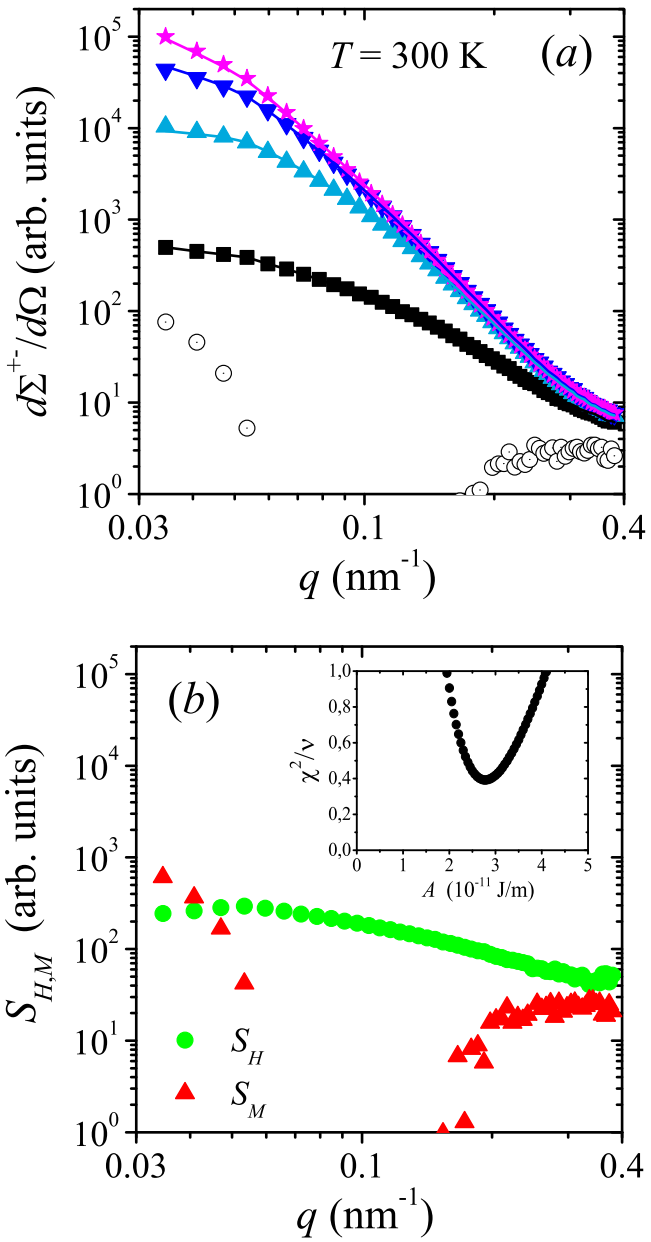

Figure 23. (*a*) Azimuthally-averaged spin-flip SANS cross-section $\mathrm{d}\Sigma^{+-}/\mathrm{d}\Omega$ of nanocrystalline Co (average grain size: 9.5 ± 3.0 nm) as a function of momentum transfer q ($\mathbf{k}_0 \perp \mathbf{H}_0$) at selected applied magnetic fields (log–log scale); field values (in mT) from bottom to top: 1239, 181, 53, 24. The solid lines represent a fit of the data to the micromagnetic theory (equation (115)). (○) Residual scattering cross-section $\mathrm{d}\Sigma_{\mathrm{res}}/\mathrm{d}\Omega = (\pi^3/V)b_H^2|\widetilde{M}_z(q)|^2$. Data taken from [67]. (*b*) Scattering functions of the anisotropy field $S_H = (8\pi^3/V)b_H^2|h(q)|^2$ and of the longitudinal magnetization $S_M = (8\pi^3/V)b_H^2|\widetilde{M}_z(q)|^2$ (log–log scale). The inset depicts the (reduced) weighted mean-square deviation between experiment and fit, χ^2/ν, as a function of the exchange-stiffness constant A.

magnetization profile and on the shape of the correlations. Section 5.3 discusses (for the example of a NdFeB-based nanocomposite) the field dependence of experimental spin-misalignment correlations, and it is shown that the ratio of anisotropy-field strength H_p to magnetization jump ΔM at internal interfaces determines the size of gradients in the spin-microstructure.

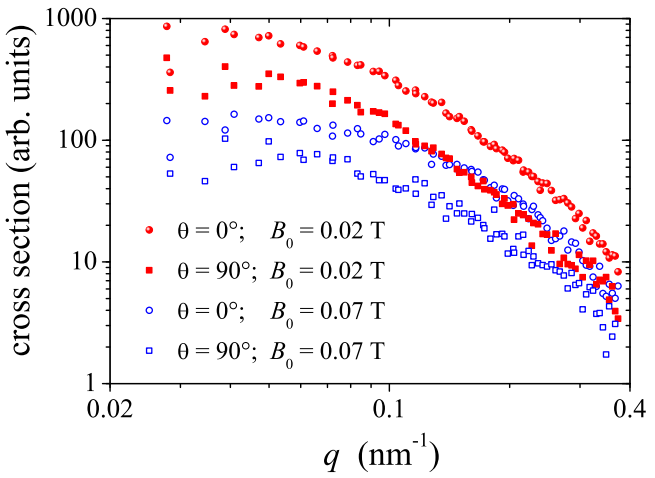

Figure 24. Field dependence of ($\pm 7.5^\circ$) sector averages of the spin-flip cross-section of an FeCr-based nanocomposite ($\mathbf{k}_0 \perp \mathbf{H}_0$) (log–log-scale). The curves labelled $\theta = 90^\circ$ are related to $|\widetilde{M}_x|^2$, while the $\theta = 0^\circ$ data are proportional to $|\widetilde{M}_x|^2 + |\widetilde{M}_y|^2$ (compare equation (72)). Reproduced from [48] with permission from Springer Science & Business Media.

5.1. Definition

The autocorrelation function $C(\mathbf{r})$ of the spin-misalignment is defined by close analogy to the well-known Patterson function in x-ray crystallography [207] as [58, 63, 66]

$$C(\mathbf{r}) = \frac{1}{V}\int \frac{\delta\mathbf{M}(\mathbf{r}')\,\delta\mathbf{M}(\mathbf{r}'+\mathbf{r})}{M_s^2}\,\mathrm{d}^3r', \qquad (120)$$

where V is the sample volume, and $\delta\mathbf{M}(\mathbf{r}) = \mathbf{M}(\mathbf{r}) - \langle\mathbf{M}\rangle$ denotes the fluctuation of the local magnetization $\mathbf{M}(\mathbf{r})$ about its position-independent average $\langle\mathbf{M}\rangle$, which in the high-field limit is directed along the externally applied magnetic field $\mathbf{H}_0$.

For an isotropic distribution of the magnetization Fourier coefficient, it was shown in [58] that $C(r)$ can be related to the experimental spin-misalignment SANS cross-section $\mathrm{d}\Sigma_M/\mathrm{d}\Omega$ according to

$$C(r) = \frac{w}{2\pi^2 b_m^2 \rho_a^2 r}\int_0^\infty \frac{\mathrm{d}\Sigma_M}{\mathrm{d}\Omega}\sin(qr)\,q\,\mathrm{d}q, \qquad (121)$$

where $w = 3/2$ at small applied magnetic field (demagnetized state), and $w = 4/3$ for the nearly saturated, texture-free ferromagnet; b_m and ρ_a denote, respectively, the atomic magnetic scattering length and the atomic density. From experimental correlation functions, one may then estimate the correlation length l_C of the spin-misalignment, which is a measure for the size of inhomogeneously magnetized regions around lattice imperfections. We have identified l_C with the r-value for which the extrapolated value of $C(r)$ to the origin, $C(0)$, has decayed to $C(0)\exp(-1)$, i.e.

$$l_C = r \quad \text{for which} \quad C(r) = C(0)\exp(-1). \qquad (122)$$

5.2. Magnetization profiles and correlation functions

Based on linearized micromagnetic theory, we have computed in [66] the autocorrelation function of the spin-misalignment for various models for the magnetic anisotropy field. In

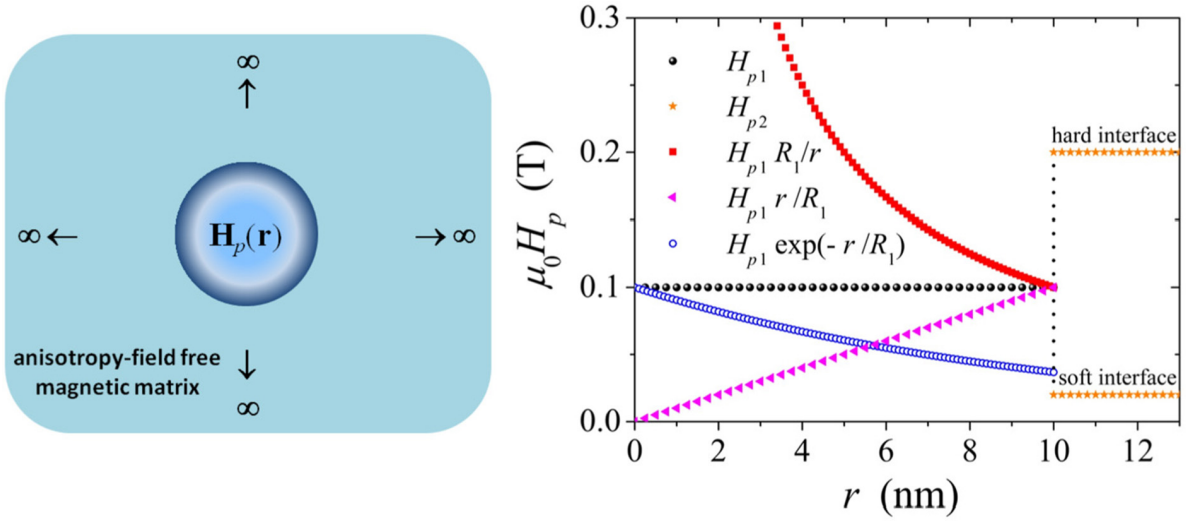

Figure 25. Models for the spatial structure of the magnetic anisotropy field $H_p(r)$ of a spherical particle (core-shell), which is embedded in an anisotropy-field free, infinitely extended magnetic matrix. The following functional dependencies for $H_p(r)$ are assumed: $H_p(r) = H_{p1}$ = constant for $r \leqslant R_1$ (uniform sphere); $H_p(r) = H_{p1}$ for $r \leqslant R_1$ and $H_p(r) = H_{p2}$ for $R_1 \leqslant r \leqslant R_2$ (uniform core-shell particle); $H_p(r) = H_{p1}\exp(-r/R_1)$ (exponential decay); $H_p(r) = H_{p1}(R_1/r)$ (power-law decay); $H_p(r) = H_{p1}(r/R_1)$ (linear increase). Depending on whether the anisotropy field of the shell, H_{p2}, is larger or smaller than H_{p1}, the interface is denoted as a hard or soft interface. For illustration purposes, we have chosen $R_1 = 10\,\mathrm{nm}$, $R_2 = 13\,\mathrm{nm}$, $\mu_0 H_{p1} = 0.1\,\mathrm{T}$, and $\mu_0 H_{p2} = 0.2\,\mathrm{T}$ (0.02 T). Reprinted with permission from [66]. Copyright 2010 by the American Physical Society.

particular, we have considered a single isolated spherical nanoparticle that is embedded in an infinitely extended magnetic matrix. The particle is characterized by its magnetic anisotropy field $\mathbf{H}_p(\mathbf{r})$, whereas the matrix is assumed to be anisotropy-field free. For different spatial profiles of $\mathbf{H}_p$ (uniform sphere, uniform core-shell, linear increase, exponential and power-law decay), the magnetization response around the defect and the corresponding correlation functions were calculated. Figure 25 displays the considered models for $H_p(r)$. The theory assumes uniform values for A and M_s, i.e. jumps in M_s are not taken into account, and the spin-misalignment SANS reduces to $\mathrm{d}\Sigma_M/\mathrm{d}\Omega = S_H R_H$ (compare equation (103)); the case $\mathrm{d}\Sigma_M/\mathrm{d}\Omega = S_H R_H + S_M R_M$ is considered in section 5.3 below. Analytical expressions for the Fourier coefficients $\mathbf{h}$ of $\mathbf{H}_p$ can be found in [66]; magnetic materials parameters assumed for Ni were $A = 8.2\,\mathrm{pJ\,m^{-1}}$ and $M_s = 500\,\mathrm{kA\,m^{-1}}$.

We would like to particularly emphasize that in the model calculations on homogeneous single-phase low-anisotropy ferromagnets reported in [66], the magnetostatic field $\mathbf{H}_d$ due to $\nabla \cdot \mathbf{M} \neq 0$ is neglected. Specifically, this means that (besides the $\widetilde{M}_z$ contribution) the term $M_s q_y^2/q^2 = M_s \sin^2\theta$ in the denominator of equation (43) is not taken into account. As one may expect, this simplification is justified in the high-field regime when the magnetization is nearly aligned along the applied magnetic field. Figure 26 shows the effect of $\mathbf{H}_d$ on the magnetization profiles, correlation functions, and on the spin-misalignment length. Since the inclusion of the magnetostatic field suppresses $\mathbf{M}(\mathbf{q})$ (compare equation (43)), both M_p/M_s and C at a given field are larger without $\mathbf{H}_d$ (solid lines in figures 26(a) and (b)) than with $\mathbf{H}_d$ (dashed lines). The difference between the two cases becomes progressively smaller as the applied field is increased, thus, corroborating that dipole-field effects are indeed negligible at the larger fields and for the particular system under study. Moreover, the shapes of the $\frac{M_p}{M_s}(r)$ and $C(r)$ curves are very similar and the resulting values for the correlation length l_C of the spin-misalignment are almost identical (figure 26(c)). Without going into too much detail, figure 26 should simply serve as a 'reminder' that for the discussion of the following results (figures 27–30 and figure 37) the magnetodipolar interaction is of minor importance. The influence of the magnetostatic interaction on the spin-misalignment correlations of *inhomogeneous* magnets such as two-phase nanocomposites is discussed in figure 36 below.

The applied-field dependence of the reduced transversal magnetization $\frac{M_p}{M_s}(r)$ (for the various anisotropy-field models depicted in figure 25) are shown in figure 27. Increasing the applied field suppresses transversal spin fluctuations. The M_p/M_s curves reveal that the perturbation which is caused by the anisotropy-field of the particle is largest at the centre of the dominating defect, and then M_p/M_s decays smoothly at the larger distances. While the data for the uniform-sphere model (figure 27(a)) and the exponential decay case (figure 27(c)) are qualitatively similar, the shapes of the other two M_p/M_s curves are significantly different: the core-shell particle (figure 27(b)) exhibits a peak in M_p/M_s due to the presence of the hard shell (at $10\,\mathrm{nm} \leqslant r \leqslant 13\,\mathrm{nm}$), and for the power-law decay case (figure 27(d)), we find an almost linear decrease of M_p/M_s at small r and not loo large fields. Note that the M_p/M_s for a soft interface (i.e. $H_{p1}/H_{p2} > 1$) are qualitatively similar to the uniform-sphere case.

The results in figure 27 also demonstrate the special role of the exchange length $l_H(H_i) = \sqrt{2A/(\mu_0 M_s H_i)}$, which can be taken as the spatial resolution limit of the magnetization [131]. Variations in the magnetic anisotropy field on a characteristic microstructural length scale $\mathcal{L}$ can be followed by the magnetization only when $l_H \lesssim \mathcal{L}$. At the largest fields, l_H is of the

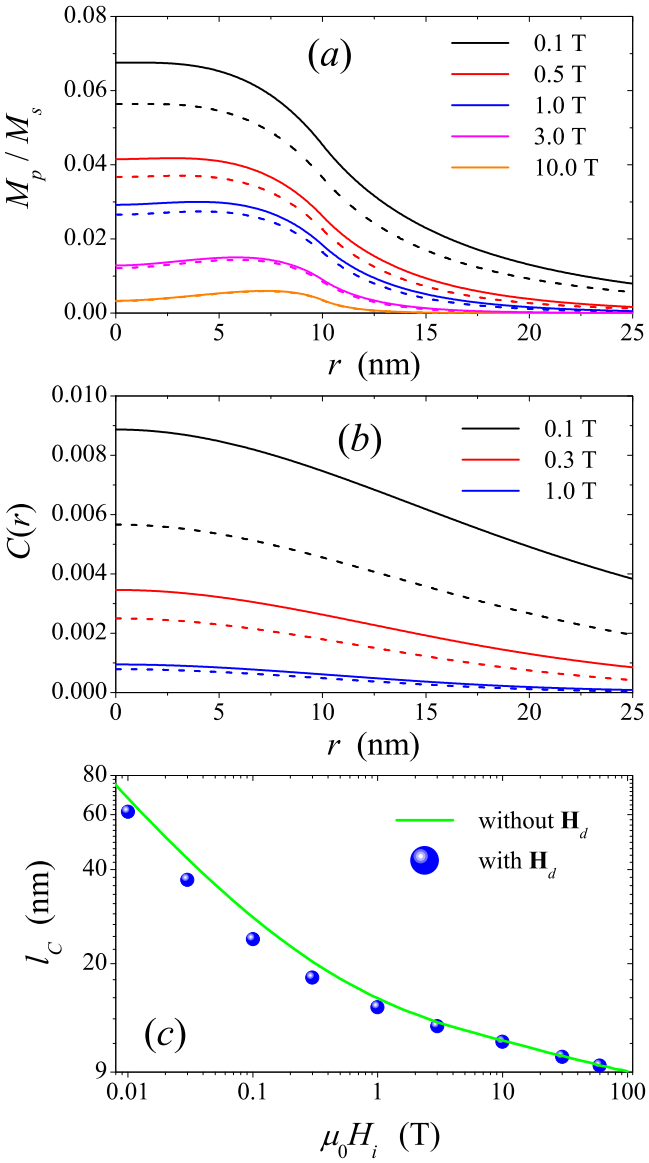

Figure 26. Effect of the magnetostatic interaction on (*a*) the magnetization profiles M_p/M_s and (*b*) the correlation functions $C(r)$. In the calculation, we have assumed uniform values for A and M_s, and the particle's anisotropy field increases linearly with position, i.e. $H_p(r) = H_{p1}(r/R_1)$ with $\mu_0 H_{p1} = 0.1$ T and $R_1 = 10$ nm (compare figure 25). Values of the applied magnetic field are indicated in the insets and increase from top to bottom, respectively. Solid lines: no magnetostatic field. Dashed lines: with magnetostatic field. (*c*) Field dependence of the spin-misalignment length l_C (log–log scale) obtained by ignoring $\mathbf{H}_d$ (solid line) and by taking into account $\mathbf{H}_d$ (•). Reprinted with permission from [66]. Copyright 2010 by the American Physical Society.

order of a few nm, e.g. $l_H(5\,\mathrm{T}) \cong 2.6$ nm for Ni, with the consequence that sharp variations in M_p/M_s on a scale of the order of l_H can be resolved. This can be clearly seen, for instance in figure 27(*b*), where the perturbing effect of the magnetically hard shell is only seen at the largest field values, and it gives rise to a peak feature which is washed out at the lower fields.

In agreement with the M_p/M_s curves, the corresponding correlation functions shown in figure 28 are strongly field dependent and reveal the long-range nature of the spin-misalignment fluctuations. Despite the existing differences in the underlying functional dependencies of $H_p(r)$ and the associated M_p/M_s data (compare figure 27), the shapes of the different $C(r)$ in figure 28 appear to be closely similar: for the anisotropy-field microstructures investigated in this study, $C(r)$ at a given field takes on the maximum value at $r = 0$ with $(\mathrm{d}C/\mathrm{d}r)_{r\to 0} = 0$ and then decays towards $C = 0$ for $r \to \infty$. Clearly, the correlations do neither decay exponentially nor according to the Ornstein–Zernike formula.

Figure 29 compares the shapes of the $C(r)$ for the uniform-sphere and the uniform core-shell model with hard interfaces; the inset depicts the corresponding derivatives $\frac{\mathrm{d}C(r)}{\mathrm{d}r}$.

The observation in figures 28 and 29 that the slope of $C(r)$ at the origin vanishes is consistent with the lack of a sharp boundary in the magnetic microstructure and with the absence of an asymptotic q^{-4} Porod behaviour of $\mathrm{d}\Sigma_M/\mathrm{d}\Omega = S_H R_H$, which may be as steep as q^{-8} (compare figure 15). The magnetic SANS that is of interest here is due to infinitely extended smoothly varying magnetization profiles. Correspondingly, the linear term in the expansion of C in powers of r is absent [152], i.e.

$$C(r) \cong C(0) - ar^2 + \ldots \tag{123}$$

(compare figure 34). By comparison, the correlation function of a single uniform sphere with radius R reads $C(r) = 1 - 3r/(4R) + r^3/(16R^3)$ for $r \leqslant 2R$, and $C = 0$ for $r > 2R$.

The value of the correlation function at the origin, $C(r = 0)$, is equal to the reduced mean-square magnetization fluctuation (compare equation (120)) and describes the approach-to-saturation behaviour, according to [58]

$$M(H_i) = M_s\sqrt{1 - C(0, H_i)}. \tag{124}$$

Figure 30 displays the field dependence of $C(0)$ for the various anisotropy-field models shown in figure 25. Closed-form expressions for $C(0)$ can be found in [199] and [66].

For the case of a spherical particle (crystallite) with a uniform magnetic anisotropy field and neglecting the magnetostatic field due to nonzero volume divergences of the magnetization, the following closed-form expression for $C(r)$ can be derived [68],

$$C(r) = \frac{K R^4}{H_i^2} \int_0^\infty \frac{J_0(qr)\, J_1^2(qR)}{(1 + l_H^2\, q^2)^2}\, \mathrm{d}q, \tag{125}$$

where $K = 8H_p^2 V^{-1}$, and J_0 and J_1 denote, respectively, the spherical Bessel functions of zeroth and first order. The parameter R represents the corresponding 'anisotropy-field' radius, and it is emphasized that R is not necessarily identical with the average crystallite size. Figure 31 shows the field-dependent (experimental) correlation functions of nanocrystalline Co and Ni metal together with *global* fits to equation (125) (solid lines).

From the fit, one obtains the following values for the exchange-stiffness constants, $A = 35 \pm 1$ pJ m^{-1} for nanocrystalline Co and $A = 9.2 \pm 0.1$ pJ m^{-1} for nanocrystalline Ni. These values are about $10 - 20$ % larger than the values that were previously obtained by analyzing the field-dependent

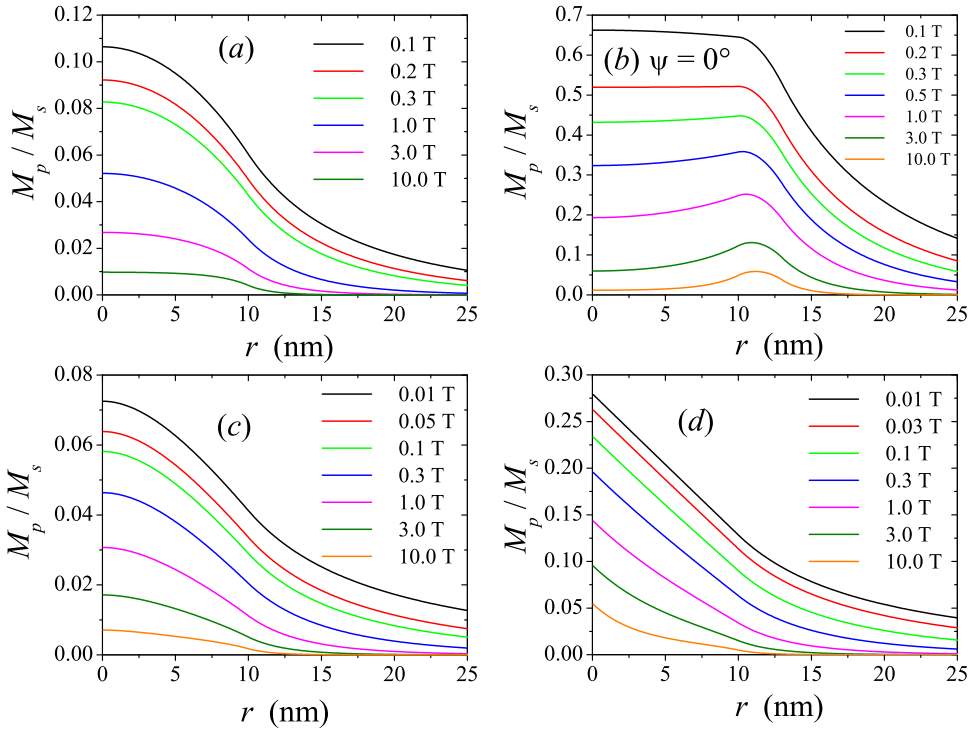

Figure 27. Reduced transversal magnetization component M_p/M_s as a function of the distance r from the centre of the inclusion (at $r = 0$). Values of the applied magnetic field are indicated in the insets and increase from top to bottom, respectively. (*a*) Uniform-sphere model ($R_1 = 10\,\text{nm}$, $\mu_0 H_{p1} = 0.1\,\text{T}$). (*b*) Uniform core-shell model with hard interfaces ($R_1 = 10\,\text{nm}$, $R_2 = 13\,\text{nm}$, $H_{p1}/H_{p2} = 0.1$). $\psi = 0^\circ$ denotes the angle between the anisotropy field of the core and the shell. (*c*) Exponential decay. (*d*) Power-law decay. The corresponding correlation functions $C(r)$ are displayed in figure 28. Reprinted with permission from [66]. Copyright 2010 by the American Physical Society.

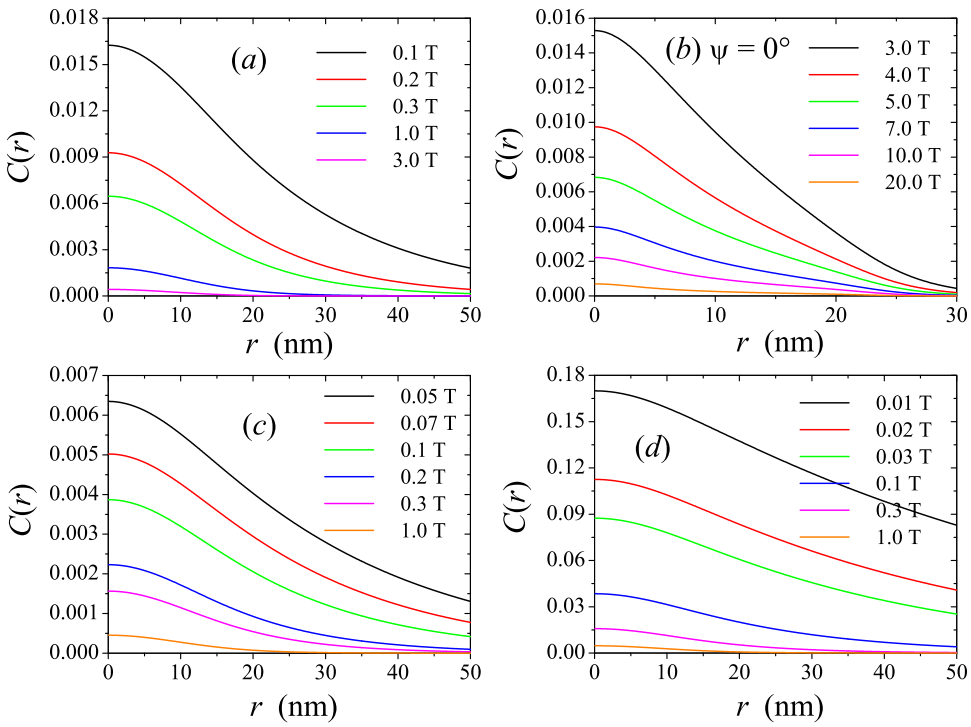

Figure 28. Results for the field dependence of the correlation function $C(r)$ of the spin-misalignment. Values of the applied magnetic field are indicated in the insets and increase from top to bottom, respectively. (*a*) Uniform-sphere model ($R_1 = 10\,\text{nm}$, $\mu_0 H_{p1} = 0.1\,\text{T}$). (*b*) Uniform core-shell model with hard interfaces ($R_1 = 10\,\text{nm}$, $R_2 = 13\,\text{nm}$, $H_{p1}/H_{p2} = 0.1$). $\psi = 0^\circ$ denotes the angle between the anisotropy field of the core and the shell. (*c*) Exponential decay. (*d*) Power-law decay. Reprinted with permission from [66]. Copyright 2010 by the American Physical Society.

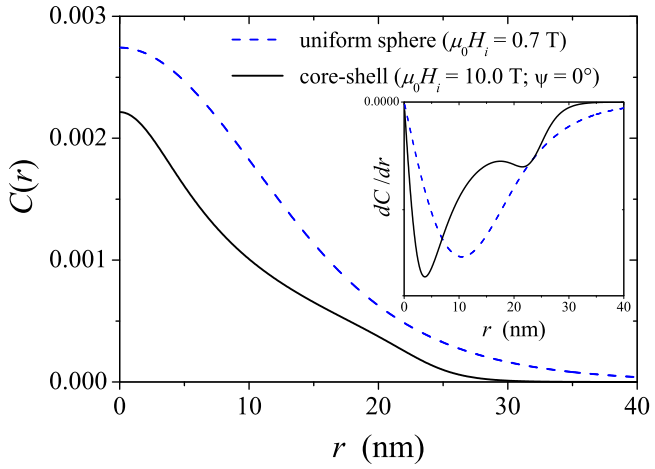

Figure 29. Correlation functions $C(r)$ of the spin-misalignment for the uniform-sphere model ($R_1 = 10$ nm, $\mu_0 H_{p1} = 0.1$ T) and for the uniform core-shell model with hard interfaces ($R_1 = 10$ nm, $R_2 = 13$ nm, $H_{p1}/H_{p2} = 0.1$). Inset: respective derivatives dC/dr. $\psi = 0°$ denotes the angle between the anisotropy field of the core and the shell. Reprinted with permission from [66]. Copyright 2010 by the American Physical Society.

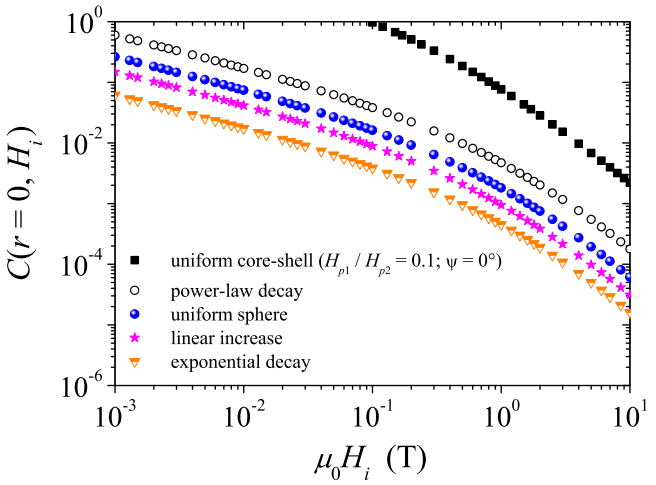

Figure 30. Applied-field dependence of the reduced mean-square magnetization fluctuation $C(r = 0, H_i) = M_s^{-2}\langle|\delta\mathbf{M}|^2\rangle$ for different spatial profiles of the magnetic anisotropy field (see inset) (log–log scale). The observation that $C(0, H_i)$ for the hard core-shell model takes on values > 1 at small fields suggests that here the small-misalignment approximation is not valid anymore; $\psi = 0°$ denotes the angle between the anisotropy field of the core and the shell. Reprinted with permission from [66]. Copyright 2010 by the American Physical Society.

SANS data in reciprocal space in terms of micromagnetic theory [26]. The values for the anisotropy-field radius, $R = 14.3 \pm 0.2$ nm (Co) and $R = 13.6 \pm 0.1$ nm (Ni), are consistent with previous results and conclusions [63, 68].

5.3. Field dependence of spin-misalignment correlations

A quantity of particular interest in the analysis of experimental spin-misalignment scattering data is the correlation length l_C of the spin-misalignment, which specifies the range over which perturbations in the spin structure (around a lattice defect) are transmitted by the exchange interaction into the surrounding crystal lattice (compare figure 1). Besides its obvious dependence on the applied magnetic field, l_C may depend on the magnetic interaction parameters (A, K, M_s, λ), and on the nature and spatial extension (size) of the defect. For a polycrystalline bulk ferromagnet containing a large amount of different imperfections, the experimental value(s) for l_C represents a weighted average over the different defects. There exists a close relationship between l_C and the micromagnetic exchange length l_H (see below).

In the following, we briefly discuss the prototypical SANS data analysis for the example of a two-phase NdFeB-based nanocomposite, which consists of hard magnetic $Nd_2Fe_{14}B$ particles (size: ∼22 nm) and Fe_3B crystallites (size: ∼29 nm) [55, 56]. It is important to mention that for this particular alloy the difference ΔM in the saturation magnetizations of the $Nd_2Fe_{14}B$ phase and the Fe_3B crystallites is rather small, $\mu_0 \Delta M \cong 0.01$ T [208]. As a consequence, the related longitudinal magnetic SANS $\propto |\widetilde{M}_z|^2 \propto (\Delta M)^2$ is negligible as compared to the nuclear SANS $|\widetilde{N}|^2$.

Figure 32(*a*) displays the total unpolarized $d\Sigma/d\Omega$ of the NdFeB nanocomposite. A strong field dependence between the largest applied field of 10 T and the coercive field of $\mu_0 H_c = -0.55$ T is observable. Since nuclear SANS is field independent and since SANS due to $|\widetilde{M}_z|^2$ fluctuations is negligible (for this particular alloy), it is evident that the dominating contribution to $d\Sigma/d\Omega$ is due to transversal spin-misalignment. In order to (approximately) obtain the corresponding spin-misalignment SANS $d\Sigma_M/d\Omega$ (see figure 32(*b*)), the $d\Sigma/d\Omega$ at 10 T was subtracted from the $d\Sigma/d\Omega$ at lower fields (compare equation (93)). The resulting $d\Sigma_M/d\Omega$ is of comparable magnitude as $d\Sigma/d\Omega$, but possesses a strikingly different q-dependency. In particular, the shoulder in $d\Sigma/d\Omega$ at about $q = 0.2\,\mathrm{nm}^{-1}$ is absent in $d\Sigma_M/d\Omega$. Possible origins for the shoulder in $d\Sigma/d\Omega$ are interparticle interferences and/or diffusion zones around the particles, as discussed in [42]. The different shapes of $d\Sigma/d\Omega$ and $d\Sigma_M/d\Omega$ are also reflected in different asymptotic power-law exponents n (see figure 33).

While the spin-misalignment SANS is characterized by power-law exponents which range between $n \sim 5$–6 at all fields investigated, the total unpolarized SANS reveals significantly lower values for n, which approach the Porod value of $n = 4$ at 10 T. This finding in conjunction with the observation that the two-dimensional $d\Sigma/d\Omega$ at 10 T is approximately isotropic (data not shown) provides support for the conclusion that the $d\Sigma/d\Omega$ data at 10 T (and large q) are essentially due to nuclear particle scattering.

Fourier transformation of the $d\Sigma_M/d\Omega$ data according to equation (121) yields the correlation function $C(r)$ of the spin-misalignment (see figure 34). The field-dependent correlations in figure 34 do not decay exponentially, in agreement with the absence of an $n = 4$ power-law exponent in $d\Sigma_M/d\Omega$. Furthermore, the $C(r)$ seem to approach the origin $r = 0$ with zero slope (dotted line in figure 34), which is in agreement with the notion of magnetic SANS from continuous magnetization

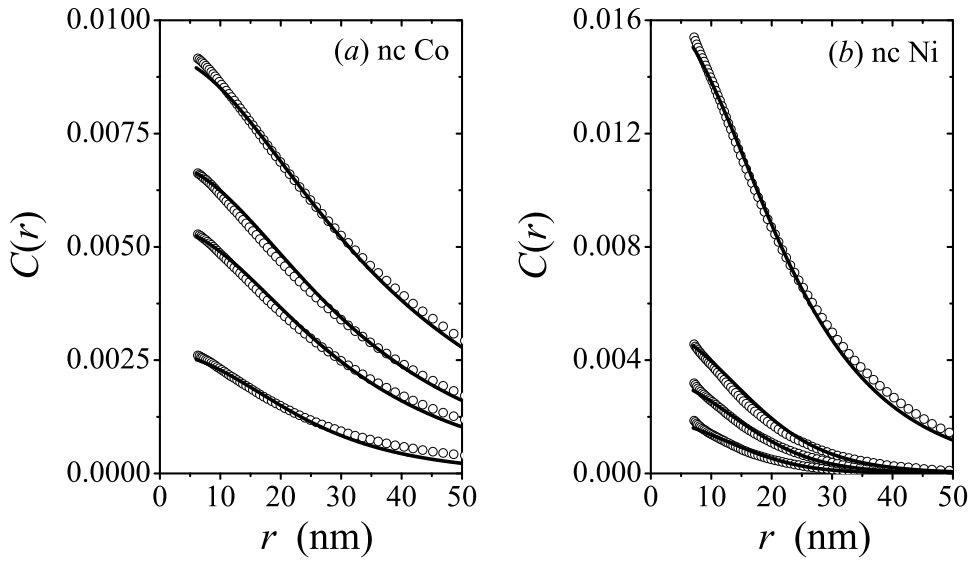

Figure 31. (○) Applied-field dependence of the autocorrelation function $C(r)$ of the spin-misalignment of (*a*) nanocrystalline Co and (*b*) nanocrystalline Ni with average crystallite sizes of 10 nm (Co) and 49 nm (Ni) [62]. Values of the internal magnetic field H_i (in mT) from top to bottom, respectively: (*a*) 54, 80, 107, 243; (*b*) 190, 570, 800, 1240. Solid lines in (*a*) and (*b*) represent a fit to equation (125). $M_s = 1434\,\mathrm{kA\,m^{-1}}$ for Co and $M_s = 522\,\mathrm{kA\,m^{-1}}$ for Ni were assumed. Reproduced with permission of the International Union of Crystallography from [68].

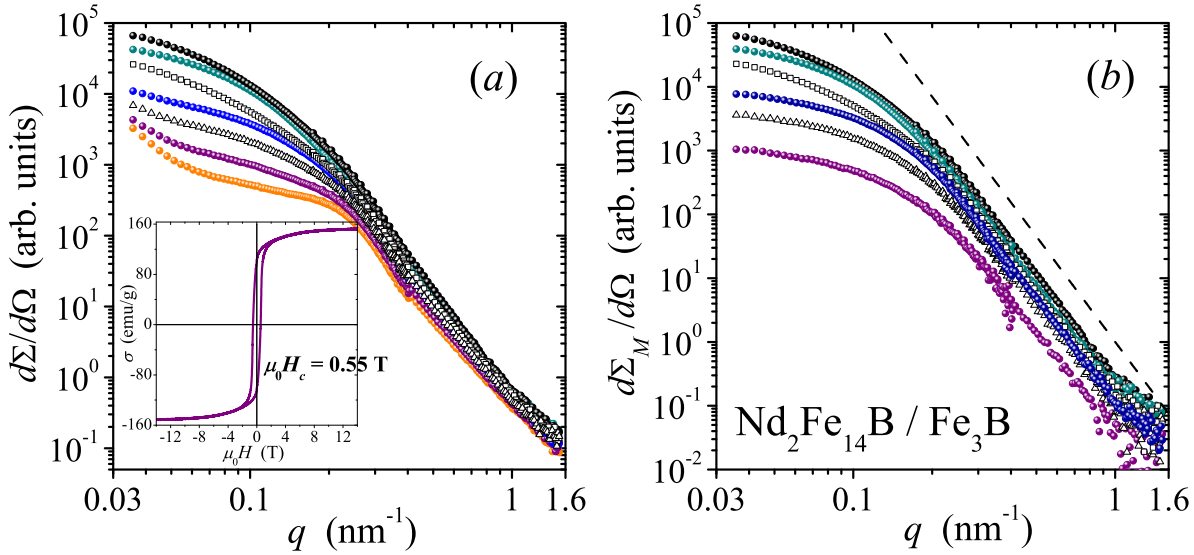

Figure 32. (*a*) Azimuthally-averaged total SANS cross-section $\mathrm{d}\Sigma/\mathrm{d}\Omega$ of $Nd_2Fe_{14}B/Fe_3B$ as a function of momentum transfer q and applied magnetic field H ($T = 300\,\mathrm{K}$) ($\mathbf{k}_0 \perp \mathbf{H}_0$) (log–log scale). Solid circles (●): applied-field values (in Tesla) decrease from bottom to top: 10, 6, 1, −0.25, −0.55; (□): −1 T; (△): −3 T. Inset: room-temperature magnetization curve of $Nd_2Fe_{14}B/Fe_3B$. (*b*) Applied-field dependence of the spin-misalignment SANS cross-section $\mathrm{d}\Sigma_M/\mathrm{d}\Omega$ of nanocrystalline $Nd_2Fe_{14}B/Fe_3B$. Solid circles (●): field values (in Tesla) decrease from bottom to top: 6, 1, −0.25, −0.55; (□): −1 T; (△): −3 T. The $\mathrm{d}\Sigma_M/\mathrm{d}\Omega$ data displayed in (*b*) were obtained by subtracting the 10 T data shown in (*a*) from the $\mathrm{d}\Sigma/\mathrm{d}\Omega$ at lower fields. Dashed line: $\mathrm{d}\Sigma_M/\mathrm{d}\Omega \propto q^{-5.5}$. Reproduced with permission from [55]. Copyright 2013, American Institute of Physics.

profiles and the absence of a sharp interface in the magnetic microstructure [152].

By means of the extrapolated value of the correlation function at the origin, $C(0)$, one can determine the correlation length l_C of the spin-misalignment. We used the definition $C(r = l_C) = C(0)\exp(-1)$ (equation (122)), which yields the exact correlation length for correlations with exponential decay. The values of l_C obtained in this way are plotted in figure 35 as a function of the applied magnetic field, which is usually the control parameter in magnetic SANS experiments.

In previous studies [26, 53, 55, 63, 66], we have found that $l_C(H_0)$ data can be well described by an equation of the type

$$l_C(H_0) = \mathcal{L} + \sqrt{\frac{2A}{\mu_0 M_s\,(H_0 + H^\star)}}, \qquad (126)$$

where the *field-independent* parameter $\mathcal{L}$ is of the order of the defect size and the second *field-dependent* term on the right hand side represents a modified exchange length l_H of the field.

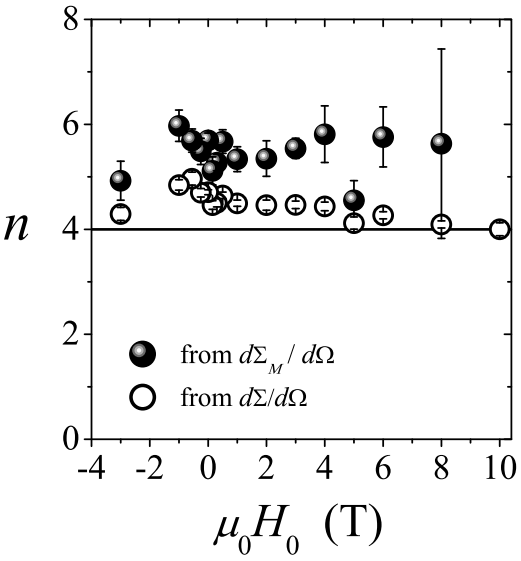

Figure 33. Field dependence of the power-law exponent n which was determined by a fit of, respectively, $\mathrm{d}\Sigma/\mathrm{d}\Omega$ (figure 32(a)) and $\mathrm{d}\Sigma_M/\mathrm{d}\Omega$ (figure 32(b)) to C/q^n (C = constant). In both cases, the fit was restricted to the interval $0.6\,\mathrm{nm}^{-1} \leqslant q \leqslant 0.7\,\mathrm{nm}^{-1}$. Solid horizontal line: $n = 4$. Reproduced with permission from [55]. Copyright 2013, American Institute of Physics.

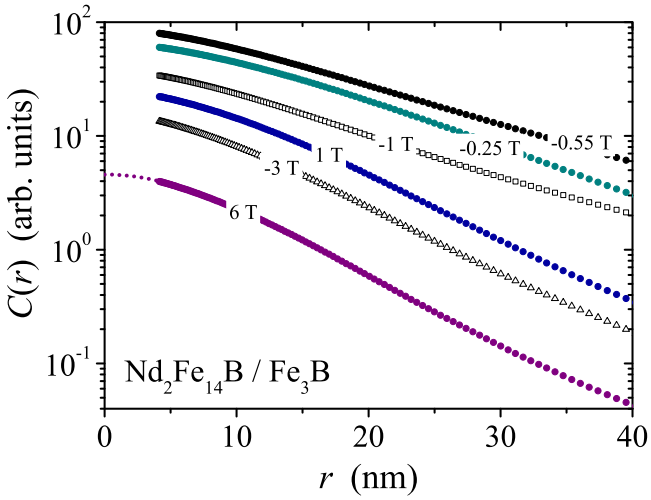

Figure 34. Field dependence of the correlation function $C(r)$ of the spin-misalignment of nanocrystalline $Nd_2Fe_{14}B/Fe_3B$ (log-linear scale). The field values follow the course of a hysteresis loop, starting from a large positive field and then reducing the field to negative values (see insets). Dotted line (extrapolating the 6 T data to $r = 0$): $C(r) = 4.58 - 0.043\,r^2$. Reproduced with permission from [55]. Copyright 2013, American Institute of Physics.

Equation (126) is a phenomenological prediction based on micromagnetic theory, which embodies the convolution relationship between the magnetic anisotropy-field microstructure $\mathbf{H}_p(\mathbf{r})$ and micromagnetic response functions which decay with l_H [62, 199]. The 'correlation length' $\mathcal{L}$ of the magnetic anisotropy field appears to be the average size over which the direction and/or magnitude of $\mathbf{H}_p$ changes. For a statistically isotropic polycrystalline material, where each crystallite is a single crystal with magnetocrystalline anisotropy only, the parameter $\mathcal{L}$ is sensibly related to the average crystallite

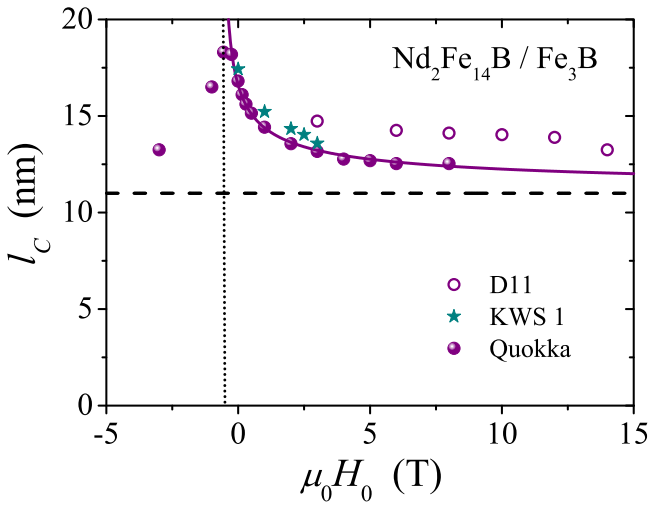

Figure 35. Applied-field dependence of the correlation length l_C of the spin-misalignment of nanocrystalline $Nd_2Fe_{14}B/Fe_3B$. Solid line: fit of the data to equation (126), where $\mathcal{L} = 10.9$ nm and $\mu_0 H^\star = +0.60$ T are treated as adjustable parameters, and the quantities $A = 12.5\,\mathrm{pJ\,m^{-1}}$ and $\mu_0 M_s = 1.6$ T are held fixed. In addition to $l_C(H_0)$ data obtained at the instrument Quokka (ANSTO, Australia), results obtained at the SANS instruments KWS 1 (JCNS, Germany) and D11 (ILL, France) are also shown. Dashed horizontal line: average radius of the $Nd_2Fe_{14}B$ particles ($R = 11$ nm). Dotted vertical line: coercive field $\mu_0 H_c = -0.55$ T. Reproduced with permission from [55]. Copyright 2013, American Institute of Physics.

size [53, 66]. The field $H^\star$ (introduced in [55]) is expected to model the influence of the magnetodipolar interaction and of the magnetic anisotropy. For soft magnetic materials with low crystalline anisotropy at large applied magnetic fields (when the magnetostatic interaction may be negligible), one may ignore the field $H^\star$, so that $l_C = \mathcal{L} + l_H$ (see e.g. figure 36(b) below). The latter equation has been found to excellently describe the field-dependent spin-misalignment correlations in nanocrystalline Co and Ni [63]. By contrast, for (uniaxial) hard magnets, the anisotropy field $H_K = 2K_u/M_s$, which for $Nd_2Fe_{14}B$ single crystal is about 8 T at 300 K [209], is expected to cut down the size of spin inhomogeneities. Likewise, jumps ΔM of the magnitude of the magnetization at internal phase boundaries, which in Fe-based nanocomposites can be as large as 1.5 T [46], give rise to magnetic torques that produce spin disorder in the surrounding magnetic phase; such kind of perturbations also decrease the size of gradients in the magnetization (see figure 36 below). It is interesting to note that at $H_0 = 0$ and for $H^\star = H_K = 2K_u/(\mu_0 M_s)$, equation (126) reduces to $l_C = \mathcal{L} + \sqrt{A/K_u}$.

For the NdFeB nanocomposite (with $\Delta M \cong 0$), we expect that l_C describes the spatial extent of magnetization inhomogeneities, mainly within the soft magnetic Fe_3B grains, that are caused by the jump in the magnetic materials parameters (exchange constant, direction and magnitude of magnetic anisotropy) at the interface between the $Nd_2Fe_{14}B$ particles and the surrounding Fe_3B crystallites. As can be seen in figure 35, l_C approaches a constant value of about 12.5 nm at the largest positive fields and increases with decreasing applied field to take on a maximum value of about 18.5 nm at the experimental coercive field of $\mu_0 H_c = -0.55$ T. Further

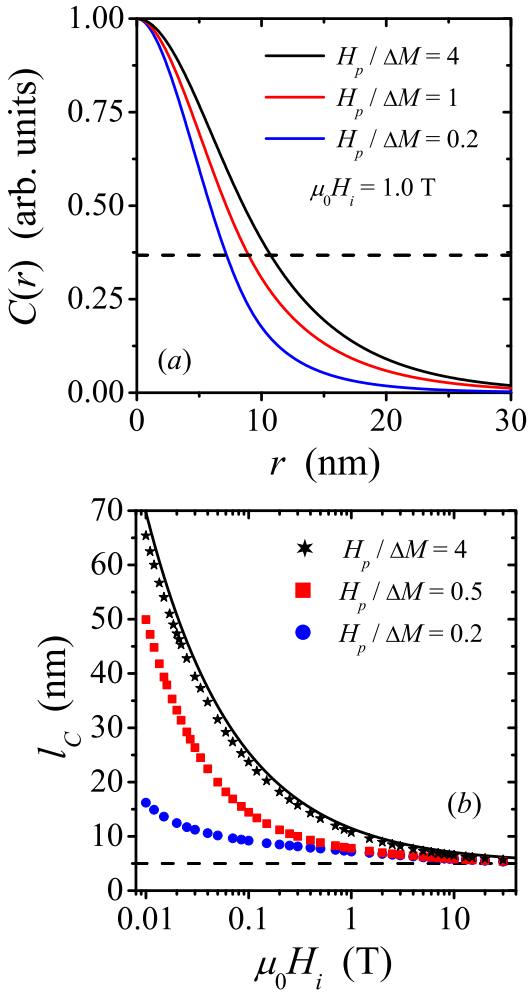

Figure 36. (*a*) Normalized autocorrelation function $C(r)$ of the spin-misalignment at $\mu_0 H_i = 1.0$ T and for different ratios of $H_p/\Delta M$ (decreasing from top to bottom, see inset) ($\mathbf{k}_0 \perp \mathbf{H}_0$). Dashed horizontal line: $C(r = l_C) = \exp(-1)$. $C(r)$ represents the numerically-computed Fourier transform of $\mathrm{d}\Sigma_M/\mathrm{d}\Omega = S_H R_H + S_M R_M$. For $S_H \propto h^2(qR)$ and $S_M \propto \widetilde{M}_z^2(qR)$, we used the form factor of the sphere with a radius of $R = 5$ nm (equations (104) and (105)). The following materials parameters were used: $A = 2.5 \times 10^{-11}$ J m^{-1}; $\mu_0 M_s = 1.5$ T; $\mu_0 \Delta M = 0.25$ T. (*b*) Field dependence of the spin-misalignment length l_C for $\mathbf{k}_0 \perp \mathbf{H}_0$ and for different ratios of $H_p/\Delta M$ (see inset) (log-linear scale). Solid line: equation (126) with $H^\star = 0$. Dashed horizontal line: $l_C = \mathcal{L} = R = 5$ nm. Reprinted with permission from [53]. Copyright 2013 by the American Physical Society.

increase of H_0 towards more negative values results again in a decrease of l_C towards $\sim$ 12.5 nm. From the fit of the $l_C(H_0)$ data to equation (126) (solid line in figure 35), we obtain $\mathcal{L} = 10.9$ nm (close to the experimental average grain radius of the $Nd_2Fe_{14}B$ phase) and $\mu_0 H^\star = +0.60$ T, which is close to the absolute value of the experimental coercive field. At the remnant state, the penetration depth of the spin disorder into the Fe_3B phase amounts to $\sim$5–6 nm.

The influence of internal magnetostatic stray fields in two-phase nanocomposites on the range of the spin-misalignment correlations has been investigated in [53]. We remind the reader that for a bulk ferromagnet, where the main sources of perturbations in the spin structure are related to spatially inhomogeneous magnetic anisotropy fields and magnetostatic fields, the spin-misalignment SANS cross-section can be expressed as $\mathrm{d}\Sigma_M/\mathrm{d}\Omega = S_H R_H + S_M R_M$ (equation (103)). Figure 36(*a*) depicts the numerically-computed autocorrelation function of the spin-misalignment at a fixed applied magnetic field of 1.0 T, but for different ratios of magnetic anisotropy field strength H_p to the magnitude ΔM of the jump of the magnetization at internal particle-matrix interfaces; the field dependence of l_C for different ratios of $H_p/\Delta M$ is plotted in figure 36(*b*).

As can be seen, the ratio $H_p/\Delta M$ decisively determines the characteristic decay length l_C: increasing $H_p/\Delta M$ results in the emergence of more long-range magnetization inhomogeneities, whereas ΔM dominated perturbations in the spin structure decay on a smaller length scale. For $H_p/\Delta M \gg 1$, the data can be well described by equation (126) with $H^\star = 0$ (solid line in figure 36(*b*)). Irrespective of the value of $H_p/\Delta M$, it is observed that at large fields l_C approaches the particle radius, i.e. $l_C = \mathcal{L} = R = 5$ nm (dashed line in figure 36(*b*)).

When ΔM fluctuations can be ignored, e.g. in a homogeneous single-phase bulk ferromagnet, the spin-misalignment SANS (in the approach-to-saturation regime) reduces to $\mathrm{d}\Sigma_M/\mathrm{d}\Omega = S_H R_H$. Figure 37 depicts the results for the applied-field dependence of the spin-misalignment length l_C (extracted from the $C(r)$ shown in figure 28) for the various spatial profiles of $H_p(r)$ shown in figure 25; we remind the reader that the magnetostatic field is neglected in these calculations and that the materials parameters are for Ni.

It is seen in figure 37(*a*) that irrespective of the detailed spatial profile of H_p of the particle, the relation $l_C = \mathcal{L} + l_H$ with $\mathcal{L} = R_1 = 10$ nm (solid line) provides an excellent description of the field-dependent correlations, except for the core-shell model with hard interfaces (figure 37(*b*)), which exhibits a more complicated behaviour $l_C(H_i)$. It is also demonstrated that exponentially decaying magnetization fluctuations, which result in $l_C = l_H$ (dashed line in figure 37(*a*)), are not in accordance with $l_C = \mathcal{L} + l_H$ already at fields larger than a few 10 mT.

6. Summary, conclusions, and outlook on future challenges

We have provided a detailed discussion of magnetic small-angle neutron scattering (SANS) of bulk ferromagnets in terms of the continuum theory of micromagnetics. For this class of magnetic materials, microstructural imperfections (e.g. point defects, dislocations, interfaces, pores) play a decisive role for magnetic SANS: magnetostrictive forces due to the distortion of the crystal lattice in the vicinity of a defect, magnetocrystalline anisotropy, as well as magnetostatic stray fields, for instance due to variations of the materials parameters (exchange, anisotropy, magnetization) at internal interfaces, result in nonuniform magnetic structures, which give rise to a large and strongly field-dependent contribution to the overall magnetic SANS cross-section. In the approach-to-saturation regime, where Brown's equations of micromagnetics can be linearized, analytical expressions for the transversal Fourier coefficients $\widetilde{M}_x(\mathbf{q})$ and $\widetilde{M}_y(\mathbf{q})$ were derived. In combination with models for the longitudinal magnetization Fourier coefficient $\widetilde{M}_z(\mathbf{q})$ and the nuclear SANS $\widetilde{N}(\mathbf{q})$, this allows one to

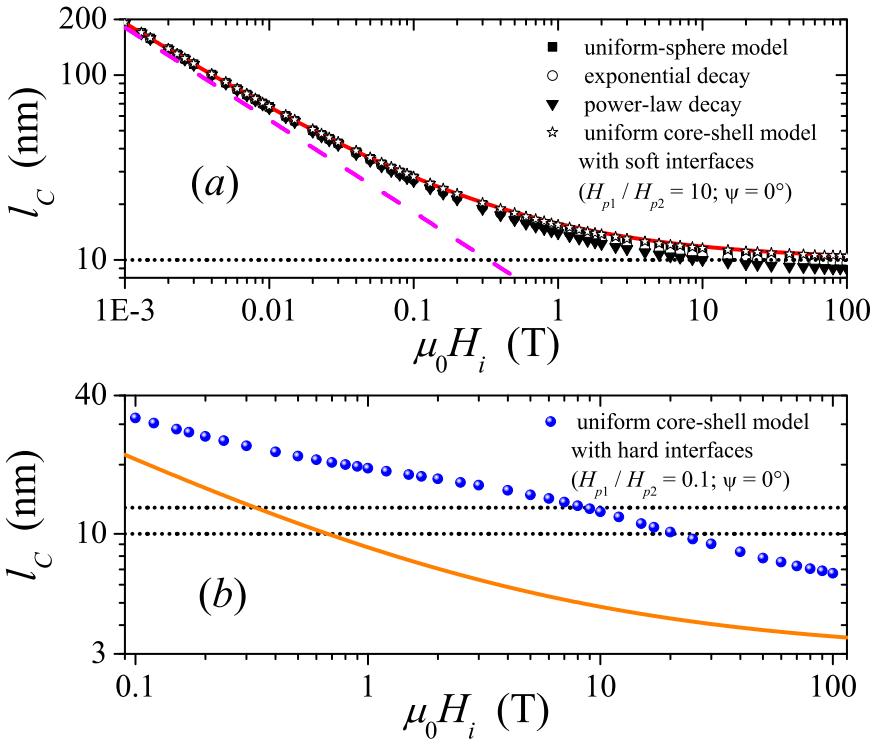

Figure 37. Results for the field dependence of the correlation length l_C of the spin-misalignment for the various models of the magnetic anisotropy field depicted in figure 25 (see insets) (log–log scale). Solid line in (*a*): $l_C = \mathcal{L} + l_H$ with $\mathcal{L} = R_1 = 10$ nm. Dashed line in (*a*): $l_C = l_H$. Dotted horizontal line in (*a*): $l_C = R_1 = 10$ nm. Solid line in (*b*): $l_C = \mathcal{L} + l_H$ with $\mathcal{L} = \Delta R = R_2 - R_1 = 3$ nm. Dotted horizontal lines in (*b*): $R_1 = 10$ nm and $R_2 = 13$ nm. $\psi = 0°$ denotes the angle between the anisotropy field of the core and the shell. Reprinted with permission from [66]. Copyright 2010 by the American Physical Society.

obtain closed-form expressions for the four spin-resolved (POLARIS) SANS cross-sections and, consequently, also for the half-polarized (SANSPOL) and unpolarized cross-sections.

For the most often employed scattering geometry, where the applied magnetic field is perpendicular to the incoming neutron beam, the results for the spin-misalignment SANS cross-section $\mathrm{d}\Sigma_M/\mathrm{d}\Omega$ exhibit a variety of angular anisotropies that are fundamentally different from the well-known $\sin^2\theta$ or $\cos^2\theta$-type patterns. In particular, by explicitly taking into account the wave-vector dependence of the longitudinal magnetization, novel terms appear in $\mathrm{d}\Sigma_M/\mathrm{d}\Omega$, which give rise to maxima roughly along the diagonals of the detector ('cloverleaf' anisotropy), in agreement with experimental observations. Besides the value of the applied magnetic field, it is the ratio of the magnetic anisotropy field H_p to the jump ΔM in the longitudinal magnetization at internal interfaces (e.g. phase boundaries) which determines the properties of $\mathrm{d}\Sigma_M/\mathrm{d}\Omega$, for instance, the asymptotic power-law exponent, the angular anisotropy, or the decay length of spin-misalignment correlations.

The micromagnetic approach also underlines the importance of the magnetodipolar interaction for understanding magnetic SANS: ignoring this interaction results (for an isotropic anisotropy-field microstructure) in all Fourier coefficients to be isotropic, in contrast to experiment. Moreover, the cloverleaf-shaped angular anisotropy in $\mathrm{d}\Sigma_M/\mathrm{d}\Omega$-which was previously [46] attributed exclusively to nanoscale jumps in the magnetization magnitude at internal interfaces-is of relevance for all bulk nanomagnets with spatially fluctuating magnetic parameters.

Analysis of unpolarized and spin-resolved experimental data of various nanocrystalline ferromagnets (hard and soft magnetic nanocomposites and elemental ferromagnets) provides values for the average exchange-stiffness constant and for the volume-averaged magnetic anisotropy field and magnetostatic field due to ΔM variations. Regarding half-polarized SANS experiments, it is pointed out that we do not observe interference between nuclear and spin-misalignment scattering amplitudes. The only spin-dependent terms in SANSPOL 'spin-up' and 'spin-down' experiments are due to $\widetilde{N}\widetilde{M}_z$ correlations, which have very weak dependence on the applied magnetic field, compared to the spin-misalignment SANS. Therefore, since spin-misalignment scattering represents the dominating contribution to the total unpolarized SANS cross-section, we believe that the measurement of the SANSPOL 'spin-up' and 'spin-down' cross-sections does not provide significantly more information regarding $\mathrm{d}\Sigma_M/\mathrm{d}\Omega$ than can already be learned by the measurement of the unpolarized cross-section alone.

Since the predictions of the present micromagnetic theory are quite generally valid in the approach-to-saturation regime, it would be of interest to use these equations in order to study related phenomena such as neutron depolarization or magnetic spin-echo small-angle neutron scattering [210–212].

The recent discovery of skyrmion lattices in metallic and semiconducting B20 transition-metal compounds [107, 153]

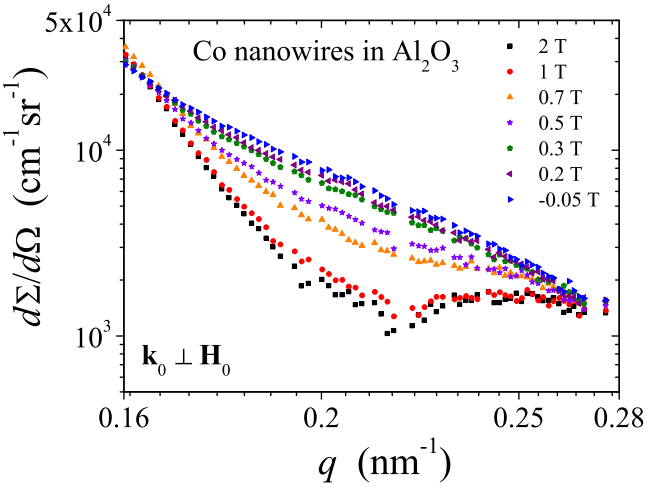

Figure 38. Applied-field dependence of the azimuthally-averaged unpolarized SANS cross-section $d\Sigma/d\Omega$ of Co nanowires (diameter: 27 ± 3 nm), which are embedded in an Al_2O_3 matrix ($\mathbf{k}_0 \perp \mathbf{H}_0$) (log–log scale). The long rod axes are aligned parallel to the incident neutron beam. Data taken from [96].

has triggered an enormous new research. Skyrmions can be viewed as a new form of particle-like order in a magnetic material. On the phenomenological level of micromagnetic theory, these features are modelled by taking into account (in the energy functional) terms which depend on the curl of the magnetization vector field ($D\mathbf{M} \cdot (\nabla \times \mathbf{M})$) ($D$: Dzyaloshinsky–Moriya constant), in addition to the usual exchange terms ($A(\nabla \mathbf{M})^2$) [213–215]. Based on our recent micromagnetic theory for the magnetic SANS of inhomogeneous ferromagnets [53], it would be of interest to investigate analytically the effect of such terms on the magnetic SANS cross-section.

The present work has focused on the magnetic microstructure within the bulk of macroscopic magnetic bodies, and, therefore, we have restricted attention to the bulk equilibrium conditions for the magnetization, equation (19). Future work may address the micromagnetic computation of the magnetic SANS of a dispersion of magnetic nanoparticles in a nonmagnetic matrix-the classical prototypical sample microstructure in magnetic SANS. There is ample experimental evidence that nanosized magnetic particles are not homogeneously magnetized (e.g. [91, 94, 96]), and the question arises whether the standard expression for the cross-section, equation (2), is still adequate to describe magnetic SANS (see also the discussion in the Introduction). As an example, we show in figure 38 the field dependence of the unpolarized SANS cross-section of Co nanowires that are embedded in a nonmagnetic Al_2O_3 matrix; $d\Sigma/d\Omega$ clearly changes by a factor of about 5 between the largest field of 2 T and the coercive field of -0.05 T. This observation strongly suggests the existence of intraparticle spin disorder. For such a system, boundary conditions for the magnetization at internal particle-matrix interfaces have to be taken into account, a task which (from the micromagnetic point of view) severely complicates the problem. Nucleation theory [115, 135–137] may provide a guideline for attacking this problem. As a first attempt in this direction, one may employ the known analytical solutions for the spin structure of a cylindrical dot array [216, 217] for computing magnetic SANS.

Recent progress in SANS instrumentation regarding time-resolved data-acquisition procedures (TISANE) [82] opens up the way to study the dynamics of the spin system up to the μs regime. The chopper-based TISANE technique represents an improvement of conventional stroboscopic time-resolved SANS, which is limited by the neutron time-of-flight spread resulting from the wavelength distribution of the incident neutrons ($\Delta\lambda/\lambda \cong 10\,\%$) to about 300 Hz time resolution [218]. TISANE allows one to probe magnetism up to the 10 kHz regime. Therefore, the (analytical and numerical) extension of the present static approach to include magnetization dynamics (Landau–Lifshitz–Gilbert equation) represents a major challenge.

In view of the continuously increasing power of modern computers (e.g. multiprocessor systems, CUDA), a further understanding of magnetic neutron scattering may also be expected from the development of efficient micromagnetic algorithms. Numerical micromagnetic computations can take into account the full nonlinearity of Brown's equations and, indeed, have provided fundamental insights into magnetic SANS [31, 47, 49, 50, 99]. A particular importance/advantage of micromagnetic simulations resides in their flexibility regarding microstructure variations (particle-size distribution, texture, magnetic materials parameters, etc.); it also rather straightforward to 'switch on' and 'off' certain magnetic interactions and to test in this way their impact on the neutron scattering. In general, we believe that the combination of experimental scattering data with large-scale numerical computations will become more and more important in the future.

Acknowledgments

We thank the National Research Fund of Luxembourg for financial support (ATTRACT project no. FNR/A09/01). Critical reading of the manuscript (or of parts of it) by Dirk Honecker, Jens-Peter Bick, Annegret Günther, Sergey Erokhin, and Konstantin Metlov is gratefully acknowledged. It is also a pleasure to acknowledge the support and collaboration with many colleagues, in particular, Elliot Gilbert, Kiyonori Suzuki, Ted Forgan, Charles Dewhurst, Ralf Schweins, Peter Lindner, Albrecht Wiedenmann, Joachim Kohlbrecher, Rainer Birringer, Frank Döbrich, Dmitry Berkov, Artem Feoktystov and André Heinemann.

Appendix.

List with most important parameters, quantities, and relations

$\mathbf{M}(\mathbf{r}) = [M_x(\mathbf{r}), M_y(\mathbf{r}), M_z(\mathbf{r})]$: three-dimensional (Cartesian) magnetization vector field

$\widetilde{\mathbf{M}}(\mathbf{q}) = [\widetilde{M}_x(\mathbf{q}), \widetilde{M}_y(\mathbf{q}), \widetilde{M}_z(\mathbf{q})]$: Fourier transform of the magnetization vector field

$\mathbf{r} = (x, y, z)$: position vector

$\mathbf{q} = (q_x, q_y, q_z)$: wave vector or scattering vector

A: exchange-stiffness constant

$M_s = |\mathbf{M}|$: saturation magnetization

$H_i = H_0 - NM_s$: internal magnetic field

H_0: externally applied magnetic field

$0 < N < 1$: demagnetizing factor of the sample

$d\Sigma/d\Omega$: macroscopic differential SANS cross-section (in units of $cm^{-1}sr^{-1}$)

$d\Sigma_{res}/d\Omega$: nuclear and magnetic residual SANS cross-section; measured at complete magnetic saturation

$d\Sigma_M/d\Omega$: spin-misalignment SANS cross-section; purely magnetic scattering due to transversal spin-misalignment measured away from saturation

$d\Sigma/d\Omega = d\Sigma_{res}/d\Omega + d\Sigma_M/d\Omega$: the magnetic-field-dependent SANS cross-section can be written as the sum of the (nuclear and magnetic) cross-section at saturation and the magnetic (spin-misalignment) SANS signal at a field away from saturation

$S_H(q)$: scattering function of the magnetic anisotropy field (in units of $cm^{-1}sr^{-1}$) (equation (96)); field-independent in the approach-to-saturation regime; can be obtained from the micromagnetic analysis of field-dependent SANS data; integration of $S_H(q)$ over the whole **q**-space yields a lower bound for the average magnetic anisotropy field of the sample (compare equations (107)–(109))

$R_H(q, \theta, H_i, A, M_s)$: dimensionless micromagnetic response function of the magnetic anisotropy field (equation (98)); contains the applied-field dependence, the angular anisotropy, and the dependence of $d\Sigma/d\Omega$ on the magnetic-interaction parameters

$S_M(q)$: scattering function of the magnetostatic field (in units of $cm^{-1}sr^{-1}$) (equation (97)); field-independent in the approach-to-saturation regime; can be obtained from the micromagnetic analysis of field-dependent SANS data; integration of $S_M(q)$ over the whole **q**-space yields a lower bound for the average magnetostatic field due to fluctuations of the magnetization (e.g. at internal interfaces) (compare equations (107)–(109))

$R_M(q, \theta, H_i, A, M_s)$: dimensionless micromagnetic response function of the magnetostatic field (equation (99)); contains the applied-field dependence, the angular anisotropy, and the dependence of $d\Sigma/d\Omega$ on the magnetic-interaction parameters

θ: angle describing the azimuthal orientation of the scattering vector **q** on the two-dimensional detector

$d\Sigma_M/d\Omega = S_H R_H + S_M R_M$: micromagnetic result for the spin-misalignment SANS cross-section in the approach-to-saturation regime (unpolarized neutrons)

$d\Sigma/d\Omega = d\Sigma_{res}/d\Omega + S_H R_H + S_M R_M$: micromagnetic result for the total nuclear and magnetic (unpolarized) magnetic-field-dependent SANS cross-section in the approach-to-saturation regime (equation (103)) ($\mathbf{k}_0 \perp \mathbf{H}_0$); central result of this paper; micromagnetic analysis of field-dependent SANS cross-sections provides the quantities A, $S_H(q)$, $S_M(q)$, and $d\Sigma_{res}/d\Omega$

$C(r)$: autocorrelation function of the spin-misalignment; Fourier transform of $d\Sigma_M/d\Omega$ (compare equations (121) and (125))

$l_H(H_i) = \sqrt{2A/(\mu_0 M_s H_i)}$: micromagnetic exchange length of the field; measure for the size of inhomogeneuously magnetized regions around microstructural defects

$l_C(H_i)$: experimental correlation length of the spin-misalignment (equation (126)); can be obtained from experimental $C(r)$; measure for the size of inhomogeneuously magnetized regions around microstructural defects; depends on l_H, the applied magnetic field, the properties of the defect (e.g. its size), and on the magnetic interactions

References

[1] Schmatz W, Springer T, Schelten J and Ibel K 1974 *J. Appl. Crystallogr.* **7** 96
[2] Schelten J and Hendricks R W 1978 *J. Appl. Crystallogr.* **11** 297
[3] Higgins J S and Stein R S 1978 *J. Appl. Crystallogr.* **11** 346
[4] Gerold V and Kostorz G 1978 *J. Appl. Crystallogr.* **11** 376
[5] Chen S-H and Lin T-L 1987 *Methods of Experimental Physics: Neutron Scattering* vol 23, ed D L Price and K Sköld (San Diego, CA: Academic) pp 489–543
[6] Martin J E and Hurd A J 1987 *J. Appl. Crystallogr.* **20** 61
[7] Bates F S 1988 *J. Appl. Crystallogr.* **21** 681
[8] Hayter J B 1988 *J. Appl. Crystallogr.* **21** 737
[9] Chen S H, Sheu E Y, Kalus J and Hoffmann H 1988 *J. Appl. Crystallogr.* **21** 751
[10] Page R A 1988 *J. Appl. Crystallogr.* **21** 795
[11] Schmidt P W 1991 *J. Appl. Crystallogr.* **24** 414
[12] Kostorz G 1991 *J. Appl. Crystallogr.* **24** 444
[13] Pedersen J S 1997 *Adv. Colloid Interface Sci.* **70** 171
[14] Wiedenmann A 2002 *Ferrofluids: Magnetically Controllable Fluids and Their Applications* (*Lecture Notes in Physics*) ed S Odenbach (Berlin: Springer) pp 33–58
[15] Thiyagarajan P 2003 *J. Appl. Crystallogr.* **36** 373
[16] Fratzl P 2003 *J. Appl. Crystallogr.* **36** 397
[17] Svergun D I and Koch M H J 2003 *Rep. Prog. Phys.* **66** 1735
[18] Stuhrmann H B 2004 *Rep. Prog. Phys.* **67** 1073
[19] Radlinski A P, Mastalerz M, Hinde A L, Hainbuchner M, Rauch H, Baron M, Lin J S, Fan L and Thiyagarajan P 2004 *Int. J. Coal Geol.* **59** 245
[20] Fitzsimmons M R *et al* 2004 *J. Magn. Magn. Mater.* **271** 103
[21] Wagner W and Kohlbrecher J 2005 *Modern Techniques for Characterizing Magnetic Materials* ed Y Zhu (Boston: Kluwer) pp 65–105
[22] Allen A J 2005 *J. Am. Ceram. Soc.* **88** 1367
[23] Wignall G D and Melnichenko Y B 2005 *Rep. Prog. Phys.* **68** 1761

[24] Fritz G and Glatter O 2006 *J. Phys.: Condens. Matter* **18** S2403
[25] Melnichenko Y B and Wignall G D 2007 *J. Appl. Phys.* **102** 021101
[26] Michels A and Weissmüller J 2008 *Rep. Prog. Phys.* **71** 066501
[27] Wiedenmann A 2010 *Collection de la Société Française de la Neutronique* **11** 219
[28] Avdeev M V and Aksenov V L 2010 *Phys.—Usp.* **53** 971
[29] Eskildsen M R, Forgan E M and Kawano-Furukawa H 2011 *Rep. Prog. Phys.* **74** 124504
[30] Pauw B R 2013 *J. Phys.: Condens. Matter* **25** 383201
[31] Michels A, Erokhin S, Berkov D and Gorn N 2014 *J. Magn. Magn. Mater.* **350** 55
[32] Guinier A and Fournet G 1955 *Small-Angle Scattering of X-Rays* (New York: Wiley)
[33] Ibel K 1976 *J. Appl. Crystallogr.* **9** 296
[34] Glatter O and Kratky O 1982 (eds) *Small Angle X-Ray Scattering* (London: Academic)
[35] Feigin L A and Svergun D I 1987 *Structure Analysis by Small-Angle X-Ray and Neutron Scattering* (New York: Plenum)
[36] Lindner P and Zemb T (ed) 1991 *Neutron, X-Ray and Light Scattering: Introduction to an Investigative Tool for Colloidal and Polymeric Systems* (North Holland: Amsterdam)
[37] Bracchi A, Samwer K, Schaaf P, Löffler J F and Schneider S 2004 *Mater. Sci. Eng.* A **375–7** 1027
[38] García-Matres E, Wiedenmann A, Kumar G, Eckert J, Hermann H and Schultz L 2004 *Physica* B **350** e315
[39] García Calderón R, Fernández Barquín L, Kaul S N, Gómez Sal J C, Gorria P, Pedersen J S and Heenan R K 2005 *Phys. Rev.* B **71** 134413
[40] Mergia K and Messoloras S 2008 *J. Phys.: Condens. Matter* **20** 104219
[41] Mergia K and Messoloras S 2012 *J. Phys.: Conf. Ser.* **340** 012069
[42] Heinemann A, Hermann H, Wiedenmann A, Mattern N and Wetzig K 2000 *J. Appl. Crystallogr.* **33** 1386
[43] Ohnuma M, Hono K, Linderoth S, Pedersen J S, Yoshizawa Y and Onodera H 2000 *Acta Mater.* **48** 4783
[44] Michels A, Viswanath R N and Weissmüller J 2003 *Europhys. Lett.* **64** 43
[45] Grob A, Saranu S, Herr U, Michels A, Viswanath R N and Weissmüller J 2004 *Phys. Status Solidi* A **201** 3354
[46] Michels A, Vecchini C, Moze O, Suzuki K, Pranzas P K, Kohlbrecher J and Weissmüller J 2006 *Phys. Rev.* B **74** 134407
[47] Saranu S, Grob A, Weissmüller J and Herr U 2008 *Phys. Status Solidi* A **205** 1774
[48] Honecker D, Ferdinand A, Döbrich F, Dewhurst C D, Wiedenmann A, Gómez-Polo C, Suzuki K and Michels A 2010 *Eur. Phys. J.* B **76** 209–13
[49] Erokhin S, Berkov D, Gorn N and Michels A 2012 *Phys. Rev.* B **85** 024410
[50] Erokhin S, Berkov D, Gorn N and Michels A 2012 *Phys. Rev.* B **85** 134418
[51] Michels A, Honecker D, Döbrich F, Dewhurst C D, Suzuki K and Heinemann A 2012 *Phys. Rev.* B **85** 184417
[52] Yano M, Ono K, Manabe A, Miyamoto N, Shoji T, Kato A, Kaneko Y, Harada M, Nozaki H and Kohlbrecher J 2012 *IEEE Trans. Magn.* **48** 2804
[53] Honecker D and Michels A 2013 *Phys. Rev.* B **87** 224426
[54] Honecker D, Dewhurst C D, Suzuki K, Erokhin S and Michels A 2013 *Phys. Rev.* B **88** 094428
[55] Bick J-P *et al* 2013 *Appl. Phys. Lett.* **102** 022415
[56] Bick J-P, Suzuki K, Gilbert E P, Forgan E M, Schweins R, Lindner P, Kübel C and Michels A 2013 *Appl. Phys. Lett.* **103** 122402
[57] Yano M, Ono K, Harada M, Manabe A, Shoji T, Kato A and Kohlbrecher J 2014 *J. Appl. Phys.* **115** 17A730
[58] Weissmüller J, Michels A, Michels D, Wiedenmann A, Krill I I, Sauer H M and Birringer R 2004 *Phys. Rev.* B **69** 054402
[59] Balaji G, Ghosh S, Döbrich F, Eckerlebe H and Weissmüller J 2008 *Phys. Rev. Lett.* **100** 227202
[60] Döbrich F, Kohlbrecher J, Sharp M, Eckerlebe H, Birringer R and Michels A 2012 *Phys. Rev.* B **85** 094411
[61] Przeniosło R, Winter R, Natter H, Schmelzer M, Hempelmann R and Wagner W 2001 *Phys. Rev.* B **63** 054408
[62] Weissmüller J, Michels A, Barker J G, Wiedenmann A, Erb U and Shull R D 2001 *Phys. Rev.* B **63** 214414
[63] Michels A, Viswanath R N, Barker J G, Birringer R and Weissmüller J 2003 *Phys. Rev. Lett.* **91** 267204
[64] Löffler J F, Braun H B, Wagner W, Kostorz G and Wiedenmann A 2005 *Phys. Rev.* B **71** 134410
[65] Michels A, Elmas M, Döbrich F, Ames M, Markmann J, Sharp M, Eckerlebe H, Kohlbrecher J and Birringer R 2009 *Europhys. Lett.* **85** 47003
[66] Michels A 2010 *Phys. Rev.* B **82** 024433
[67] Honecker D, Döbrich F, Dewhurst C D, Wiedenmann A and Michels A 2011 *J. Phys.: Condens. Matter* **23** 016003
[68] Michels A and Bick J P 2013 *J. Appl. Crystallogr.* **46** 788–90
[69] van den Brandt B *et al* 2006 *Eur. Phys. J.* B **49** 157
[70] van den Brandt B, Glättli H, Hautle P, Kohlbrecher J, Konter J A, Michels A, Stuhrmann H B and Zimmer O 2007 *J. Appl. Crystallogr.* **40** s106
[71] Noda Y, Kumada T, Hashimoto T and Koizumi S 2011 *J. Appl. Crystallogr.* **44** 503
[72] Laver M *et al* 2006 *Phys. Rev. Lett.* **96** 167002
[73] Forgan E, Laver M and Bowell C 2007 *J. Appl. Crystallogr.* **40** s485
[74] Coppola R, Kampmann R, Magnani M and Staron P 1998 *Acta Mater.* **46** 5447
[75] Bischof M, Erlach S, Staron P, Leitner H, Scheu C and Clemens H 2005 *Z. Metallkd.* **96** 1074
[76] Bischof M, Staron P, Michels A, Granitzer P, Rumpf K, Leitner H, Scheu C and Clemens H 2007 *Acta Mater.* **55** 2637
[77] Heintze C, Bergner F, Ulbricht A and Eckerlebe H 2011 *J. Nucl. Mater.* **409** 106
[78] Kreyssig A, Prozorov R, Dewhurst C D, Canfield P C, McCallum R W and Goldman A I 2009 *Phys. Rev. Lett.* **102** 047204
[79] Gazeau F, Dubois E, Bacri J C, Boué F, Cebers A and Perzynski R 2002 *Phys. Rev.* E **65** 031403
[80] Thomson T, Lee S L, Toney M F, Dewhurst C D, Ogrin F Y, Oates C J and Sun S 2005 *Phys. Rev.* B **72** 064441
[81] Ijiri Y, Kelly C V, Borchers J A, Rhyne J J, Farrell D F and Majetich S A 2005 *Appl. Phys. Lett.* **86** 243102
[82] Wiedenmann A, Keiderling U, Habicht K, Russina M and Gähler R 2006 *Phys. Rev. Lett.* **97** 057202
[83] Farrell D F, Ijiri Y, Kelly C V, Borchers J A, Rhyne J J, Ding Y and Majetich S A 2006 *J. Magn. Magn. Mater.* **303** 318
[84] Grigoryeva N A, Grigoriev S V, Eckerlebe H, Eliseev A A, Lukashin A V and Napolskii K S 2007 *J. Appl. Crystallogr.* **40** s532
[85] Napolskii K S, Eliseev A A, Yesin N V, Lukashin A V, Tretyakov Y D, Grigorieva N A, Grigoriev S V and Eckerlebe H 2007 *Physica* E **37** 178
[86] Heinemann A, Wiedenmann A and Kammel M 2007 *J. Appl. Crystallogr.* **40** s57
[87] Bonini M, Wiedenmann A and Baglioni P 2007 *J. Appl. Crystallogr.* **40** s254

[88] Oku T *et al* 2009 *Physica* B **404** 2575
[89] Avdeev M V, Dubois E, Mériguet G, Wandersman E, Garamus V M, Feoktystov A V and Perzynski R 2009 *J. Appl. Crystallogr.* **42** 1009
[90] Grigoriev S V, Syromyatnikov A V, Chumakov A P, Grigoryeva N A, Napolskii K S, Roslyakov I V, Eliseev A A, Petukhov A V and Eckerlebe H 2010 *Phys. Rev.* B **81** 125405
[91] Krycka K L *et al* 2010 *Phys. Rev. Lett.* **104** 207203
[92] Avdeev M V *et al* 2010 *J. Appl. Crystallogr.* **43** 959
[93] Chumakov A P, Grigoriev S V, Grigoryeva N A, Napolskii K S, Eliseev A A, Roslyakov I V, Okorokov A I and Eckerlebe H 2011 *Physica* B **406** 2405
[94] Disch S, Wetterskog E, Hermann R P, Wiedenmann A, Vainio U, Salazar-Alvarez G, Bergström L and Brückel T 2012 *New J. Phys.* **14** 013025
[95] Maurer T, Zighem F, Gautrot S, Ott F, Chaboussant G, Cagnon L and Fruchart O 2013 *Phys. Procedia* **42** 74
[96] Günther A, Bick J P, Szary P, Honecker D, Dewhurst C D, Keiderling U, Feoktystov A V, Tschöpe A, Birringer R and Michels A 2014 *J. Appl. Crystallogr.* **47** 992–8
[97] Toney M F, Rubin K A, Choi S M and Glinka C J 2003 *Appl. Phys. Lett.* **82** 3050
[98] Wismayer M P, Lee S L, Thomson T, Ogrin F Y, Dewhurst C D, Weekes S M and Cubitt R 2006 *J. Appl. Phys.* **99** 08E707
[99] Ogrin F Y, Lee S L, Wismayer M, Thomson T, Dewhurst C D, Cubitt R and Weekes S M 2006 *J. Appl. Phys.* **99** 08G912
[100] Lister S J *et al* 2010 *Appl. Phys. Lett.* **97** 112503
[101] Lister S J, Kohlbrecher J, Venkataramana V, Thomson T, Takano K and Lee S L 2011 *Int. J. Mater. Res.* **102** 1142
[102] Laver M, Mudivarthi C, Cullen J R, Flatau A B, Chen W C, Watson S M and Wuttig M 2010 *Phys. Rev. Lett.* **105** 027202
[103] Ueland B G, Lynn J W, Laver M, Choi Y J and Cheong S W 2010 *Phys. Rev. Lett.* **104** 147204
[104] Ramazanoglu M, Laver M, Ratcliff I I, Watson S M, Chen W C, Jackson A, Kothapalli K, Lee S, Cheong S W and Kiryukhin V 2011 *Phys. Rev. Lett.* **107** 207206
[105] Dufour C, Fitzsimmons M R, Borchers J A, Laver M, Krycka K L, Dumesnil K, Watson S M, Chen W C, Won J and Singh S 2011 *Phys. Rev.* B **84** 064420
[106] Grigoriev S V, Chernyshov D, Dyadkin V A, Dmitriev V, Maleyev S V, Moskvin E V, Menzel D, Schoenes J and Eckerlebe H 2009 *Phys. Rev. Lett.* **102** 037204
[107] Mühlbauer S, Binz B, Jonietz F, Pfleiderer C, Rosch A, Neubauer A, Georgii R and Böni P 2009 *Science* **323** 915
[108] Halpern O and Johnson M H 1939 *Phys. Rev.* **55** 898
[109] Löffler J F, Wagner W and Kostorz G 2000 *J. Appl. Crystallogr.* **33** 451
[110] Wiedenmann A 2005 *Physica* B **356** 246
[111] Lembke U, Hoell A, Kranold R, Müller R, Schüppel W, Goerigk G, Gilles R and Wiedenmann A 1999 *J. Appl. Phys.* **85** 2279
[112] Wiedenmann A 2000 *J. Appl. Crystallogr.* **33** 428
[113] Shull C G, Wollan E O and Koehler W C 1951 *Phys. Rev.* **84** 912
[114] Brown Jr W F 1963 *Micromagnetics* (New York: Interscience)
[115] Aharoni A 1996 *Introduction to the Theory of Ferromagnetism* 2nd edn (Oxford: Clarendon)
[116] Kronmüller H and Fähnle M 2003 *Micromagnetism and the Microstructure of Ferromagnetic Solids* (Cambridge: Cambridge University)
[117] Kronmüller H and Parkin S (ed) 2007 *Handbook of Magnetism and Advanced Magnetic Materials* (*Micromagnetism* vol 2) (Chichester: Wiley)
[118] Kronmüller H, Seeger A and Wilkens M 1963 *Z. Phys.* **171** 291
[119] Seeger A K 1959 *J. Appl. Phys.* **30** 629
[120] Schmatz W, Dederichs P H and Scheuer H 1974 *Z. Phys.* **270** 337
[121] Vorbrugg W and Schärpf O 1975 *Phil. Mag.* A **32** 629
[122] Vorbrugg W 1975 *Phil. Mag.* A **32** 643
[123] Göltz G and Kronmüller H 1980 *Phys. Lett.* A **77** 70
[124] Anders R, Göltz G, Scheuer H and Stierstadt K 1980 *Solid State Commun.* A **35** 423
[125] Anders R, Giehrl M, Röber E, Stierstadt K and Schwahn D 1984 *Solid State Commun.* A **51** 111
[126] Göltz G, Kronmüller H, Seeger A, Scheuer H and Schmatz W 1986 *Phil. Mag.* A **54** 213
[127] Heuser B J and King J S 1997 *J. Alloys Compounds* **261** 225
[128] Shenoy V B, Cleveringa H H M, Phillips R, Van der Giessen E and Needleman A 2000 *Modelling Simul. Mater. Sci. Eng.* **8** 557
[129] Maxelon M, Pundt A, Pyckhout-Hintzen W, Barker J and Kirchheim R 2001 *Acta mater.* **49** 2625
[130] Heuser B J and Ju H 2011 *Phys. Rev.* B **83** 094103
[131] Kronmüller H and Seeger A 1961 *J. Phys. Chem. Solids* **18** 93
[132] Landau L and Lifshitz E 1935 *Phys. Z. Sowjetunion* **8** 153
[133] Herring C and Kittel C 1951 *Phys. Rev.* **81** 869
[134] Skomski R 2003 *J. Phys.: Condens. Matter* **15** R841
[135] Skomski R and Coey J M D 1993 *Phys. Rev.* B **48** 15812
[136] Yang J-S and Chang C-R 1995 *IEEE Trans. Magn.* **31** 3602
[137] Leineweber T and Kronmüller H 1997 *Phys. Status Solidi* **201** 291
[138] Kittel C 1949 *Rev. Mod. Phys.* **21** 541
[139] Bachmann M, Fischer R and Kronmüller H 1998 *Magnetic Anisotropy and Coercivity in Rare-Earth Transition Metal Alloys* ed L Schultz and K H Müller (Frankfurt: Werkstoff- Informationsgesellschaft) pp 217–36
[140] Brooks M S S and Goodings D A 1968 *J. Phys.* C **1** 1279
[141] Colarieti-Tosti M, Simak S I, Ahuja R, Nordström L, Eriksson O, Åberg D, Edvardsson S and Brooks M S S 2003 *Phys. Rev. Lett.* **91** 157201
[142] Chikazumi S 1997 *Physics of Ferromagnetism* (Oxford: Clarendon)
[143] Aharoni A 1960 *Phys. Rev.* **119** 127
[144] Abraham C and Aharoni A 1960 *Phys. Rev.* **120** 1576
[145] Brown W F Jr 1940 *Phys. Rev.* **58** 736
[146] Brown W F Jr 1941 *Phys. Rev.* **60** 139
[147] Kronmüller H 1966 *Moderne Probleme der Metallphysik* vol 2, ed A Seeger (Berlin: Springer) pp 24–156
[148] Schlömann E 1967 *J. Appl. Phys.* **38** 5027
[149] Schlömann E 1971 *J. Appl. Phys.* **42** 5798
[150] Kronmüller H and Ulner J 1977 *J. Magn. Magn. Mater.* **6** 52
[151] Fähnle M and Kronmüller H 1978 *J. Magn. Magn. Mater.* **8** 149
[152] Porod G 1982 *Small Angle X-Ray Scattering* ed O Glatter and O Kratky (London: Academic) pp 17–51
[153] Pfleiderer C *et al* 2010 *J. Phys.: Condens. Matter* **22** 164207
[154] Hubert A and Schäfer R 1998 *Magnetic Domains* (Berlin: Springer) p 10
[155] Lowde R D and Umakantha N 1960 *Phys. Rev. Lett.* **4** 452
[156] Stringfellow M W 1968 *J. Phys.* C **1** 950
[157] Okorokov A I, Runov V V, Toperverg B P, Tretyakov A D, Maltsev E I, Puzei I M and Mikhailova V E 1986 *JETP Lett.* **43** 503
[158] Maleev S V 1965 *Soviet Phys.—JETP* **21** 969
[159] Glinka C J, Barker J G, Hammouda B, Krueger S, Moyer J J and Orts W J 1998 *J. Appl. Crystallogr.* **31** 430
[160] Schelten J and Schmatz W 1980 *J. Appl. Crystallogr.* **13** 385
[161] Pedersen J S, Posselt D and Mortensen K 1990 *J. Appl. Crystallogr.* **23** 321

[162] May R P 1994 *J. Appl. Crystallogr.* **27** 298
[163] Allen A J and Berk N F 1994 *J. Appl. Crystallogr.* **27** 878
[164] Barker J G and Pedersen J S 1995 *J. Appl. Crystallogr.* **28** 105
[165] Kohlbrecher J and Wagner W 2000 *J. Appl. Crystallogr.* **33** 804
[166] Mazumder S, Sen D, Roy S K, Hainbuchner M, Baron M and Rauch H 2001 *J. Phys.: Condens. Matter* **13** 5089
[167] Šaroun J 2007 *J. Appl. Crystallogr.* **40** s701
[168] Dewhurst C D 2008 *Meas. Sci. Technol.* **19** 034007
[169] Mildner D F R and Cubitt R 2012 *J. Appl. Crystallogr.* **45** 124
[170] Bazhenov A N, Lobashev V M, Pirozhkov A N and Slusar V N 1993 *Nucl. Instrum. Meth.* A **332** 534
[171] Keller T, Krist T, Danzig A, Keiderling U, Mezei F and Wiedenmann A 2000 *Nucl. Instrum. Meth.* A **451** 474
[172] Petoukhov A K *et al* 2006 *Nucl. Instrum. Meth.* A **560** 480
[173] Batz M, Baeßler S, Heil W, Otten E W, Rudersdorf D, Schmiedeskamp J, Sobolev Y and Wolf M 2005 *J. Res. NIST* **110** 293
[174] Moon R M, Riste T and Koehler W C 1969 *Phys. Rev.* **181** 920
[175] Maleev S V 1961 *Soviet Phys.—JETP* **13** 860
[176] Izyumov Y A and Maleev S V 1962 *Soviet Phys.—JETP* **14** 1168
[177] Maleev S V, Bar'yakhtar V G and Suris R A 1963 *Sov. Phys. Solid State* **4** 2533
[178] Blume M 1963 *Phys. Rev.* **130** 1670
[179] Marshall W and Lowde R D 1968 *Rep. Prog. Phys.* **31** 705
[180] Okorokov A I, Runov V V and Gukasov A G 1978 *Nucl. Instrum. Meth.* **157** 487
[181] Mezei F 1986 *Physica* B **137** 295
[182] Tasset F 1989 *Physica* B **156–7** 627
[183] Schärpf O and Capellmann H 1993 *Phys. Status Solidi* A **135** 359
[184] Schweizer J 2006 *Neutron Scattering from Magnetic Materials* ed T Chatterji (Amsterdam: Elsevier) pp 153–213
[185] Brown P J 2006 *Neutron Scattering from Magnetic Materials* ed T Chatterji (Amsterdam: Elsevier) pp 215–44
[186] Squires G L 1978 *Introduction to the Theory of Thermal Neutron Scattering* (New York: Dover)
[187] Lovesey S W 1984 *Theory of Neutron Scattering from Condensed Matter* vol II (Oxford: Clarendon)
[188] Williams W G 1988 *Polarized Neutrons* (Oxford: Clarendon)
[189] Hicks T J 1995 *Magnetism in Disorder* (Oxford: Clarendon)
[190] Wildes A R 2006 *Neutron News* **17** 17
[191] Keiderling U 2002 *Appl. Phys.* A **74** S1455
[192] Keiderling U, Wiedenmann A, Rupp A, Klenke J and Heil W 2008 *Meas. Sci. Technol.* **19** 034009
[193] Krycka K, Chen W, Borchers J, Maranville B and Watson S 2012 *J. Appl. Crystallogr.* **45** 546
[194] Grigoriev S V, Metelev S V, Maleyev S V, Okorokov A I, Böni P, Georgii R, Lamago D, Eckerlebe H and Pranzas K 2005 *Phys. Rev.* B **72** 214423
[195] Kohlbrecher J and Bressler I 2014 *Software package SASfit for fitting small-angle scattering curves* (https://kur.web.psi.ch/sans1/SANSSoft/sasfit.html)
[196] Kline S R 2006 *J. Appl. Crystallogr.* **39** 895
[197] Sato M and Hirakawa K 1975 *J. Phys. Soc. Japan* **39** 1467
[198] Suzuki K, Makino A, Inoue A and Masumoto T 1994 *J. Magn. Soc. Japan* **18** 800
[199] Weissmüller J, McMichael R D, Michels A and Shull R D 1999 *J. Res. Natl Inst. Stand. Technol.* **104** 261
[200] Thomson R, Levine L E and Long G G 1999 *Acta Crystallogr.* A **55** 433
[201] Long G G and Levine L E 2005 *Acta Crystallogr.* A **61** 557
[202] Michels A, Vecchini C, Moze O, Suzuki K, Cadogan J M, Pranzas P K and Weissmüller J 2005 *Europhys. Lett.* **72** 249
[203] Herzer G 1997 *Handbook of Magnetic Materials* vol 10, ed K H J Buschow (Amsterdam: Elsevier) pp 415–62
[204] Suzuki K and Cadogan J M 1998 *Phys. Rev.* B **58** 2730
[205] Suzuki K and Herzer G 2006 *Advanced Magnetic Nanostructures* ed D Sellmyer and R Skomski (New York: Springer) pp 365–401
[206] Alperin H A, Steinsvoll O, Shirane G and Nathans R 1966 *J. Appl. Phys.* **37** 1052
[207] Guinier A 1994 *X-Ray Diffraction in Crystals, Imperfect Crystals and Amorphous Bodies* (New York: Dover) p 31
[208] Schrefl T, Kronmüller H and Fidler J 1993 *J. Magn. Magn. Mater.* **127** L273
[209] Woodcock T G, Zhang Y, Hrkac G, Ciuta G, Dempsey N M, Schrefl T, Gutfleisch O and Givord D 2012 *Scr. Mater.* **67** 536
[210] Maleyev S V 1982 *J. Phys. Coll.* **43** C7–23
[211] Rosman R and Rekveldt M T 1991 *Phys. Rev.* B **43** 8437
[212] Rekveldt M T, van Dijk N H, Grigoriev S V, Kraan W H and Bouwman W G 2006 *Rev. Sci. Instrum.* **77** 073902
[213] Bogdanov A N and Yablonskii D A 1989 *Sov. Phys.—JETP* **68** 101
[214] Bogdanov A and Hubert A 1994 *J. Magn. Magn. Mater.* **138** 255
[215] Bogdanov A N, Rössler U K and Pfleiderer C 2005 *Physica* B **359–61** 1162
[216] Metlov K L 2006 *Phys. Rev. Lett.* **97** 127205
[217] Metlov K L 2010 *Phys. Rev. Lett.* **105** 107201
[218] Wiedenmann A, Gähler R, Dewhurst C D, Keiderling U, Prévost S and Kohlbrecher J 2011 *Phys. Rev.* B **84** 214303